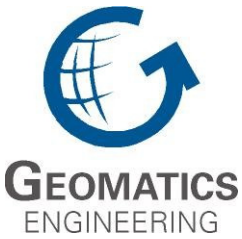


**UCGE Reports**
**Number 20319**

Department of Geomatics Engineering

# Integration of Precise Point Positioning and Low Cost MEMS IMU

**(URL: http://www.geomatics.ucalgary.ca/graduatetheses)**

**by**

**Shuang Du**

**November 2010**

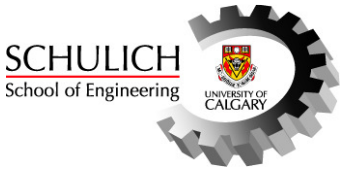

UNIVERSITY OF CALGARY

# Integration of Precise Point Positioning and Low Cost MEMS IMU

by

Shuang Du

A THESIS

SUBMITTED TO THE FACULTY OF GRADUATE STUDIES

IN PARTIAL FULFILMENT OF THE REQUIREMENTS FOR THE

DEGREE OF MASTER OF SCIENCE

DEPARTMENT OF GEOMATICS ENGINEERING

CALGARY, ALBERTA

NOVEMBER 2010

**Abstract**

Global Positioning System (GPS) and low cost Inertial Navigation System (INS) integrated systems are expected to become more widespread as a result of the availability of low cost inertial Micro-Electro-Mechanical Sensors (MEMS). This integrated system has been widely and successfully applied in many applications, such as vehicle navigation and mobile mapping system.

Currently most of the GPS/INS integrated systems are based on the differential GPS (DGPS) to ensure the navigation performance. However the requirement on a base station is usually problematic as it limits the operational range of the system and also increases the system cost and complexity. To tackle this issue, a method to integrate the data from a single GPS receiver and a low cost MEMS Inertial Measurement Unit (IMU) for autonomous positioning and attitude determination is developed in this thesis. The GPS and IMU data will be fused based on the Precise Point Positioning (PPP) technology, which is able to provide centimetre to decimetre positioning accuracy by using a single dual-frequency receiver and is therefore employed to ensure the navigation performance. Previous work has demonstrated that the integration of PPP GPS and tactical grade IMU is able to provide navigation solution with accuracy at centimetre to decimetre for position and centimetre per second for velocity. However, due to the expensive cost of the tactical grade IMU, it is not suitable for the commercial applications.

The motivation of this research is to investigate the integration of PPP GPS and low cost MEMS IMU for precise positioning and attitude determination. Both loose and tight

integration of PPP GPS and MEMS IMU are studied and loosely and tightly coupled Kalman filters are developed to derive the optimal navigation solutions. The primary observable used in PPP GPS is the carrier phase measurement, and it is well known that the undetected cycle slips deteriorate its high precision nature and eventually degrade the overall system performance. An algorithm of inertial aided cycle slip detection and identification is also investigated in this thesis. Two van tests are conducted to evaluate the performance of the developed integrated PPP GPS/MEMS IMU system. The performance analysis is carried out based the position, velocity and attitude errors. A loosely coupled DGPS/tactical grade IMU system is used to provide the reference solution.

**Acknowledgements**

First of all, I would like to express my sincere gratitude to my supervisor, Dr. Yang Gao. He continuously encouraged me to go through all the research during my graduate studies at The University of Calgary. Without the supervision and the support from him, this study cannot be done.

Dr. Yang Gao, Dr. Naser El-Sheimy, Dr. Kyle O'Keefe and Dr. Behrouz Far, members of my examination committee, are greatly acknowledged for your time to read this thesis.

Dr. Kongzhe Chen and Dr. Yufeng Zhang in the PMIS group are greatly thanked for offering valuable comments and suggestions on my research. I am also grateful to those graduate students, Hang Liu, Da Wang, Peng Xie, Tao Lin, Feng Tang, Feng Xu, Feng Man and Junbo Shi, in this department who helped me with my research and answered my questions.

Special thanks to Dr. Gérard Lachapelle, Dr. Mark Petovello, Jared Bancroft and Tao Li for providing me the field test dataset. Without your help, this research cannot be finished.

Finally, and most importantly, I would like to thank my parents, Liping Du and Furong Lan, for their unconditional love, encouragement through all of my years. This work would not have been possible without their support.

## Table of Contents

## List of Tables

## List of Figures and Illustrations

## List of Symbols

| Symbol | Definition |
|---|---|
| $D^{-1}$ | Relationship matrix between the position rate and velocity in the l-frame |
| $F(t)$ | System dynamics matrix |
| $G(t)$ | Shaping matrix |
| $H_k$ | Design matrix at time $t_k$ |
| $H(P)$ | Design matrix for pseudorange measurement |
| $H_{2D}$ | Design matrix for 2D velocity constraints |
| $H(\Phi)$ | Design matrix for carrier phase measurements |
| $H(\dot{\Phi})$ | Design matrix for Doppler measurements |
| $K_k$ | Kalman gain matrix at time $t_k$ |
| $M_{dry}$ | Dry mapping function |
| $M_{wet}$ | Wet mapping function |
| $N$ | Ambiguity in carrier phase measurement |
| $P$ | GPS pseudorange measurement |
| $P_{k,k-1}$ | A priori covariance matrix at time $t_k$ |
| $P_{k-1}$ | Posteriori covariance matrix at time $t_{k-1}$ |
| $Q_k$ | Discrete processing noise at $t_k$ |
| $Q(t)$ | Spectral density matrix of $w(t)$ |
| $R_b^e$ | Rotation matrix from the b-frame to the e-frame |
| $R_b^l$ | Rotation matrix from the b-frame to the l-frame |
| $R_e^l$ | Rotation matrix from the e-frame to the l-frame |
| $R_m$ | Meridian radius of the earth curvature |
| $R_n$ | Prime vertical radius of the earth curvature |

| | |
|---|---|
| $R_1, R_2, R_3$ | Rotation matrices about X, Y, and Z axes, respectively |
| $S_a$ | Accelerometer scale factor |
| $S_g$ | Gyroscope scale factor |
| $T_D$ | Threshold for cycle slip detection |
| $TEC$ | Total electron content |
| $T_{GD,r}$ | Receiver inter-frequency bias in code measurement |
| $T'_{GD,r}$ | Receiver inter-frequency bias in carrier phase measurement |
| $T_{GD,s}$ | Satellite inter-frequency bias in code measurement |
| $T'_{GD,s}$ | Satellite inter-frequency bias in carrier phase measurement |
| $T_N$ | Threshold for cycle slip identification |
| $b_a$ | Accelerometer bias |
| $b_{a,tob}$ | Accelerometer turn on bias |
| $b_g$ | Gyro bias |
| $b_{g,tob}$ | Gyro turn on bias |
| $c$ | Light speed |
| $dT$ | Receiver clock error |
| $\dot{dT}$ | Receiver clock error drift |
| $d_{dry}$ | Zenith dry component of tropospheric delay |
| $d_{ion}$ | Ionospheric delay |
| $\dot{d}_{ion}$ | Ionospheric delay drift |
| $d_{orb}$ | Satellite orbital error |
| $\dot{d}_{orb}$ | Satellite orbital error drift |
| $dt$ | Satellite clock error |

| | |
|---|---|
| $\dot{dt}$ | Satellite clock error drift |
| $d_{trop}$ | Tropospheric delay |
| $\dot{d}_{trop}$ | Tropospheric delay drift |
| $d_{wet}$ | Zenith wet component of tropospheric delay |
| $f^E, f^N, f^U$ | Specific force in the l-frame |
| $f^b$ | Specific force vector sensed by the accelerometer triad |
| $f(x(t),t)$ | Nonlinear function |
| $g^l$ | Earth's local gravity vector |
| $q_{V_E}$ | Spectral density of the velocity in east direction |
| $q_{V_N}$ | Spectral density of the velocity in north direction |
| $q_{V_U}$ | Spectral density of the velocity in up direction |
| $q_{V_{dt}}$ | Spectral density of the receiver clock error drift |
| $q_{trop}$ | Spectral density of the wet component of the tropospheric delay |
| $r^l$ | Position vector in the l-frame |
| $v_k$ | Discrete measurement noise vector |
| $v^l$ | Velocity vector in the l-frame |
| $w(t)$ | Noise vector |
| $x(t)$ | System state vector |
| $x^*(t)$ | Nominal trajectory |
| $\delta Z_k$ | Measurement error vector |
| $\delta r^l$ | Position error state vector in the l-frame |
| $\delta v^l$ | Velocity error state vector in the l-frame |
| $\delta x_k$ | System state (error) vector at $t_k$ |

| | |
|---|---|
| $\delta x(t)$ | Error state vector |
| $\delta\varepsilon^{l}$ | Attitude error state vector in the l-frame |
| $\Phi$ | GPS carrier phase measurement |
| $\dot{\Phi}$ | GPS Doppler measurement |
| $\Phi_{k,k-1}$ | State transition matrix from $t_{k-1}$ to $t_k$ |
| $\Omega_{bc}^{a}$ | Skew-symmetric matrix form of vector $\omega_{bc}^{a}$ |
| $\varepsilon(P)$ | Combination of code noise and multipath |
| $\varepsilon(\Phi)$ | Combination of carrier phase noise and multipath |
| $\varepsilon(\dot{\Phi})$ | Doppler measurement noise |
| $\rho$ | Geometric range |
| $\dot{\rho}$ | Geometric range rate |
| $\varphi$ | Latitude |
| $\dot{\varphi}$ | Latitude rate |
| $\lambda$ | Longitude |
| $\dot{\lambda}$ | Longitude rate |
| $\psi$ | Azimuth angle |
| $\theta$ | Pitch angle |
| $\phi$ | Roll angle |
| $\tau$ | Correlation time |
| $\eta$ | Gauss-Markov process driving noise |
| $\omega_{el}^{l}$ | Transport rate |
| $\omega_{ib}^{b}$ | Angular rate vector sensed by the gyroscope triad |
| $\omega_{ie}^{l}$ | Earth rotation rate projected into the l-frame |
| $\omega_{e}$ | Earth rotation rate respect to the i-frame |
| $\Delta\tilde{v}_{f}^{b}$ | Velocity increment from the accelerometer output |

| | |
|---|---|
| $\Delta v_f^b$ | Actual velocity increment |
| $\Delta \tilde{\theta}_{ib}^b$ | Angular increment from the gyro output |
| $\Delta \theta_{ib}^b$ | Actual angular increment |

## List of Abbreviations

| | |
|---|---|
| AR | Auto-Regressive |
| CS | Cycle Slip |
| DGPS | Differential Global Positioning System |
| DOP | Dilution of Precision |
| DV | Decision Variable |
| DoD | Department of Defense |
| ECEF | Earth Center Earth Fixed |
| EKF | Extended Kalman Filter |
| ENU | East-North-Up |
| EWL | Extra Widelane |
| GPS | Global Positioning System |
| IF | Ionosphere-free |
| IGS | International GPS service |
| IMU | Inertial Measurement Unit |
| INS | Inertial Navigation System |
| JPL | Jet Propulsion Laboratory |
| LC | Loosely Coupled |
| LKF | Linearized Kalman Filter |
| LLF | Local Level Frame |
| MEMS | Micro-Electro-Mechanical Sensor |
| NRCan | Natural Resources Canada |
| PPM | Parts Per Million |
| PPP | Precise Point Positioning |
| PPS | Pulse Per second |
| PRN | Pseudo Random Noise |
| PVA | Position, Velocity and Attitude |
| PVT | Position, Velocity and Time |
| RF | Radio Frequency |

| | |
|---|---|
| RMS | Root Mean Square |
| SPS | Standard Positioning Service |
| STD | Standard Deviation |
| SV | Space Vehicle |
| TC | Tightly Coupled |
| TEC | Total Electron Content |
| TOA | Time-Of-Arrival |
| UAV | Unmanned Aerial Vehicle |
| WL | Widelane |

# Chapter One: Introduction

Nowadays, the powerful synergy between Global Positioning System (GPS) and Inertial Navigation System (INS), along with the availability of the low cost inertial Micro-Electro-Mechanical Sensors (MEMS), makes the integration of the two navigation technologies more widespread (Mathur and Grass, 2000). The integration can be implemented using a Kalman filter in such modes as loosely coupled and tightly coupled. In both of the modes, the INS error states, together with the navigation states and other unknown parameters of interests, are estimated using the GPS measurements (Park and Gao, 2002). This thesis investigates an integrated GPS/INS system based a single dual-frequency GPS receiver and a low cost MEMS inertial measurement unit (IMU). To ensure the navigation performance, the Precise Point Positioning (PPP) technique is employed.

## 1.1 Background

Currently most of the GPS/INS integrated systems are based on the differential GPS (DGPS) to ensure the navigation performance. In such a system, two GPS receivers must be employed, one as a base station set up at a precisely surveyed control point while the other as a rover station installed on the vehicle platform. However, the requirement on a base station is usually problematic for some applications as it limits the operational range of the system and also increases the system cost and complexity. With the advent of the Precise Point Positioning (PPP) GPS, which is able to provide centimetre to decimetre positioning accuracy without the need for a base receiver station, it opens the opportunity

to develop a high performance integrated GPS/INS system based on only one GPS receiver.

Zhang and Gao (2007) demonstrated that the integration of PPP GPS and tactical grade IMU is able to provide position accuracy at centimetre to decimetre and velocity accuracy at centimetre per second. However, the tactical grade IMU is too expensive for many commercial applications. Considering the price and the acceptable performance, the MEMS IMU is a good alternative for commercial applications. The challenge of working with the current generation of the low cost MEMS IMU is to develop a robust navigation capability that can deal with the large instrument errors (Brown and Lu, 2004). In the proposed PPP GPS/MEMS IMU integrated system, the MEMS inertial sensor errors can be continuously estimated with the availability of the PPP GPS, as a result the INS error accumulation can be limited; on the other hand, the low cost MEMS inertial sensors can bridge the navigation estimates during the PPP GPS outages. Eventually, the derived navigation solution from an integrated system is better than either standalone solutions.

The proposed integrated PPP GPS/MEMS IMU system can be useful to many applications. Some of them are briefly described in the following.

1) Unmanned Aerial Vehicle (UAV) Navigation Systems

In recent years, the UAV has been more and more used in the civilian applications, such as the disaster assessment and management, life search and rescue, environmental

monitoring and mineral exploration (Kim and Sukkarieh, 2002). For different UAV applications, the position, velocity and attitude information is necessary for the ground station control or autonomous navigation. The requirements on the accuracies of the position, velocity and attitude information depend on the missions that the UAV is intended to perform. Currently some commercial navigation or autonomous guidance systems for the UAVs are developed based on the low grade GPS/MEMS IMU systems, which are only able to offer positioning accuracy at several to tens of metres. This may not be suitable for some applications that require higher positioning accuracy. Some other navigation and guidance systems are developed based on the differential GPS (DGPS) to ensure the navigation performance. This is also problematic for some applications such as disaster & emergency management since the setup of a base station is not time effective and it also limits the operational range of the system and further increases the system cost and complexity.

The proposed integrated PPP GPS/MEMS IMU system can be used as the UAV navigation and guidance system, especially when the base station is difficult to be set up. The accurate navigation solutions provided by the integrated system can be used to track the UAV or, in combination with an automated guidance system, to steer the UAV.

2) Land Vehicle/Machine Automation

A navigation system based on a low cost MEMS IMU integrated GPS has been widely used in land vehicle/machine automation applications, such as guidance of dozers, drills,

draglines and shovels in mining and grader excavators and pavers for construction (Geng et al., 2007). Nowadays, most of such systems are developed based on the DGPS, which is costly and limits the operational range. Another issue is that the cycle slips occur frequently for the land vehicle/machine applications due to the signal blockages, which potentially degrades the navigation performance.

The proposed integrated PPP GPS/MEMS IMU system can be used to provide the navigation guidance for the machine automation without the need for a base receiver station, and reduce the system cost and complexity. With the aiding from the MEMS IMU, the cycle slips on carrier phase measurements can be detected and identified by developing inertial aided cycle slip detection and identification algorithms.

3) Mobile Mapping Systems (MMS)

The MMS integrates a set of sensors such as inclinometer, compass, IMU, GPS and camera, mounted on a common platform and it is capable of operating and collecting navigation and image data that are sufficient to do the mapping process without the need to establish costly, and time consuming terrestrial ground control network (Ellum, 2001; El-Sheimy and Schwarz, 1999). Currently, the integrated GPS/INS systems are extensively used for direct geo-referencing of the MMS. In such systems, the navigation-grade or tactical-grade IMU are commonly used to ensure the necessary navigation performance. The high cost of such IMUs, their considerable size and their restricted handing regulations have limited their use (Niu et al., 2006). Recently, the MEMS IMU

has been considered as an alternative for the navigation-grade IMU or tactical-grade IMU in MMS due to its small size, light weight, inexpensive cost.

The proposed integrated system has the potential to be used by the MEMS-based mobile mapping system, with advantages being low-cost and small size although the attitude accuracy requires further improvement.

The PPP GPS and MEMS IMU are briefly introduced in the following sections.

### *1.1.1 Precise Point Positioning GPS*

The PPP uses un-differenced GPS measurements from a single dual-frequency GPS receiver, such as pseudorange, carrier phase observations, in addition to precise orbit and clock data. This technique does not suffer from the drawbacks of the conventional DGPS technique and is able to provide similar positioning accuracy comparable to DGPS without the need for a base station (Zhang and Gao, 2005). Several organizations, such as International GPS Service (IGS) and Jet Propulsion Laboratory (JPL), provide the precise GPS orbit and clock products. IGS is a civilian organization, which operates a global network of high quality dual frequency GPS stations and provides the GPS orbit and clock, earth rotation parameters, troposphere delay and global ionosphere map. JPL operates a global network of GPS stations and calculates the corrections corresponding to the broadcast satellite orbit and clock corrections. These corrections are then transferred to the users through the Internet (Aldel-Salam, 2005). The Natural Resources Canada (NRCan) is also operating a network of GPS stations all over Canada and produce real

time satellite orbit and clock corrections, which are available through the Internet and the Canadian MSAT communication satellite (Lochhead et al., 2002).

Precise Point Positioning technology was proposed by Zumberge et al. (1997) as well as Kouba and Heroux (2000). Zumberge et al. (1997) suggested a method for calculating the orbit and clock data using a subset of the IGS network. By using the precise data with intervals of 30 seconds and 15 minutes for satellite clock and orbit, respectively, promising results were obtained based on their technique. Kouba and Heroux (2000) were the first to publish the technique of using un-differenced code and carrier phase observations from a dual-frequency receiver. They emphasized error mitigations especially those related to the un-differenced code and carrier phase observations. Using the GPS data at interval of 30 seconds, the unknown parameters were estimated at 15 minutes interval. They obtained results comparable to Zumberge's (1997).

The research work from Zumberge et al. (1997) as well as Kouba and Heroux (2000) was focused on using the ionosphere-free combination of pseudorange and carrier phase observations. The unknowns include one float ambiguity term for each satellite in addition to position coordinates, a receiver clock offset and a troposphere parameter. Gao and Shen (2001) introduced a new observation model that uses the average of code and carrier phase observations on both L1 and L2 frequencies in addition to the ionosphere-free carrier phase combination. The newly developed model allows for estimation of ambiguities on both L1 and L2 frequencies for each satellite along with the position parameter, receiver clock offset and tropospheric delay.

Since the success of Precise Point Positioning system significantly improves the operational flexibility and reduces the system cost, it increases the number of applications using GPS technology, such as geodetic surveys, machine control and atmosphere sensing (Aldel-Salam, 2005).

### *1.1.2 Low Cost MEMS IMU*

The key of development of MEMS IMU is the need to maintain reasonable cost levels when using an INS for consumer applications. With smaller size and lower price, inertial technology is now being used in applications that were previously not feasible due to size and cost constraints (Hide et al., 2003). The MEMS IMUs are often categorized as automotive grade sensors based on their performance levels and intended applications.

Table 1.1 presents the error characteristics of different IMUs, which include the low cost MEMS IMU, the tactical and navigation grade IMU. As illustrated in the table, the MEMS IMU (categorized under the automotive grade) features a turn on bias of several thousand degrees per hour in gyroscopes and a scale factor of about 10000 PPM, while these errors can be negligible in tactical grade or higher grade IMUs. Also, the MEMS IMU exhibits in-run bias of more than 1000 degrees per hour in gyroscopes, comparing to 1~10 degrees per hour for a tactical grade IMU, and about 0.01 degree per hour for a navigation grade IMU. However, the MEMS IMU is preferred for commercial applications in terms of cost. As it can be noted, the cost of MEMS IMU is ten times lower than that of tactical grade IMU.

**Table 1.1 Performance of different grade of IMU (Modified from Godha, 2006)**

| Grade | Navigation | Tactical | Automotive |
|---|---|---|---|
| **Accelerometers** | | | |
| **In Run Bias (mg)** | 0.05~0.1 | 0.5~1 | 2.5 |
| **Turn On Bias (mg)** | N/A | N/A | 30 |
| **Scale Factor (PPM)** | 100 | 300 | 10000 |
| **Gyroscopes** | | | |
| **In Run Bias (deg/hr)** | 0.01 | 1~10 | < 1200 |
| **Turn On Bias (deg/hr)** | N/A | N/A | 5000 |
| **Scale Factor (PPM)** | 5 | 150 | 10000 |
| **Cost** | >$90K | $10K-$20K | <$5 |

Given the significant sensor errors of MEMS IMU, some traditional approaches of using the high-end IMU are not suitable for MEMS IMU, for instance, the coarse alignment method cannot be implemented with MEMS IMU. As a result, some non-traditional algorithms and approaches are required (Salychev et al., 2000; Ford et al., 2001).

## 1.2 Literature Review

The integration of GPS and low cost INS has been a popular research area over the past decades. This section briefly reviews the research that investigates the GPS and INS integration techniques.

### *1.2.1 Integration of GPS and INS Using a Kalman Filter*

In the last few years, some research was conducted to investigate the GPS/INS integration using the Kalman filtering. Salychev et al (2000) and Nayak (2000) applied a loose integration strategy to integrate the MotionPak$^{TM}$ MEMS IMU with DGPS using pseudorange and Doppler measurements. Hide (2003) investigated the tightly coupled integrated DGPS/INS system for marine application based on a Crossbow AHRS DMU-HDX IMU and carrier phase measurements. Shin and El-Sheimy (2004) applied the unscented Kalman filter and extended Kalman filter to the integration of DGPS and low cost MEMS IMU. Li et al (2006) investigated the low cost tightly coupled GPS/INS integration based on a nonlinear Kalman filter design. Wang (2006) developed a loosely coupled integrated GPS/MEMS IMU system using the aiding from the fuzzy logic expert system. The above research primarily investigated the system performance under benign operation environments.

Some research was to study the system performance under more realistic environments, such as urban canyon area. Hide and Moore (2005) investigated the positioning performance of the DGPS and low cost INS integrated system in urban environments. Their research demonstrated that the tightly coupled system outperformed the loosely

coupled system and a horizontal error around 20 m was obtained by using a tight integration of Crossbow AHRS400 MEMS IMU and DGPS in the city of Nottingham, UK. Godha (2006) also investigated the performance of the DGPS/MEMS IMU integrated system and he obtained a horizontal error of less than 10 m by using a tight integration of DGPS and Crista MEMS IMU without applying any vehicle motion constraints in the downtown of Calgary, Canada. His research also demonstrated that a comparable accuracy to a DGPS/HG1700 integrated system was obtained in the urban area with vehicle motion constraints. However, the use of DGPS increases the system cost and limits the operational range.

### *1.2.2 Inertial Sensor Modeling*

Some research has been conducted to characterize the inertial sensor random errors, which primarily focus on the sensor noise. Generally, the sensor noise consists of a high frequency component, which has white noise characteristics, and a low frequency component, which is commonly termed as bias drift and can be characterized by correlated noise (Nassar, 2003). Chiang et al (2004) and Abdel-Hamid et al (2004) investigated the wavelet de-nosing technique to de-noise the inertial sensor measurements prior to data processing. Chiang et al (2004) applied the wavelet de-nosing technique to the MEMS IMU and obtained about 5% - 20% improvements, while Abdel-Hamid et al (2004) obtained 30%-60% improvements by using the same technique. Nassar et al (2003) used the Auto-Regressive (AR) modeling methods to model the bias-drifts and it was shown to provide slight improvement in system performance.

### *1.2.3 Integration of GPS/INS System with Other Sensors*

Investigations were also conducted to incorporate the GPS/INS system with other sensors. The initial alignment is an important issue to use low cost MEMS IMU, since the initial attitude information cannot be obtained by using the conventional coarse alignment method due to significant sensor errors. Normally the initial azimuth information is obtained from the external source. Salychev et al (2000) and Nayak (2000) used a magnetic compass to provide the heading information to the integrated GPS/INS system.

The performance of INS during the GPS outages is degraded rapidly due to lack of updates. Some research has investigated to resolve this issue with the help of auxiliary sensors. Sukkarieh (2000) and Shin (2005) incorporated the GPS/INS system with an odometer to control the INS errors during GPS outages. Zhang et al. (2003) and Wang (2006) integrated the GPS/INS system with a magnetometer to improve the INS performance when there are no GPS updates. Numajima et al. (2002) and Lee (2002) used Vehicle Motion Sensors and an array of pseudolites to mitigate INS error accumulation, respectively.

Due to the large sensor errors and poor observability, the attitude accuracies are typically poor when a low cost MEMS IMU is used. The azimuth accuracy is even poorer than the accuracies of roll and pitch, especially when the horizontal accelerations are absent. Investigations were also conducted to resolve this issue. Hirokawa (2008) integrated the GPS/INS system with a multiple antenna GPS compass to improve the heading accuracy. Li (2009) used the forward speed information, obtained from a wheel speed sensor, along

with the 2D (lateral and vertical) velocity constraints to improve the attitude accuracies in a GPS/INS integrated system. However, the use of additional sensors increases the overall system cost.

### 1.3 Research Objectives and Contributions

Given the lack of research work on the integration of low-cost MEMS IMU with PPP GPS for precise positioning, this thesis is devoted to develop an integrated GPS/INS system based on the PPP GPS and low-cost MEMS IMU. The specific objectives of this thesis are provided in the following:

1) To develop an integrated Precise Point Positioning GPS/MEMS IMU system without the need for a base receiver station and to investigate the performance of the integrated system using both loose and tight integration strategies.

2) Due to the significant sensor errors of MEMS IMU, the proposed integrated system can only result in relatively poor attitude accuracies. To improve the attitude accuracies, the 2D velocity constraints are used and their improvements are analyzed.

3) The GPS outages can be encountered in the realistic environments, such as urban areas. This thesis also investigates the ability of MEMS IMU to bridge the GPS outages and to analyze the performance improvements obtained by using the 2D velocity constraints.

4) The cycle slips occur frequently for the land vehicle/machine applications due to the signal blockages. To detect and fix these cycle slips, an inertial aided cycle slip detection and identification algorithm is investigated in this thesis. The developed algorithm is able to detect the possible cycle slips and eventually improve the overall system performance.

The major contributions of this thesis can be summarized as follows:

1) The development of both the tight and loose integration algorithms for the integrated PPP GPS/MEMS IMU system. The INS error states, which include the position error, velocity error, attitude error, sensor bias drift, sensor turn on bias and sensor scale factor, are estimated in the loosely coupled integrated system. For the tightly coupled system, the INS error states plus the states unique to PPP including the receiver clock offset and drift, tropospheric delay and ambiguities are estimated.

2) The development of a non-holonomic constraints aided inertial navigation algorithm. This algorithm is capable of improving attitude accuracies and mitigating the INS error accumulation during the GPS outages using vehicle dynamic knowledge. The navigation performance of MEMS IMU during complete and partial GPS outages is also evaluated.

3) The development of an inertial aided cycle slip detection and identification algorithm. The proposed algorithm uses Widelane phase and Extra-Widelane phase to detect and

identify the possible cycle slips due to their much longer wavelength compared to that of the L1and L2 phases.

### 1.4 Thesis Outline

Chapter Two provides an overview of GPS and INS. The available GPS measurements and different GPS error sources are reviewed. The Precise Point Positioning technology is also reviewed with an emphasis given on the error mitigation techniques and the observation models. Next, the focus is on the coordinate systems, INS mechanization and INS alignment of the Inertial Navigation System.

Chapter Three reviews the integration of GPS and INS, and the Kalman filtering theory. Different GPS and INS integration strategies are introduced, including the system design, advantages and disadvantages of each integration strategy. Following the discussion of GPS/INS integration, an overview of estimation theory and the Kalman filter algorithm are provided.

Chapter Four introduces the integrated PPP GPS/MEMS IMU system from the implementation point of view. The Precise Point Positioning technique, the tightly and loosely coupled integrated systems are described with the details of the Kalman filter design, which includes the filter states, the mathematical and the measurement models. Later, the 2D velocity constraints are described in details. The proposed algorithm of inertial aided cycle slip detection and identification is introduced at last.

Chapter Five presents two field tests and the analysis results. One field test is conducted under a relatively open sky environment, and the other one is carried out in a combined environment, which includes a relatively open sky environment and an urban canyon environment. The position, velocity and attitude error results are firstly presented. Then the GPS outages are simulated to evaluate the ability of MEMS IMU to bridge the GPS outages. The efficiency of the proposed inertial aided cycle slip detection and identification algorithm is verified at last.

Chapter Six summarizes the work presented in this thesis, and draw conclusions from the field test results and analysis. Then the recommendations for the future work are given.

# Chapter Two: Overview of Precise Point Positioning GPS and Inertial Navigation System

This chapter reviews the relevant characteristics of each system. It begins with an introduction of GPS including the GPS measurements and the various error sources that affect the GPS positioning accuracy. Then the Precise Point Positioning technology is reviewed, with details of the techniques used to mitigate the various error sources. Later, the principle of the INS is reviewed, including the different coordinate systems, INS mechanization, and the alignment procedures.

## 2.1 Overview of GPS

GPS is a satellite-based radio navigation system developed by the United States Department of Defense (DoD) to provide position, velocity and time (PVT) information in all weather conditions and at all times and anywhere on or near the earth. A comprehensive description of GPS could be found in Kaplan (1996), Parkinson and Spilker (1996), Hofmann-wellenhof et al. (2001).

Typically the following three types of measurements can be obtained from most GPS receivers.

- Pseudorange (code) measurements.
- Carrier phase (phase) measurements.
- Doppler measurements.

Pseudorange measurements are derived from the Pseudo-Random Noise (PRN) codes and are therefore classified according to code and frequency as L1-C/A, L1-P and L2-P (Petovello, 2003). The pseudorange measurement can be described by Equation (2.1) (Lachapelle, 2008).

$$P = \rho + d_{orb} + c(dt - dT) + d_{ion} + d_{trop} + \varepsilon(P) \tag{2.1}$$

where $P$ is the GPS pseudorange measurement, $\rho$ is the geometric range, $d_{orb}$ is the satellite orbital error, $c$ is the speed of the light, $dt$ and $dT$ are the satellite clock error and receiver clock error, respectively, $d_{ion}$ is the ionospheric delay, $d_{trop}$ is the tropospheric delay, and $\varepsilon(P)$ is a combination of code measurement noise and code multipath.

The carrier phase measurements are derived by measuring the phase of the incoming carrier in both L1 and L2 frequencies (Petovello, 2003). The carrier phase measurements in the unit of length can be described as Equation (2.2) (Lachapelle, 2008).

$$\Phi = \rho + d_{orb} + c(dt - dT) + \lambda N - d_{ion} + d_{trop} + \varepsilon(\Phi) \tag{2.2}$$

where $\Phi$ is the receiver measured carrier phase measurement, $\lambda$ is the wavelength of the carrier, $N$ is the ambiguity in the carrier phase measurement, and $\varepsilon(\Phi)$ is a combination of carrier phase noise and the carrier phase multipath.

The Doppler measurements are the derivatives of the carrier phase measurements with respect to time, which are caused by the relative motion between the GPS receiver and GPS satellite (Petovello, 2003). It can be described as Equation (2.3) (Lachapelle, 2008).

$$\dot{\Phi} = \dot{\rho} + \dot{d}_{orb} + c(\dot{dt} - \dot{dT}) - \dot{d}_{ion} + \dot{d}_{trop} + \varepsilon(\dot{\Phi}) \tag{2.3}$$

where $\dot{\Phi}$ is the measured Doppler measurement, $\dot{\rho}$ is the geometric range rate, $\dot{d}_{orb}$ is the orbital error drift, $\dot{dt}$ and $\dot{dT}$ are the satellite clock error drift and receiver clock error drift, respectively, $\dot{d}_{ion}$ is the ionospheric delay drift, $\dot{d}_{trop}$ is the tropospheric delay drift, and $\varepsilon(\dot{\Phi})$ is the Doppler measurement noise.

Autonomous point positioning or Standard Positioning Service (SPS) is vulnerable to the effect caused by the GPS related errors (Abdel-Salam, 2005). As indicated through Equation (2.1) to Equation (2.3), these GPS error sources include satellite orbit and clock errors, the errors caused by atmosphere propagation, such as ionospheric delay and tropospheric delay and the errors caused by site belongings and receiver firmware, such as multipath and noise. The common magnitudes of these errors are given in Table 2.1.

**Table 2.1 GPS error budget (Misra and Enge, 2001; Abdel-Salam, 2005)**

| Common Error Source | Error Magnitude |
|---|---|
| **Satellite Orbit** | ≈ 2 m |
| **Satellite Clock** | ≈ 2 m |
| **Ionospheric Delay** | ≈ 2 ~ 10 m at zenith |
| **Tropospheric Delay** | ≈ 2.3 ~ 2.5 m at zenith |
| **Multipath** | In a clean environment<br>code: 0.5 ~ 1 m<br>Carrier: 0.5 ~ 1 cm |
| **Receiver Noise** | Code: 0.25 ~ 0.5 m<br>Carrier phase: 1 ~ 2 mm |

Due to these GPS error sources, autonomous or standard point positioning can only result in the positioning accuracy at the level of several metres (Abdel-Salam, 2005). To achieve high accuracy positioning, techniques for error mitigation are necessary. The most common method to improve the positioning accuracy is the differential GPS, which requires a base station with precisely surveyed coordinates. However the requirement for a base station can be problematic for some applications, as it limits the operational range of the system and also increases the system cost and complexity. Due to these shortcomings of differential GPS, the Precise Point Positioning technique is developed to enable precise positioning using a single GPS receiver without the need for a base station (Abdel-Salam and Gao, 2003).

## 2.2 Overview of Precise Point Positioning GPS

With the advent of precise ephemerides and satellite clock corrections from IGS or other organizations, it is possible to conduct high precision GPS positioning using a single receiver without a need to use base stations, referred as the Precise Point Positioning (Zhang and Gao, 2007). This positioning method uses the un-differenced carrier phase observations as the primary observables and is able to provide centimetre or decimetre positioning accuracy (Gao and Shen 2001). Because of the un-differenced nature of PPP, all error sources associated with the space segment, propagation, environment and receiver need to take into account (Abdel-salam, 2005). Due to the lack of a base station, the error mitigations can be carried out by modeling, estimation and observation combination. The details of these error mitigation techniques are described as follows.

### *2.2.1 Satellite Orbit and Clock Errors*

The major errors associated with GPS satellites are uncertainties in satellite orbit and clock corrections broadcast from the satellites. The magnitudes of these errors are typically about 2 m for orbit and 7 ns for clock correction (Kaplan, 1996). With a global GPS station networks, the GPS satellite orbit and clock can be estimated with high accuracy (Zumberge et al., 1998). IGS provides the GPS satellite orbit and clock in different latencies and accuracies as shown in Table 2.2 (Abdel-salam, 2005). By using these precise GPS orbit and clock products, the uncertainties in the satellite orbit and clock corrections can be significantly reduced.

**Table 2.2 IGS products (Abdel-salam, 2005)**

| Data | Accuracy | | Latency | Interval | |
|---|---|---|---|---|---|
| | Orbit | Clock | | Orbit | Clock |
| **Final** | < 5 cm | ~ 0.1 ns | ~ 13 days | 15 minutes | 15 minutes |
| | | | | | 5 minutes |
| **Rapid** | < 5 cm | ~ 0.1 ns | ~ 17 hours | 15 minutes | 5 minutes |
| **Ultra rapid (observed)** | < 5 cm | ~0.2 ns | ~ 3 hours | 15 minutes | 15 minutes |
| **Ultra rapid (predicted)** | ~ 10 cm | 5 ns | Real time | 15 minutes | 15 minutes |

### *2.2.2 Tropospheric Delay*

Troposphere is the lower layer of atmosphere, and it extends from the sea level up to about 40 km (Skone, 2009). Due to its non-dispersive nature, the tropospheric delay is invariant to GPS frequencies. As a result, it cannot be mitigated by observation combination from different GPS frequencies. The tropospheric delay consists of two components, which are referred as the wet and dry components. The wet component, which contains most of the water vapor, represents 10% of the total tropospheric delay (Misra and Enge, 2001; Zhang and Gao, 2007; Tao, 2008), and it is caused by the lower portion of the troposphere. Due to the fact that the variation of the water vapor density is a function of position and time, the wet component is difficult to model (Tao, 2008). The dry component contains mainly gases, which can be easily modeled, and is caused by the higher portion of troposphere. It represents 90% of the total tropospheric delay. The wet and dry tropospheric delay are usually modeled at zenith and then mapped, using a

mapping function of the satellite elevation as described in Equation (2.4) (Zhang and Gao, 2007; Tao, 2008).

$$d_{trop} = d_{wet} M_{wet} + d_{dry} M_{dry} \tag{2.4}$$

where $d_{wet}$ is the zenith wet component, $M_{wet}$ is the wet mapping function, $d_{dry}$ is the zenith dry component, $M_{dry}$ is the dry mapping function.

Different models for the zenith wet and dry tropospheric delays and mapping functions based on theoretical and practical data are in use. The troposphere models include Saastamoinen, Hopfield, and Black-Eisner, while mapping functions include Davis, Chao, Marini and Niell (Tao, 2008). More details of these models and mapping functions can be found in Mendes and Langely (1994) and Tao (2008). In PPP, the dry component of the tropospheric delay is mitigated by modeling, since its modeling accuracy can achieve millimetre level (Zhang and Gao, 2007). The wet component of the tropospheric delay remains in the measurement equation and is estimated along with other parameters of interests.

### *2.2.3 Ionospheric Delay*

The ionosphere layer is the higher portion of the atmosphere, which is extending from about 40 km to 1000 km, and the ionosphere contains ionized particles created by the sun's ultraviolet radiation (Skone, 2009). Different from the troposphere, the ionosphere

is a dispersive medium, which means that it causes different magnitude of delays for GPS L1 and L2 frequencies. The density of ionized particles differs with height profile and can be illustrated as five layers: H, F2, F1, E and D (Skone, 2009). More details can be found in Klobuchar (1996) and Skone (2009).

Ionosphere advances the carrier phase but delays code observations with the same amount. As a result, the summation of the carrier phase and code measurement eliminates the ionospheric delay. For single frequency GPS users, the ionosphere models can be used to mitigate the ionospheric delay, although it can only alleviate part of the delays. For dual frequency GPS receivers, by using the dispersive nature of ionosphere, the ionospheric delay can be mitigated by observation combination. The ionospheric delay is related to the frequency that the signal travelled and the total electron content (TEC). The absolute TEC can be calculated based on the code observations from L1 and L2 frequencies, whereas a more accurate estimate but ambiguous can be derived from the carrier phase observations (Skone, 2009). The ambiguous nature is caused by the ambiguity in the carrier phase observations from L1 and L2 frequencies. The calculation procedure is described by Equation (2.5) and Equation (2.6).

$$TEC_a = \frac{f_1^2 f_2^2}{40.3(f_1^2 - f_2^2)}(P_1 - P_2 - (1 - \frac{f_1^2}{f_2^2})cT_{GD,r} + (1 - \frac{f_1^2}{f_2^2})cT_{GD,s}) \quad (2.5)$$

$$TEC_r = \frac{f_1^2 f_2^2}{40.3(f_1^2 - f_2^2)}(\Phi_1 + \lambda_1 N_1 - \Phi_2 - \lambda_2 N_2 + (1 - \frac{f_1^2}{f_2^2})cT_{GD,r}^{'} - (1 - \frac{f_1^2}{f_2^2})cT_{GD,s}^{'}) \quad (2.6)$$

where $a$ and $r$ represent the absolute and relative (with ambiguity unknown), respectively, $P_1$ and $P_2$ are the measured pseudorange on L1 and L2 frequencies, respectively, $\Phi_1$ and $\Phi_2$ are the measured carrier phase on L1 and L2 frequencies, respectively, $\lambda_1$ and $\lambda_2$ are the wavelength on L1 and L2 frequencies, respectively, $T_{GD,s}$ and $T_{GD,s}^{'}$ are the satellite inter-frequency bias in code and phase measurements, and $T_{GD,r}$ and $T_{GD,r}^{'}$ are the receiver inter-frequency bias in code and phase measurements.

Some other GPS common error sources, such as sagnac effect, relativity and receiver antenna phase center have been well discussed in a lot of publications and thus they are not discussed herein. The details can be found in Kaplan (1996), Parkinson and Spilker (1996).

There are several GPS related error sources that have not attracted as much attention as other error sources because these errors are relatively small or can be eliminated by differencing algorithm in differential GPS (Abdel-Salam, 2005). These error sources include the satellite antenna phase center offset, phase wind up, earth tide, ocean tide loading and atmosphere loading. However due to the un-differencing nature and the requirements of high positioning accuracy in PPP, these error sources must be considered. The details of these error sources can be found in Witchayangkoon (2000), Abdel-Salam et al. (2002), Bisnath and Langley (2001), Collins et al. (2001), Zumberge et al. (2001).

## 2.3 Overview of Inertial Navigation System

INS is a dead-reckoning navigation system which determines the attitude, velocity and position of a moving object from the knowledge of the previous states and the measurements obtained from an IMU (Schwarz and Wei, 2000). The IMU normally consists of three accelerometers and three gyroscopes, which provide measurements of specific force along its axes and measurements of rotation rate of the body with respect to the inertial reference frame, respectively. With the initial attitude information or the attitude estimates from the previous epoch and the measured rotation rate, the orientation of the object at the current epoch can be determined (Skaloud, 1999). By using the attitude information, accelerometer measurements can be transformed to an appropriate frame of interest thus to determine the translational motion of the moving body within that frame after the integration process takes place. Given the knowledge of the initial velocity and position, the trajectory of a moving object with respect to a reference frame can be determined (Park, 2004).

### *2.3.1 Coordinates Frames and Transformations*

The INS typically requires transformation between different coordinate systems. The most common used coordinate systems are Inertial Frame, Earth Centered Earth Fixed Frame, Local Level Frame and Body Frame, which are described as follows.

**Inertial Frame (i-frame):** it is a non-rotating and non-accelerating frame with respect to fixed stars. The inertial frame is defined as follows:

Origin: Earth's centre of mass

$Z^i$ –Axis : Parallel to the spin axis of the Earth

$X^i$ –Axis : Pointing towards the mean vernal equinox

$Y^i$ –Axis : Orthogonal to X and Z completing a right-handed system

**Earth Centered Earth Fixed (ECEF or e-frame):** it is defined as follows (Figure 2.1):

Origin : Earth's centre of mass

$Z^e$ –Axis : Parallel to the mean spin axis of the Earth

$X^e$ –Axis : Pointing towards the mean meridian of Greenwich

$Y^e$ –Axis : Orthogonal to X and Z completing a right-handed system

**Local Level Frame (LLF or l-frame):** it is a local geodetic frame as shown in Figure 2.1, it can be defined as

Origin : Coinciding with sensor frame

$Z^l$ –Axis : Orthogonal to reference ellipsoid pointing up

$X^l$ –Axis : Pointing towards geodetic east

$Y^l$ –Axis : Pointing towards geodetic north

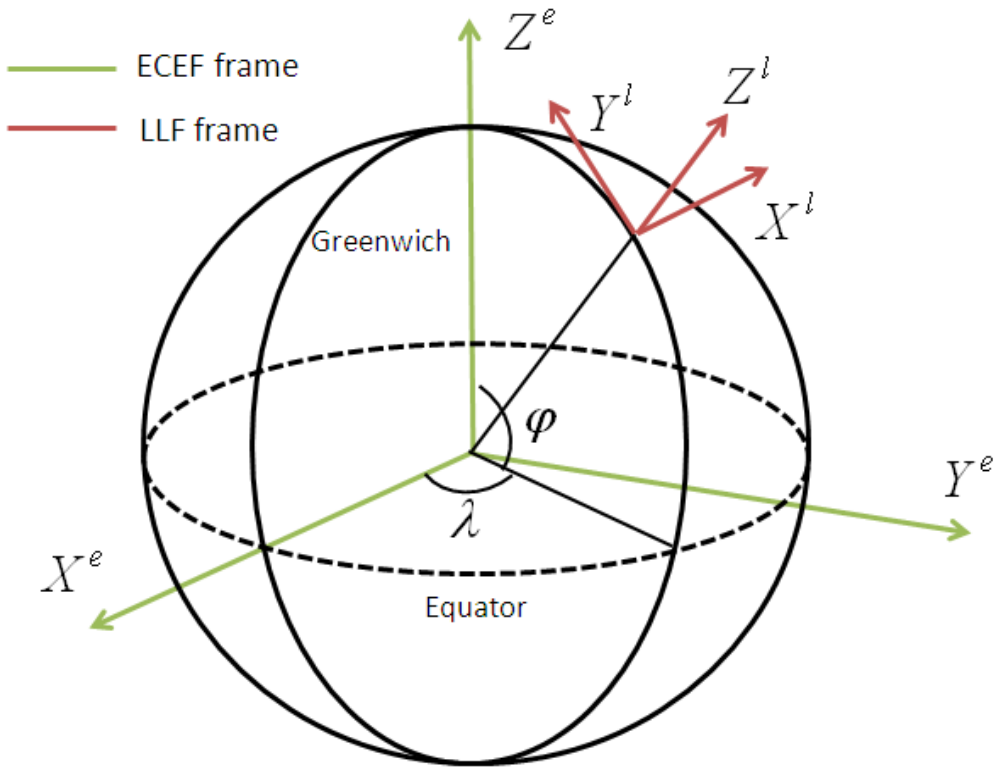


**Figure 2.1 ECEF and LLF frames**

**Body Frame (b-frame):** it is an orthogonal frame, whose axes coincide with the axis of the IMU. The body frame is assumed to be aligned with the vehicle frame as shown in Figure 2.2 and can be defined as follows:

Origin : Centre of the IMU

$X^b$ –Axis : Pointing towards the right of the vehicle

$Y^b$ –Axis : Pointing towards the forward direction

$Z^b$ –Axis : Orthogonal to the X and Y axes to complete a right-handed system

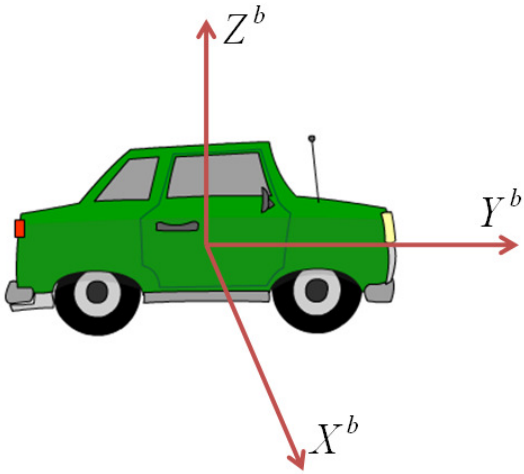


**Figure 2.2 Body frame**

The transformation between e-frame and l-frame can be performed by two consecutive rotations around the X and Z axes of the ECEF frame, and can be described by Equation (2.7) (Schwarz and Wei, 2000; Jekeli, 2000).

$$R_e^l = R_1(\frac{\pi}{2} - \varphi)R_3(\frac{\pi}{2} + \lambda) \tag{2.7}$$

where $\varphi$ is the latitude, $\lambda$ is the longitude, $R_e^l$ is the rotation matrix from e-frame to l-frame, and $R_1, R_3$ are the rotation matrices about X and Z axes, respectively.

The transformation between b-frame and l-frame can be performed by three consecutive rotations around Y, X and Z axes, and can be described Equation (2.8) (Schwarz and Wei, 2000; Jekeli, 2000).

$$R_b^l = R_3(\psi)R_1(\theta)R_2(\phi) \tag{2.8}$$

where $\psi$ is the azimuth angle, $\theta$ is the pitch angle, $\phi$ is the roll angle, and $R_b^l$ is the transformation matrix from b-frame to the l-frame.

The transformation between the b-frame and e-frame can be obtained by the two consecutive rotations as described by Equation (2.9) (Schwarz and Wei, 2000; Jekeli, 2000).

$$R_b^e = R_l^e R_b^l = (R_e^l)^T R_b^l \tag{2.9}$$

### *2.3.2 INS Mechanization*

INS mechanization is the algorithm that derives the current position, velocity and attitude solutions from the measurements of an IMU (Edwan et al., 2009). Normally, the mechanization algorithm can be carried out in both e-frame and l-frame. In this study, the INS mechanization is carried out in l-frame.

Generally, the INS mechanization can be concluded as two steps. In the first step, the measured rotation rate along with the attitude of previous epoch or the initial attitude obtained by INS alignment (will be reviewed in the later section) are used to calculate the current attitude. The effect caused by the earth rotation and the change of orientation of l-

frame should be compensated in this step. Then based on the calculated attitude information, the specific force measured by the accelerometers can be transformed to the navigation frame of interest, in which the position and velocity can be obtained by integrating the specific force once and twice, respectively. Figure 2.3 summarizes the scheme of INS mechanization implemented in l-frame.

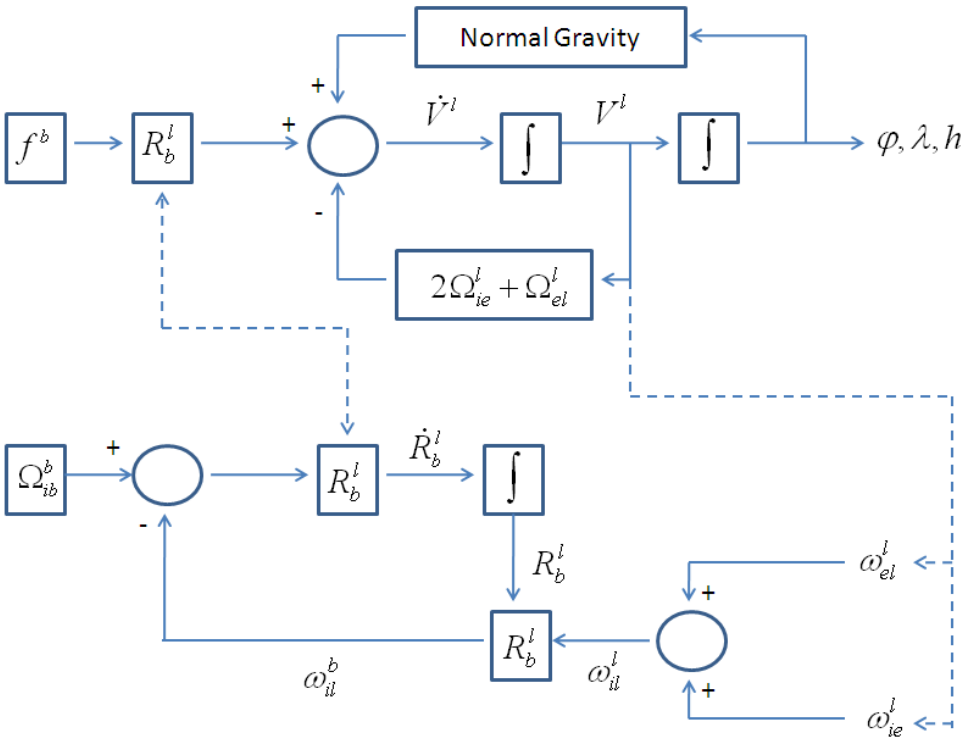


**Figure 2.3 Scheme of INS mechanization in the local-level frame (Schwarz and Wei, 2000)**

The INS mechanization algorithm can be mathematically described by Equation (2.10) (El-Sheimy, 2007).

$$\begin{bmatrix} \dot{r} \\ \dot{v} \\ \dot{R}_b^l \end{bmatrix} = \begin{bmatrix} D^{-1}v^l \\ R_b^l f^b - (2\Omega_{ie}^l + \Omega_{el}^l)v^l + g^l \\ R_b^l(\Omega_{ib}^b - \Omega_{il}^b) \end{bmatrix} \tag{2.10}$$

where dot represents the time derivatives, and the superscript 'l' and 'b' represent the l-frame and b-frame, respectively, $D^{-1} = \begin{bmatrix} 0 & \frac{1}{R_m + h} & 0 \\ \frac{1}{(R_n + h)\cos\varphi} & 0 & 0 \\ 0 & 0 & 1 \end{bmatrix}$ is the relationship matrix between the position rate and velocity in l-frame, $R_m$ is the meridian radius of the earth curvature, $R_n$ is the prime vertical radius of the earth curvature, $r^l = [\varphi \quad \lambda \quad h]$ is the position vector, $v^l = [v^E \quad v^N \quad v^U]^T$ is the velocity vector in the l-frame, $f^b$ is the specific force vector measured from the IMU accelerometer triad, $g^l = [0 \quad 0 \quad -g]$ is the earth's local gravity vector, g can be obtained from a normal gravity model, $\Omega_{ab}^c$ is the skew-symmetric matrix of the rotation rate $\omega_{ab}^c$, which represents the rotation rate from frame 'b' relative to frame 'a', expressed in frame 'c', $\omega_{ib}^b$ is the angular rate vector sensed by the gyroscope triad, $\omega_{ie}^l$ and $\omega_{el}^l$ are the earth rotation rate projected in the l-frame and the transport rate caused by the change of orientation of the l-frame, respectively, $\omega_{il}^l$ is the sum of the $\omega_{ie}^l$ and $\omega_{el}^l$.

It can be noted that Equation (2.10) represents the INS mechanization in the continuous-time domain. Due to the fact that the INS mechanization algorithm is mostly implemented in the computer, the equations of INS mechanization in continuous-time domain need to be converted to discrete-time domain. Instead of outputting the specific force and rotation rate, most IMUs actually output the velocity increment and angular increment over the sample period (Li, 2009).

Normally the INS mechanization in discrete-time domain can be implemented as following steps: sensor error compensation, attitude update and position update (El-Sheimy, 2007; Li, 2009), which are reviewed in details as follows.

Sensor Error Compensation

The raw IMU measurements are typically corrupted with inertial sensor errors, such as biases, scale factors. Normally these errors can be calibrated in the laboratory or can be estimated along with other parameters of interests. Once obtained the corrections of the sensor errors, the raw IMU measurements can be compensated as Equation (2.11) and Equation (2.12) (Li, 2009).

$$\Delta v_f^b = \frac{\Delta \tilde{v}_f^b + b_a \Delta t}{1 + S_a} \tag{2.11}$$

$$\Delta \theta_{ib}^b = \frac{\Delta \tilde{\theta}_{ib}^b + b_g \Delta t}{1 + S_g} \tag{2.12}$$

where '~' represents the raw IMU measurements corrupted with sensor errors, $\Delta v_f^b$ is the velocity increment, $\Delta\theta_{ib}^b$ is the angular increment, $b_g$ is the gyroscope drift, $b_a$ is the accelerometer bias, $S_g$ is the scale factor in gyroscope, $S_a$ is the scale factor in accelerometer and $\Delta t$ is the sample period.

Attitude Update

The angular increment obtained from an IMU is measured in the body frame with respect to the inertial frame. The body angular increment with respect to the navigation frame can be obtained by Equation (2.13) (El-Sheimy, 2007; Li, 2009)

$$\Delta\theta_{lb}^b = \Delta\theta_{ib}^b - R_l^b \omega_{il}^l \Delta t = \begin{bmatrix} \Delta\theta_x & \Delta\theta_y & \Delta\theta_z \end{bmatrix}^T \tag{2.13}$$

Based on the body angular increment with respect to the navigation frame, the updated transformation matrix from the body frame to the navigation frame can be obtained by using quaternion parameters as shown in Equation (2.14) (El-Sheimy, 2007).

$$Q_{k+1} = Q_k + \frac{1}{2}\Omega Q_k \tag{2.14}$$

where $\Omega$ is the skew-symmetric matrix of the angular increment vector obtained in Equation (2.13).

The conversion between the quaternion parameters and transformation matrix $R_b^l$ can be described by Equation (2.15) and (2.16) (El-Sheimy, 2007).

$$R_b^l = \begin{bmatrix} q_1^2 - q_2^2 - q_3^2 + q_4^2 & 2(q_1q_2 - q_3q_4) & 2(q_1q_3 + q_2q_4) \\ 2(q_1q_2 + q_3q_4) & -q_1^2 + q_2^2 - q_3^2 + q_4^2 & 2(q_2q_3 - q_1q_4) \\ 2(q_1q_3 - q_2q_4) & 2(q_2q_3 + q_1q_4) & -q_1^2 - q_2^2 + q_3^2 + q_4^2 \end{bmatrix} \tag{2.15}$$

$$Q = \begin{bmatrix} q_1 \\ q_2 \\ q_3 \\ q_4 \end{bmatrix} = \begin{bmatrix} 0.25(R_{32} - R_{23}) / q_4 \\ 0.25(R_{13} - R_{31}) / q_4 \\ 0.25(R_{21} - R_{12}) / q_4 \\ 0.5\sqrt{1 + R_{11} + R_{22} + R_{33}} \end{bmatrix} \tag{2.16}$$

where $R_{ij}$ is the element at the i$^{th}$ row and j$^{th}$ column of the transformation matrix from the b-frame to the l-frame.

The use of quaternion parameters for attitude update has the advantages such as robustness against singularities and computational efficiency. More details can be found at Savage (2000) and Jekeli (2001). The attitude solution can be derived from the transformation matrix from b-frame to l-frame through Equation (2.17) to Equation (2.19) (El-Sheimy, 2007).

$$\phi = -\tan^{-1}\left(\frac{R_{31}}{R_{33}}\right) \tag{2.17}$$

$$\theta = \sin^{-1}(R_{32}) \tag{2.18}$$

$$\psi = \tan^{-1}(\frac{R_{12}}{R_{22}}) \tag{2.19}$$

Position Update

As discussed before, the raw velocity increment obtained from an IMU is measured in the body frame, which needs to be transformed to the navigation frame. Given the updated transformation matrix from the b-frame to the l-frame, the velocity increment can be obtained through Equation (2.20) (El-Sheimy, 2007;). The Coriolis and gravity correction need to be applied when calculate the velocity increment in the l-frame.

$$\Delta v^l = R_b^l \Delta v_f^b - (2\Omega_{ie}^l + \Omega_{el}^l) v^l \Delta t + g^l \Delta t \tag{2.20}$$

Based on the velocity increment in the l-frame, the velocity and position can be updated through Equation (2.21) and Equation (2.22) (El-Sheimy, 2007; Shin, 2001), respectively.

$$v_{k+1}^l = v_k^l + \Delta v^l \tag{2.21}$$

$$r_{k+1}^l = r_k^l + \frac{1}{2} D^{-1} (v_{k+1}^l + v_k^l) \Delta t \tag{2.22}$$

It can be seen that the current position, velocity and attitude solutions are calculated based on the previous solution and the measurements from the IMU. As a result, any error in the previous solutions or in the IMU measurements will affect the current

position accuracy and eventually accumulates, thus the inertial navigation system is vulnerable to the sensor biases and it must be periodically corrected by the external source, such as GPS or other sensors (Shin et al., 2005; Stephen, 2000).

### *2.3.3 INS Initial Alignment*

As discussed before, the initial attitude is necessary to the INS mechanization. This section reviews the INS initial alignment, from which the initial attitude can be derived. Generally, the initial alignment can be implemented as horizontal alignment and heading alignment.

Horizontal Alignment

An initial estimate of the roll and pitch is obtained through the horizontal alignment, which can also be referred as accelerometer leveling. The principle of horizontal alignment is using the knowledge of the gravity sensed by each accelerometer under static conditions to derive the estimates of pitch and roll, which can be described as Equation (2.23) and Equation (2.24) (Godha, 2006).

$$\theta = \sin^{-1}\left(\frac{\Delta\bar{v}_y^b}{g\Delta t}\right) \tag{2.23}$$

$$\phi = -\sin^{-1}\left(\frac{\Delta\bar{v}_x^b}{g\Delta t}\right) \tag{2.24}$$

Where the ‘bar’ above a quantity represents a time average. The accuracies of these estimates primarily depend on the accelerometer biases (El-Sheimy, 2007). The accelerometer leveling error estimation sensitivity to accelerometer bias is 0.06 deg/mg (Godha, 2006).

## Heading Alignment

An initial estimate of the azimuth can be determined by the heading alignment, which can also be referred as the gyro compassing. Normally this method can only be used for the tactical grade or higher grade IMUs, since it uses knowledge of the Earth rotation rate sensed by each gyro under static conditions to derive the azimuth estimate. For MEMS IMU, the Earth rotation rate cannot be detected due to the significant sensor errors (Farrell and Barth, 2001). As a result, the gyro compassing cannot be implemented with MEMS IMU. Normally the initial estimate of azimuth is obtained from external source when the low cost MEMS IMU is used.

# Chapter Three: Integration of GPS and INS

Having reviewed the major aspects of GPS and INS in the previous chapter, this chapter discusses the integration of the two systems. In particular it describes the loose and tight integration strategies. Then the estimation and filtering theory, which are used to fuse the GPS and INS data, are given.

## 3.1 GPS/INS Integration Strategies

There are several strategies that can be used for GPS and INS integration. The following three strategies are the most common.

- Loose Integration
- Tight Integration
- Deep/Ultra-Tight Integration

In deep/ultra-tight integration strategy the GPS updates are used to calibrate the INS, while the INS is used to assist the GPS receiver tracking loops during interference or degraded signal conditions (Sennott and Senffner, 1997; Petovello, 2003). However, this strategy requires access to the receiver's firmware. Thus the deep/ultra-tight integration strategy is normally implemented by the equipment manufacturers (Petovello, 2003), and therefore, it is not discussed herein.

The loose and tight integration strategies are the most commonly used integration strategies for the integrated GPS/INS system at the user level. In both cases, the GPS receiver and the IMU are two separate units. They mainly differ in the type of information that is shared between the individual systems (Petovello, 2003; El-Sheimy, 2007). Each strategy is described in details as follows.

### *3.1.1 Loose Integration Strategy*

In the loose integration, the GPS and INS mechanization are carried out independently. Together these constitute a decentralized filter process; therefore, this strategy is also referred as a decentralized integration strategy (Wang and Wilson, 2002; Wang, 2004). Figure 3.1 shows the integration scheme of the loose integration strategy.

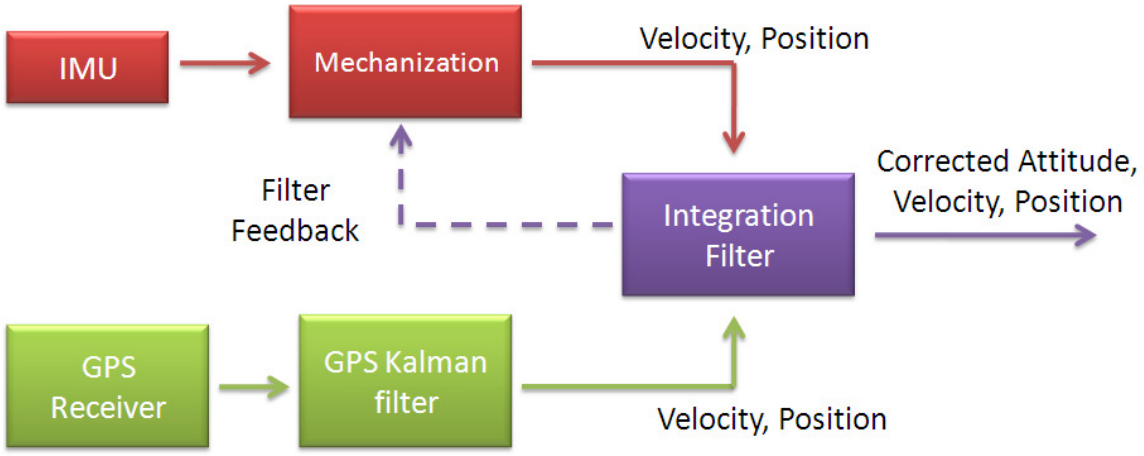


**Figure 3.1 Scheme of loose integration**

As illustrated in the figure, the raw GPS measurements are processed in a GPS-only Kalman filter to derive the position and velocity solutions. Meanwhile, the raw IMU data is processed through the mechanization algorithm to compute the attitude, position, and velocity navigation solutions. Then the INS-derived position and velocity are differenced with the GPS-derived position and velocity. The integration filter processes the position and velocity residuals to estimate the error states and then output the corrected position, velocity and attitude solutions. It is worthy to mention that the full position and velocity variance-covariance matrix is needed to generate the measurement noise matrix for the integration filter to make sure that the correlation between the velocity update and position update is properly accounted.

There are two implementation approaches for the integrated GPS/INS system, which can be referred as open loop and closed loop approaches. With the open loop approach, the INS mechanization operates independently without getting any error compensation from the Integration filter. While in the closed loop approach the integration filter feedbacks the estimated error states to the INS mechanization to compensate the sensor errors of the IMU, as shown in the dot line in Figure 3.1. Usually the open loop approach is valid for high end inertial sensors, such as navigation grade IMU and tactical grade IMU, which propagate small errors because of their superior error characteristics. However, it is not suitable for low cost MEME IMU, which propagates large errors in a small time interval due to the significant sensor errors. The reason is that without the error compensation from the integration filter, the INS mechanization error accumulates rapidly and becomes very significant for MEMS IMU, which spoils the small error assumption made in the

INS error model, and thus potentially degrades the system performance (Wang et al., 2003; Zhang et al., 2003). As a result, the closed loop approach is normally adopted to compensate the sensor errors when low cost MEMS IMU is used.

The loose integration strategy is common to use due to its faster processing, simplicity of implementation and robustness. The primary disadvantage of this strategy is that the integrated system provides typically poor solution during the periods of partial GPS availability (typically less than 4 satellites are available) and the tightly coupled integrated system normally outperforms it under such environments (Hide and Moore, 2005). Petovello (2003) identified one specific problem with loose integration strategy that the processing noise has to be added to both of the filters because the system has two independent filters. The extra processing noise in the GPS filter used to compensate the user's dynamics would have also negative effect on the state estimation.

### *3.1.2 Tight Integration Strategy*

Different from the loose integration strategy, both the raw GPS measurements, such as pseudorange, carrier phase and Doppler measurements, and INS data are processed centrally in one common filter; therefore, this integration strategy is also referred as a centralized integration scheme, which is illustrated in Figure 3.2.

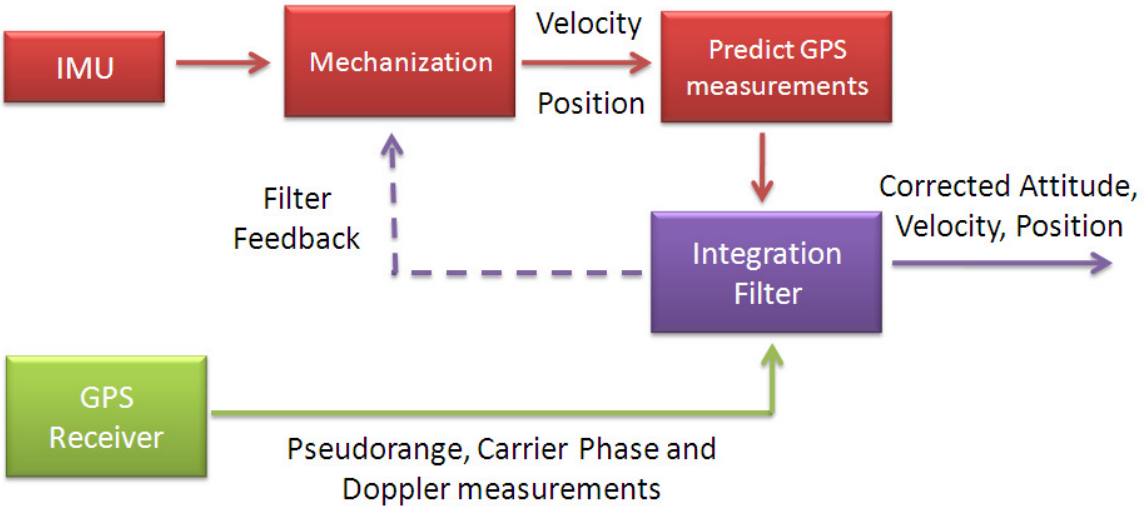


**Figure 3.2 Scheme of tight integration**

As shown in the figure, the position and velocity outputs of the INS mechanization are not directly used in the integration filter; instead they are used to predict the GPS measurements, such as the pseudorange, carrier phase and Doppler measurements. Later, the collected GPS raw measurements from the receiver are differenced with the INS predicted measurements. The integration filter then directly processes those measurement residuals to estimate the error states and then output the corrected attitude, position and velocity solutions. Similar to the loose integration strategy, the open loop and closed loop approaches can be implemented. Since the GPS updates used in the tight integration are the raw GPS measurements, the measurement noise matrix of the integration filter is the same as the normally used noise matrix in GPS filters, which has been well investigated in Tiberius (1999), Collins and Langley (1999).

The tight integration strategy is preferred to use in the urban environments, in which the number of the tracked satellites is frequently less than 4, because the INS can still be updated with the available GPS measurements. In addition, because no additional processing noise is present in the single filter and the GPS measurements used to update the filter are more statistically independent, this strategy offers better accuracy on the state estimation (Wang and Gao, 2003). However comparing to the loose integration strategy, the increased size of the state vector leads to an increased computational burden (Petovello, 2003).

### 3.2 Kalman Filtering

Estimation is to obtain a set of values for a set of unknown parameters and their properties from a redundant (non-deterministic) set of observations (Gao, 2008). The Kalman filter is one of the most common estimation methods. It is an optimal data processing algorithm that processes all available measurements regardless of their precision, to estimate the current values of the variables of interests, with the use of 1) knowledge of the system dynamics 2) the statistical description of the system noises, measurement errors, and uncertainties in the dynamic models, and 3) any available information about the initial conditions of the variables of interests (Maybeck, 1979; Gao 2008). More details can be found in Gelb (1974), Brown and Hwang (1992), and Grewal et al. (2001).

The basic Kalman filter is limited to a linear system, though most realistic systems are non-linear, such as the integrated GPS/INS system. Linearization of the non-linear model

is required in case of applying the Kalman filter to these systems. A filter where linearization is done about the predetermined nominal state vector is referred as a Linearized Kalman filter (LKF), and if the linearization is done based on the states from the previous epoch, the filter is referred as an Extended Kalman filter (EKF) (Gelb, 1974). The latter one is a more common procedure.

The non-linear system can be described by Equation (3.1) (Gelb, 1974; Gao, 2008).

$$\dot{x}(t) = f(x(t),t) + G(t)w(t) \tag{3.1}$$

where $x(t)$ is the system states, $f(x(t),t)$ is the non-linear function representing the temporal behavior of the system states, $G(t)$ is the shaping matrix and $w(t)$ is a noise vector.

The noise vector $w(t)$ in Equation (3.1) is assumed to be a Gaussian distributed noise with a mean value of zero. Its covariance matrix can be obtained through Equation (3.2) (Gelb, 1974; Gao, 2008).

$$E\{w(t)w(t)^T\} = Q(t)\delta(t) \tag{3.2}$$

where $Q(t)$ is the spectral density matrix of $w(t)$, and the $\delta(t)$ represents the Dirac delta function.

In the linearization process, a nominal trajectory $x^*(t)$ is selected, and then the system states can be written as Equation (3.3) (Gelb, 1974; Gao, 2008).

$$x(t) = x^*(t) + \delta x(t) \tag{3.3}$$

where $\delta x(t)$ is a perturbation from the nominal trajectory.

By applying the Taylor series expansion and neglect the second and higher order terms, the linearized continuous-time system is described by Equation (3.4) (Gelb, 1974; Gao, 2008).

$$\delta \dot{x}(t) = F(t)\delta x(t) + G(t)w(t) \tag{3.4}$$

where $F(t)$ is the system dynamic matrix.

As it can be noted, the Kalman filter actually estimates perturbations from the nominal trajectory after linearization. For the case of applying Kalman filter to the integrated GPS/INS system, the most common method is the EKF, which can be implemented as: first use the last Kalman filter estimate as the linearization point to linearize the non-linear model, then applying the standard Kalman filter.

Normally the Kalman filter estimation algorithm is implemented on a computer and the continuous-time system equations need to be transformed to their corresponding discrete-time form. The Equation (3.4) can be transformed to the discrete-time form as described in Equation (3.5) (Gelb, 1974; Gao, 2008).

$$\delta x_k = \Phi_{k,k-1}\delta x_{k-1} + G_{k-1}w_{k-1} \tag{3.5}$$

where $\Phi_{k,k-1}$ is the state transition matrix, $\delta x_k$ is the system state vector at $t_k$ and $w_{k-1}$ is the driving noise during $\Delta t_k = t_k - t_{k-1}$

If $\Delta t_k$ is very small or $F(t)$ is approximately constant over $\Delta t_k$, the transition matrix can be described by Equation (3.6) (Gelb, 1974; Gao, 2008).

$$\Phi_{k,k-1} = e^{F(t_{k-1})\Delta t_k} \approx I + F(t_{k-1})\Delta t_k \tag{3.6}$$

Based on the assumption, $w_k$ is a white sequence and obeys the following conditions, which can be described by Equation (3.7) and Equation (3.8) (Gelb, 1974; Gao, 2008).

$$E[w_k] = 0 \tag{3.7}$$

$$E[w_k w_i^T] = \begin{cases} Q_k, i = k \\ 0, i \neq k \end{cases} \tag{3.8}$$

By applying a trapezoidal integration, $Q_k$ can be described by Equation (3.9) (Shin, 2005).

$$Q_k \approx \frac{1}{2}\left[\Phi_{k+1,k} G(t_k) Q(t_k) G^T(t_k) \Phi_{k+1,k}^T + G(t_{k+1}) Q(t_{k+1}) G^T(t_{k+1})\right]\Delta t_{k+1} \tag{3.9}$$

For the case of the integrated GPS/INS system, the non-linearity is associated with not only the system model but also the measurement model. After applying the linearization to the measurement model, the measurement equation about the nominal trajectory in discrete-time form is described in Equation (3.10) (Gelb, 1974; Gao, 2008).

$$\delta Z_k = H_k \delta x_k + v_k \tag{3.10}$$

where $\delta Z_k$ is the measurement error vector, $H_k$ is the design matrix and $v_k$ is the measurement noise.

If we assume the measurement noise $v_k$ is a white sequence, then it obeys the following conditions, which can be described in Equation (3.11) and Equation (3.12) (Gelb, 1974; Gao, 2008).

$$E\{v_k\} = 0 \tag{3.11}$$

$$E\{v_k v_i^T\} = \begin{cases} R_k, i = k \\ 0, i \neq k \end{cases} \tag{3.12}$$

The system noise $w_k$ and measurement noise $v_k$ are assumed to be uncorrelated, which means $E\{w_k v_j^T\} = 0$, for all $j,k$.

The covariance matrix of the error state vector is defined as Equation (3.13) (Gelb, 1974; Gao, 2008).

$$E\{(\delta\hat{x}_k - \delta x_k)(\delta\hat{x}_k - \delta x_k)^T\} = P_k \tag{3.13}$$

As introduced before, a Kalman filter is a recursive data processing algorithm that consists of a series of prediction and update steps. The implementation procedure is illustrated in Figure 3.3 (Gao, 2008). An initial state estimate $\delta\hat{x}_{k-1}$ at time $t_{k-1}$ and its variance-covariance matrix are needed to compute the Kalman gain at the first place. Then the update procedure is implemented based on the calculated Kalman gain. The state estimate of the next epoch is calculated in the prediction step based on the updated state estimate at the current epoch.

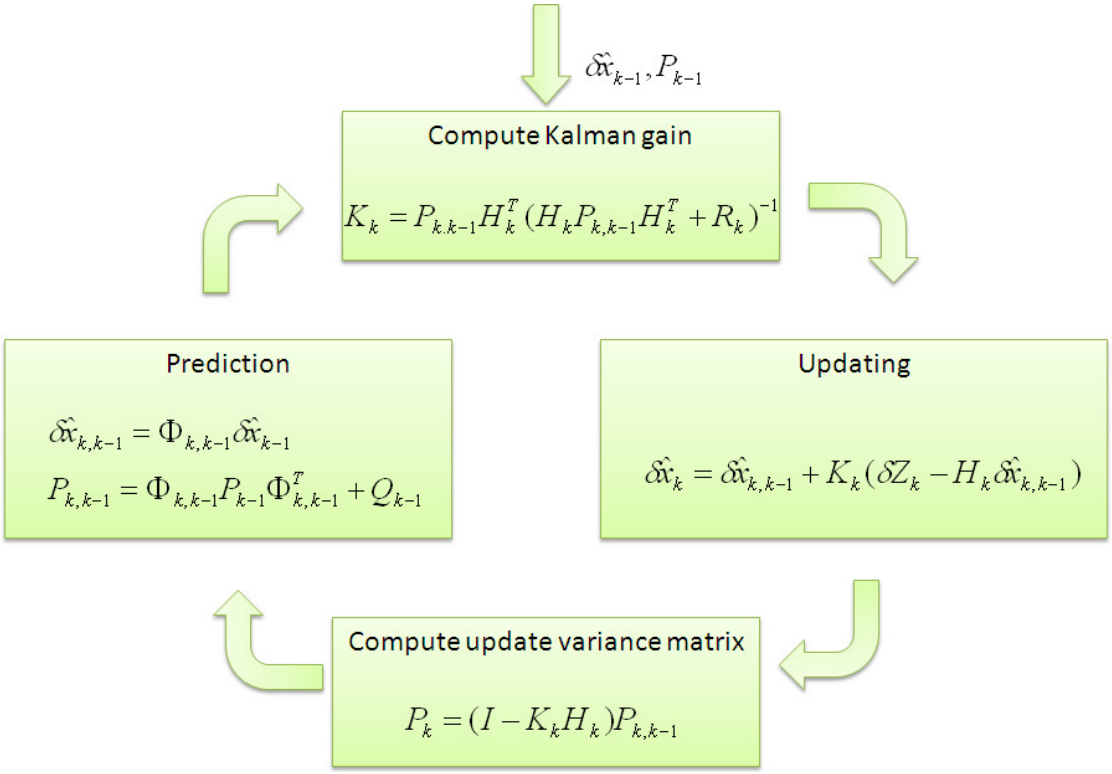


**Figure 3.3 Computation procedure of Kalman filter (Gao, 2008)**

In the prediction step, a state estimate $\delta\hat{x}_{k,k-1}$ at time $t_k$ is computed by using the transition matrix, which can be described in Equation (3.14) (Gelb, 1974; Gao, 2008).

$$\delta\hat{x}_{k,k-1} = \Phi_{k,k-1}\delta\hat{x}_{k-1} \tag{3.14}$$

The corresponding covariance matrix can be calculated based on the transition matrix and the updated matrix $P_{k-1}$ at $t_{k-1}$, which can be described in Equation (3.15) (Gelb, 1974; Gao, 2008).

$$P_{k.k-1} = \Phi_{k,k-1} P_{k-1} \Phi^T_{k,k-1} + Q_{k-1} \tag{3.15}$$

In the update step, the Kalman gain matrix $K_k$ is firstly computed by Equation (3.16) (Gelb, 1974; Gao, 2008).

$$K_k = P_{k,k-1} H_k^T (H_k P_{k,k-1} H_k^T + R_k)^{-1} \tag{3.16}$$

Based on the calculated Kalman gain matrix, the state from the prediction step and the input measurement, the updated estimate is derived as shown in Equation (3.17) (Gelb, 1974; Gao, 2008).

$$\delta\hat{x}_k = \delta\hat{x}_{k,k-1} + K_k (\delta Z_k - H_k \delta\hat{x}_{k,k-1}) \tag{3.17}$$

The updated variance-covariance matrix at time $t_k$ is calculated by Equation (3.18) (Gelb, 1974; Gao, 2008).

$$P_k = (I - K_k H_k) P_{k,k-1} \tag{3.18}$$

# Chapter Four: Integration of Precise Point Positioning GPS and Low Cost MEMS IMU

This chapter mainly discusses the theoretical and practical aspects of the integration of the PPP GPS and the low cost MEMS IMU. As discussed in the previous chapter, the Kalman filtering is used to fuse the GPS and the MEMS IMU data. The chapter begins with a discussion of the PPP filter, which includes the system model and the measurement model. Then different Kalman filter designs for both loosely and tightly coupled integrated PPP GPS/MEMS IMU system are introduced. Later, the 2D velocity constraints are discussed in details. The proposed algorithm of inertial aided cycle slip detection and identification is described at last.

## 4.1 Precise Point Positioning GPS Filter

Precise Point Positioning technique is a positioning methodology, which processes the GPS data from a single dual-frequency GPS receiver and using the precise GPS orbit and clock products to derive high quality position solution with centimetre to decimetre level accuracy. In this study, the Precise Point Positioning technique is carried out using the Kalman filtering.

### *4.1.1 System States*

Considering that the designed integrated PPP GPS/MEMS IMU system is normally used for high dynamic applications, the well-known position-velocity model is adopted for the PPP filter in this study. Based on the chosen system model, six system states are used and

parameterized in a local-level frame, which are latitude, longitude and height errors and three velocity error states in east, north and up directions.

As introduced in Chapter 2, there are two observation models in PPP GPS, namely the traditional model and the UofC model. Although the two observation models provide similar positioning accuracy, the UofC model was proposed to support the resolution of the integer ambiguities as L1 and L2 ambiguity parameters can be estimated separately. Only the traditional model is used in this study since integer ambiguity resolution is not the focus of this thesis. The satellite orbit error and clock error are eliminated by using the precise GPS clock and orbit products, the first order ionospheric delay is mitigated by using the ionosphere-free combination, and the dry component of the tropospheric delay is mitigated by modeling. So the rest errors in the GPS measurements are the GPS receiver clock offset and the wet tropospheric delay component, which are estimated along with the other parameters of interests. The ambiguity terms for different satellites in view are also estimated in the Kalman filter and treated as float values. Finally the system states for PPP filter include 3 position error states, 3 velocity error states, the receiver clock offset and drift, the wet tropospheric delay and the ambiguity terms, which can be described by Equation (4.1)

$$x_{GPS} = [\delta r^l, \delta v^l, dT, d_{dT}, d_{trop}, N_{IF_1}, N_{IF_2} \cdots N_{IF_n}] \tag{4.1}$$

where IF represents the ionosphere-free combination, n represents the number of satellites in view; $\delta r^{l} = [\delta\varphi \quad \delta\lambda \quad \delta h]$ is the position error state vector in the l-frame, $\delta\varphi, \delta\lambda, \delta h$ are the latitude, longitude and height error states, respectively; $\delta v^{l} = [\delta v_E \quad \delta v_N \quad \delta v_U]$ is the velocity error vector in the l-frame, $\delta v_E, \delta v_N, \delta v_U$ represent the velocity errors in east, north and up directions, respectively; $dT$ represents the receiver clock offset and $d_{dT}$ represents the receiver clock drift; $d_{trop}$ represents the wet component of the tropospheric delay.

### *4.1.2 System Model*

The nature of the system states dictates the suitable modeling process. Based on the chosen system model, the transition matrix in PPP filter can be described as Equation (4.2). The corresponding system states are given in Equation (4.1).

$$\Phi = \begin{bmatrix} I_{3\times3} & M & 0 & 0 & 0 & 0 \\ 0 & I_{3\times3} & 0 & 0 & 0 & 0 \\ 0 & 0 & 1 & \Delta t & 0 & 0 \\ 0 & 0 & 0 & 1 & 0 & 0 \\ 0 & 0 & 0 & 0 & 1 & 0 \\ 0 & 0 & 0 & 0 & 0 & I_{n\times n} \end{bmatrix} \tag{4.2}$$

where $M = \begin{bmatrix} 0 & \frac{\Delta t}{(R_m + h)} & 0 \\ \frac{\Delta t}{(R_n + h)\cos(\varphi)} & 0 & 0 \\ 0 & 0 & \Delta t \end{bmatrix}$ is the relationship matrix between the position errors and the velocity errors in the l-frame; $R_m$ and $R_n$ are the earth radius in meridian and prime meridian directions, respectively; $\Delta t$ is the Kalman filter time interval.

With the position-velocity system model, the velocity errors are modeled as random walk processes, as well as the receiver clock drift and the wet component of tropospheric delay. The ambiguity states are assumed to be constants since they remain unchanged if no cycle slips over time. Based on the random process modeling for the system states, the noise matrix Q is given herein. For the purpose of illustration, the structure of the noise matrix is divided into sub-blocks, in which each block represents a set of related parameters, such as position error block, receiver clock error block, tropospheric delay block and ambiguities block (Abdel-Salam, 2005). Figure 4.1 shows the structure of the noise matrix used in the PPP filter.

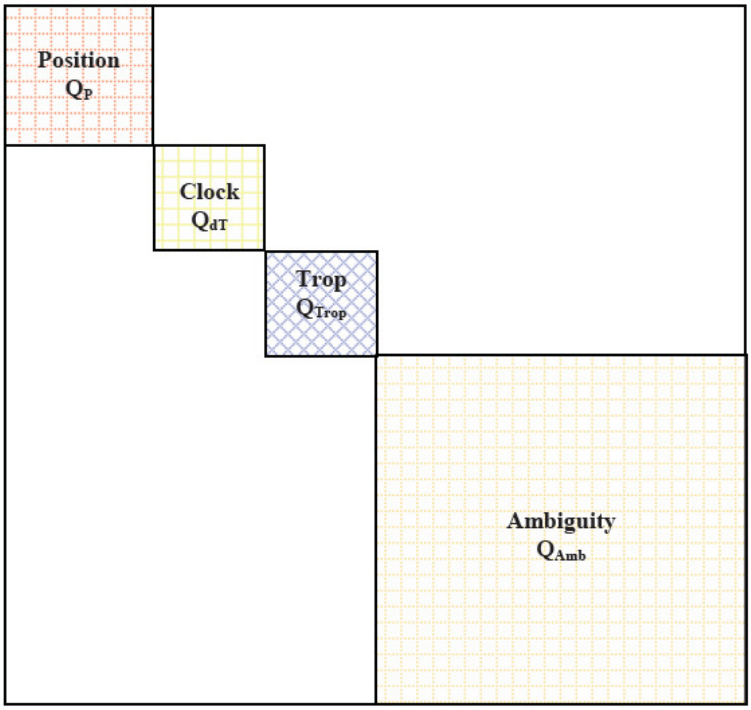


**Figure 4.1 Noise matrix structure (Abdel-Salam, 2005)**

The sub-block of the position errors can be described as Equation (4.3) (Abdel-Salam, 2005).

$$Q_P = \begin{bmatrix} \frac{q_{V_N}\Delta t^3}{3(R_m+h)^2} & 0 & 0 & 0 & \frac{q_{V_N}\Delta t^2}{2(R_m+h)} & 0 \\ 0 & \frac{q_{V_E}\Delta t^3}{3(R_n+h)^2} & 0 & \frac{q_{V_E}\Delta t^2}{2(R_n+h)} & 0 & 0 \\ 0 & 0 & \frac{q_{V_U}\Delta t^3}{3} & 0 & 0 & \frac{q_{V_U}\Delta t^2}{2} \\ 0 & \frac{q_{V_E}\Delta t^2}{2(R_n+h)} & 0 & q_{V_E}\Delta t & 0 & 0 \\ \frac{q_{V_N}\Delta t^2}{2(R_m+h)} & 0 & 0 & 0 & q_{V_N}\Delta t & 0 \\ 0 & 0 & \frac{q_{V_U}\Delta t^2}{2} & 0 & 0 & q_{V_U}\Delta t \end{bmatrix} \quad (4.3)$$

where $q_{V_E}, q_{V_N}, q_{V_U}$ are the spectral density of the velocity errors in the east, north and up directions, respectively.

Similar to the position error block, the noise matrix for the receiver clock error block can be formulated using a random walk as given in Equation (4.4) (Abdel-Salam, 2005).

$$Q_{dT} = \begin{bmatrix} \frac{1}{3} q_{V_{dt}} \Delta t^3 + q_{V_{dt}} \Delta t & \frac{1}{2} q_{V_{dt}} \Delta t^2 \\ \frac{1}{2} q_{V_{dt}} \Delta t^2 & q_{V_{dt}} \Delta t \end{bmatrix} \tag{4.4}$$

where $q_{V_{dt}}$ is the spectral density of the receiver clock error drift.

The nature of the troposphere allows for modeling its wet component as a random walk process. The noise matrix is illustrated in Equation (4.5) (Abdel-Salam, 2005).

$$Q_{Trop} = \lfloor q_{trop} \Delta t \rfloor \tag{4.5}$$

where $q_{trop}$ is the spectral density of the wet component of tropospheric delay.

As discussed before that the ambiguities are modeled as random constant processes, therefore the noise matrix is a nil matrix.

### *4.1.3 Measurement Model*

The raw GPS measurement contains the inter-frequency bias and the hardware delay that must be taken into account in PPP GPS. The inter-frequency bias is a delay between L1 and L2 signals (Abdel-Salam, 2005) and the hardware delay is caused by satellite and receiver hardware components such as the signal processing (Ray and Senior, 2005; Raquet, 2001). The inter-frequency bias is of no concern since it is cancelled out in the ionosphere-free combination, which is employed in the traditional model to eliminate the first order ionospheric delay. The hardware delay would be absorbed by the receiver clock, which would be estimated along with other parameters.

For the carrier phase measurements, the non-zero initial phase will not be cancelled out in the ionosphere-free combination but will be merged with the ambiguities, which will be estimated as float values.

The traditional model, which includes the ionosphere-free pseudorange, carrier phase and Doppler measurements, is related to the user position and velocity through Equation (4.6), (4.7) and (4.8), respectively.

$$P_{IF}^{i} = \sqrt{(x_s^i - x_u)^2 + (y_s^i - y_u)^2 + (z_s^i - z_u)^2} + cdT + M_{wet} \cdot d_{wet} \tag{4.6}$$

$$\Phi_{IF}^{i} = \sqrt{(x_s^i - x_u)^2 + (y_s^i - y_u)^2 + (z_s^i - z_u)^2} + cdT + M_{wet} \cdot d_{wet} + N_{IF,i} \cdot \lambda_{IF} \tag{4.7}$$

$$\dot{\Phi}_{IF}^{i} = \frac{(x_s^i - x_u)(v_{s,x}^i - v_{u,x}) + (y_s^i - y_u)(v_{s,y}^i - v_{u,y}) + (z_s^i - z_u)(v_{s,z}^i - v_{u,z})}{\rho^i} + cd_{dT} \tag{4.8}$$

where s and u represent the GPS satellites and the user, respectively, i represents i$^{th}$ satellite, $x, y, z$ represent the x coordinate, y coordinate and z coordinate, respectively, $v_x, v_y, v_z$ represents the velocity in x axis, y axis and z axis, respectively, and $M_{wet}$ is the mapping function for the zenith wet component of the tropospheric delay.

Obviously the three equations are non-linear, which need to be linearized when they are used in the Kalman filter. More details about the linearization can be found in Kaplan (1996) and Parkinson and Spilker (1996). After the linearization procedure, the design matrix for the pseudorange, carrier phase and Doppler measurements in the ECEF-frame can be described by Equation (4.9), (4.10) and (4.11), respectively.

$$H(P)=\begin{bmatrix} \frac{\partial P^i}{\partial x_u} & \frac{\partial P^i}{\partial y_u} & \frac{\partial P^i}{\partial z_u} & 0 & 0 & 0 & 1 & 0 & m(e)^i & \cdots 0 \\ \vdots & \vdots & \vdots & \vdots & \vdots & \vdots & \vdots & \vdots & \vdots & \vdots \\ \frac{\partial P^n}{\partial x_u} & \frac{\partial P^n}{\partial y_u} & \frac{\partial P^n}{\partial z_u} & 0 & 0 & 0 & 1 & 0 & m(e)^n & \cdots 0 \end{bmatrix} \tag{4.9}$$

$$H(\Phi)=\begin{bmatrix} \frac{\partial \Phi^i}{\partial x_u} & \frac{\partial \Phi^i}{\partial y_u} & \frac{\partial \Phi^i}{\partial z_u} & 0 & 0 & 0 & 1 & 0 & m(e)^i & \lambda_{IF} \cdots 0 \\ \vdots & \vdots & \vdots & \vdots & \vdots & \vdots & \vdots & \vdots & \vdots & \vdots \\ \frac{\partial \Phi^n}{\partial x_u} & \frac{\partial \Phi^n}{\partial y_u} & \frac{\partial \Phi^n}{\partial z_u} & 0 & 0 & 0 & 1 & 0 & m(e)^n & 0 \cdots \lambda_{IF} \end{bmatrix} \tag{4.10}$$

$$H(\dot{\Phi})=\begin{bmatrix} \frac{\partial \dot{\Phi}^i}{\partial x_u} & \frac{\partial \dot{\Phi}^i}{\partial y_u} & \frac{\partial \dot{\Phi}^i}{\partial z_u} & \frac{\partial \dot{\Phi}^i}{\partial v_x} & \frac{\partial \dot{\Phi}^i}{\partial v_y} & \frac{\partial \dot{\Phi}^i}{\partial v_z} & 0 & 1 & 0 & \cdots 0 \\ \vdots & \vdots & \vdots & \vdots & \vdots & \vdots & \vdots & \vdots & \vdots & \vdots \\ \frac{\partial \dot{\Phi}^n}{\partial x_u} & \frac{\partial \dot{\Phi}^n}{\partial y_u} & \frac{\partial \dot{\Phi}^n}{\partial z_u} & \frac{\partial \dot{\Phi}^n}{\partial v_x} & \frac{\partial \dot{\Phi}^n}{\partial v_y} & \frac{\partial \dot{\Phi}^n}{\partial v_z} & 0 & 1 & 0 & \cdots 0 \end{bmatrix} \tag{4.11}$$

where n is the number of satellites in view, $\frac{\partial}{\partial x}, \frac{\partial}{\partial y}, \frac{\partial}{\partial z}$ are the partial derivatives with respect to the position error vector; $\frac{\partial}{\partial v_x}, \frac{\partial}{\partial v_y}, \frac{\partial}{\partial v_z}$ are the partial derivatives with respect to the velocity error vector.

Since the design matrix given in Equation (4.9) to Equation (4.11) is built in the ECEF-frame, the transformation matrix from ECEF-frame to the local-level frame is needed to transform the design matrix to the local-level frame.

The code, carrier phase and Doppler observations are all used in PPP GPS. These observations have different accuracies; therefore, the weight of each observation should be chosen properly (Abdel-Salam, 2005). It is well known that the precision of the observation is related to the satellite's elevation. The SIN function is used in this study to model the relationship between the measurement precision and elevation angle as described in Equation (4.12). The reason for using this function is attributed to the similarity of the Cosecant function and behavior of tropospheric and ionospheric delay changes with respect to the satellite elevation (Vermeer, 1997; Collins and Langely, 1999; Abdel-Salam, 2005).

$$M(E) = \frac{1}{\sin(E)} \tag{4.12}$$

where E is the elevation angle

### 4.2 Tightly Coupled PPP GPS/MEMS IMU Integrated System

As discussed in Chapter 2, the INS mechanization error accumulates over time, thus, the INS must be periodically corrected by external source. This section introduces the tightly coupled integrated PPP GPS/MEMS IMU system which uses the updates from PPP GPS to mitigate the INS error accumulation in tightly coupled mode.

Figure 4.2 illustrates the integration strategy of the tightly coupled integrated PPP GPS/MEMS IMU system. As shown in the figure, a single integration filter is used to fuse the GPS and INS information. Given the GPS satellites ephemeris, the outputs of position and velocity from the INS mechanization are used to predict the pseudorange, carrier phase and Doppler measurements. The error corrector is used to correct the errors in the raw GPS measurements, such as satellite orbit and clock error, ionospheric delay, with more details in Chapter 2. Later, the corrected pseudorange, carrier phase and Doppler measurements from PPP GPS are differenced with the INS-predicted measurements. Then the integration filter directly processes those residuals to estimate the INS error estimates. Finally, the obtained INS error estimates are feed back to the INS mechanization using the closed loop approach. The outputs of the INS mechanization could also be applied in the error corrector of PPP GPS to help quality control of the integrated system, such as cycle slip detection and identification.

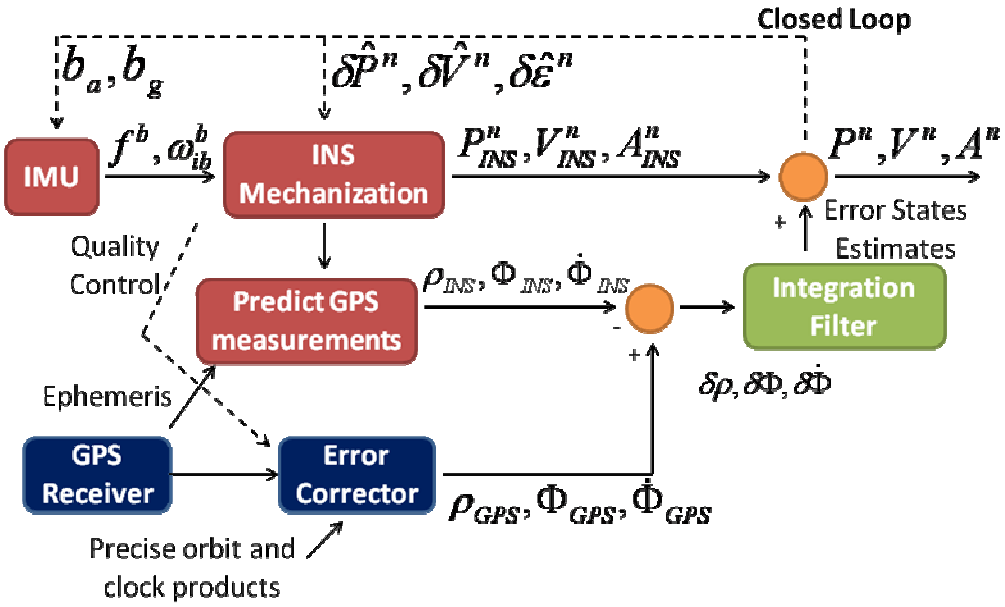


**Figure 4.2 Tightly coupled integrated PPP GPS/MEMS IMU system**

The estimated error states such as position error, velocity error can be directly applied to the INS-derived position and velocity solutions. The attitude states can be corrected by using Equation (4.13). The sensor bias and scale factors can be applied to the raw INS measurements as shown in Equation (2.11) and (2.12).

$$R_b^{l,+} = (I - \Omega_\varepsilon) R_b^{l,-} \tag{4.13}$$

where $\Omega_\varepsilon$ represent the skew-symmetric matrix of the attitude error states obtained from the integration filter, $R_b^{l,-}$ and $R_b^{l,+}$ represent the transformation matrix before and after applying the attitude corrections, respectively.

### *4.2.1 System States*

A basic INS error state vector consists of nine navigation error states, which are 3 position error states, 3 velocity error states and 3 attitude error states. However due to the sensor errors of accelerometers and gyroscopes, the system state vector needs to be augmented by the sensor error states. The number of augmented sensor error states depends on the sensor error characteristics, which primarily determined by the grade of IMU (Shin, 2005; Godha, 2006). For the high-end IMU, such as navigation grade IMU, or tactical grade IMU, the sensor errors of turn on biases and scale factors can be neglected. However, the low cost MEMS IMU, such as Crista IMU used in this study, normally features a turn-on bias of about several thousand degrees per hour and exhibits in-run bias drift of more than 1000 degrees per hour in gyros (Godha, 2006). Since it is not practical to calibrate these errors each time when the sensor is turned on, a solution is to estimate them as additional states in the Kalman filter.

By considering the position errors, velocity errors, attitude errors, and the additional sensor bias drifts, turn on biases and scale factor errors for the low cost MEMS IMU, a 27-INS error state vector is formed as Equation (4.14).

$$x_{INS} = [\delta r^l, \delta v^l, \delta \varepsilon^l, \delta b_a, \delta b_g, b_{a,tob}, b_{g,tob}, S_a, S_g] \tag{4.14}$$

where a and g represent the accelerometer and gyroscope, respectively, the symbol $\delta \varepsilon^l = [\delta\theta \quad \delta\phi \quad \delta\psi]$ is the attitude error state vector, $\delta\theta, \delta\phi, \delta\psi$ represent the

pitch, roll and azimuth error states, respectively; $S_i$ is the scale factor error, $b_{i,tob}$ is the turn on bias, and $\delta b_i$ is the bias drift

Since there is only one filter in the tightly coupled integrated system to process both GPS and INS information, the filter must account for not only the INS error states but also the PPP GPS states, such as the receiver clock offset, wet component of the tropospheric delay and the ambiguity terms. The full integration filter system state vector can be described by Equation (4.15).

$$x = [x_{INS}, dT, d_{dT}, d_{trop}, N_{IF,1}, N_{IF,2} \cdots N_{IF,n}] \tag{4.15}$$

### *4.2.2 System Model*

The INS error model is derived from the perturbations of the INS mechanization equations. It can be described by a series of differential equations as follows. The first derivative of the position errors is related to the position errors and velocity errors, which can be described as Equation (4.16) (El-Sheimy, 2007; Jekeli, 2001; Shin, 2001).

$$\dot{\delta r}^l = F_{rr}\delta r^l + F_{rv}\delta v^l \tag{4.16}$$

where $F_{rr} = \begin{bmatrix} 0 & 0 & -\dfrac{\dot{\varphi}}{R_m + h} \\ \dot{\lambda}\tan\varphi & 0 & -\dfrac{\dot{\lambda}}{R_n + h} \\ 0 & 0 & 0 \end{bmatrix}$ and $F_{rv} = \begin{bmatrix} 0 & \dfrac{1}{R_m + h} & 0 \\ \dfrac{1}{(R_n + h)\cos\varphi} & 0 & 0 \\ 0 & 0 & -1 \end{bmatrix}$.

The first derivative of the velocity errors is related to the position errors, the velocity errors, the attitude errors as well as the accelerometer sensor error, which can be described as Equation (4.17) (El-Sheimy, 2007; Jekeli, 2001; Shin, 2001).

$$\delta\dot{v}^l = F_{vr}\delta r^l + F_{vv}\delta v^l + F_{v\varepsilon}\delta\varepsilon^l + R_b^l \delta f^b \tag{4.17}$$

where $F_{vr} = \begin{bmatrix} 2\omega_e(v^U \sin\varphi + v^N \cos\varphi) + v^N\dot{\lambda}/\cos\varphi & 0 & 0 \\ -2\omega_e v^E \cos\varphi - v^E\dot{\lambda}/\cos\varphi & 0 & 0 \\ -2\omega_e v^E \sin\varphi & 0 & \dfrac{2\gamma}{R} \end{bmatrix}$,

$F_{vv} = \begin{bmatrix} \dfrac{-v^U + v^N\tan\varphi}{N + h} & (2\omega_e + \dot{\lambda})\sin\varphi & -(2\omega_e + \dot{\lambda})\cos\varphi \\ -(2\omega_e + \dot{\lambda})\sin\varphi & \dfrac{-v^U}{R_m + h} & -\dot{\varphi} \\ (2\omega_e + \dot{\lambda})\cos\varphi & 2\dot{\varphi} & 0 \end{bmatrix}$,

$F_{v\varepsilon} = \begin{bmatrix} 0 & f^U & -f^N \\ -f^U & 0 & f^E \\ f^N & -f^E & 0 \end{bmatrix}$, and $f^E, f^N, f^U$ are the specific force in the l-frame;

$\dot{\varphi}$ and $\dot{\lambda}$ are the latitude and longitude rate, respectively, $\gamma$ is the normal gravity that varies with the altitude, $\delta f^b$ is the accelerometer sensor error, and $R = \sqrt{R_m R_n}$.

The first derivative of the attitude errors is related to the position errors, the velocity errors, the attitude errors and the gyro sensor error, which can be described by Equation (4.18) (El-Sheimy, 2007; Jekeli, 2001; Shin, 2001).

$$\delta\dot{\varepsilon}^l = F_{\varepsilon r}\delta r^l + F_{\varepsilon v}\delta v^l + F_{\varepsilon\varepsilon}\delta\varepsilon^l + R_b^l\delta\omega_{ib}^b \tag{4.18}$$

where $F_{\varepsilon r} = \begin{bmatrix} 0 & 0 & \frac{\dot{\varphi}}{R_m + h} \\ -\omega_e \sin\varphi & 0 & -\frac{\dot{\lambda}\cos\varphi}{R_n + h} \\ \omega_e \cos\varphi + \dot{\lambda}/\cos\varphi & 0 & -\frac{\dot{\lambda}\sin\varphi}{R_n + h} \end{bmatrix}$, $F_{\varepsilon v} = \begin{bmatrix} 0 & -\frac{1}{R_m + h} & 0 \\ \frac{1}{R_n + h} & 0 & 0 \\ \frac{\tan\varphi}{R_n + h} & 0 & 0 \end{bmatrix}$,

$F_{\varepsilon\varepsilon} = \begin{bmatrix} 0 & (\omega_e + \dot{\lambda})\sin\varphi & -(\omega_e + \dot{\lambda})\cos\varphi \\ -(\omega_e + \dot{\lambda})\sin\varphi & 0 & -\dot{\varphi} \\ (\omega_e + \dot{\lambda})\cos\varphi & \dot{\varphi} & 0 \end{bmatrix}$, $\omega_e$ represents the earth rotation rate and $\delta\omega_{ib}^b$ is the gyro sensor error.

The inertial sensor bias-drift is normally modeled as a first order Gauss-Markov process, which can be described as Equation (4.19).

$$\begin{aligned} \dot{\delta b}_a &= -\frac{1}{\tau_a}\delta b_a + \eta_{ba} \\ \dot{\delta b}_g &= -\frac{1}{\tau_g}\delta b_g + \eta_{bg} \end{aligned} \tag{4.19}$$

where $\tau_i$ is the correlation time and $\eta_{bi}$ is the Gauss-Markov process driving noise with spectral density $q_{bi}$.

Normally the Gauss-Markov model parameters, such as correlation time $\tau_i$ and variance $\sigma_i$, are obtained by calculating the auto-correlation function of the raw INS data under static conditions (Gelb, 1974; Nassar, 2003).

The inertial sensor turn on bias remains constant after the sensor is turned on; therefore, it is modeled as a random constant process, which can be described as Equation (4.20).

$$\begin{aligned} \dot{b}_{a,tob} &= 0 \\ \dot{b}_{g,tob} &= 0 \end{aligned} \tag{4.20}$$

The inertial sensor scale factor changes slowly with time, and thus can be modeled as a first order Gauss-Markov process with a large correlation time (Godha, 2006), which can be described as Equation (4.21)

$$\dot{S}_a = -\frac{1}{\tau_{sa}} S_a + \eta_{sa}$$
$$\dot{S}_g = -\frac{1}{\tau_{sg}} S_g + \eta_{sg} \tag{4.21}$$

where $\tau_{si}$ represents the correlation time and the $\eta_{si}$ is the Gauss-Markov process driving noise.

The PPP states remain the same as described in the PPP filter, which can be described by Equation (4.22)

$$\begin{bmatrix} \dot{dT} \\ \dot{d}_{dT} \\ \dot{d}_{wet} \\ \dot{N}_{IF,i} \end{bmatrix} = \begin{bmatrix} 0 & 1 & 0 & 0 \\ 0 & 0 & 0 & 0 \\ 0 & 0 & 0 & 0 \\ 0 & 0 & 0 & 0 \end{bmatrix} \begin{bmatrix} dT \\ d_{dT} \\ d_{wet} \\ N_{IF,i} \end{bmatrix} + \begin{bmatrix} 0 \\ q_{v_{dt}} \\ q_{trop} \\ 0 \end{bmatrix} \tag{4.22}$$

### *4.2.3 Measurement Model*

The integration filter processes the residuals between the corrected GPS measurements and the corresponding INS-predicted measurements to estimate the error states. The design matrix for pseudorange, carrier phase and Doppler measurements in an ECEF-frame are given in Equation (4.23), (4.24) and (4.25), respectively. The linearization point is obtained from the INS mechanization. A transformation matrix from the ECEF-frame to the local-level frame is needed to transform the design matrix to the local level-frame. The misclosure vector can be calculated as Equation (4.26).

$$H(P)=\begin{bmatrix} \frac{\partial P^i}{\partial x_u} & \frac{\partial P^i}{\partial y_u} & \frac{\partial P^i}{\partial z_u} & 0 & 0 & 0 & 0_{1\times 21} & 1 & 0 & m(e)^i & \cdots 0 \\ \vdots & \vdots & \vdots & \vdots & \vdots & \vdots & \vdots & \vdots & \vdots & \vdots & \vdots \\ \frac{\partial P^n}{\partial x_u} & \frac{\partial P^n}{\partial y_u} & \frac{\partial P^n}{\partial z_u} & 0 & 0 & 0 & 0_{1\times 21} & 1 & 0 & m(e)^n & \cdots 0 \end{bmatrix} \tag{4.23}$$

$$H(\Phi)=\begin{bmatrix} \frac{\partial \Phi^i}{\partial x_u} & \frac{\partial \Phi^i}{\partial y_u} & \frac{\partial \Phi^i}{\partial z_u} & 0 & 0 & 0 & 0_{1\times 21} & 1 & 0 & m(e)^i & \lambda_{IF}\cdots 0 \\ \vdots & \vdots & \vdots & \vdots & \vdots & \vdots & \vdots & \vdots & \vdots & \vdots & \vdots \\ \frac{\partial \Phi^n}{\partial x_u} & \frac{\partial \Phi^n}{\partial y_u} & \frac{\partial \Phi^n}{\partial z_u} & 0 & 0 & 0 & 0_{1\times 21} & 1 & 0 & m(e)^n & 0\cdots \lambda_{IF} \end{bmatrix} \tag{4.24}$$

$$H(\dot{\Phi})=\begin{bmatrix} \frac{\partial \dot{\Phi}^i}{\partial x_u} & \frac{\partial \dot{\Phi}^i}{\partial y_u} & \frac{\partial \dot{\Phi}^i}{\partial z_u} & \frac{\partial \dot{\Phi}^i}{\partial v_x} & \frac{\partial \dot{\Phi}^i}{\partial v_y} & \frac{\partial \dot{\Phi}^i}{\partial v_z} & 0_{1\times 21} & 0 & 1 & 0 & \cdots 0 \\ \vdots & \vdots & \vdots & \vdots & \vdots & \vdots & \vdots & \vdots & \vdots & \vdots & \vdots \\ \frac{\partial \dot{\Phi}^n}{\partial x_u} & \frac{\partial \dot{\Phi}^n}{\partial y_u} & \frac{\partial \dot{\Phi}^n}{\partial z_u} & \frac{\partial \dot{\Phi}^n}{\partial v_x} & \frac{\partial \dot{\Phi}^n}{\partial v_y} & \frac{\partial \dot{\Phi}^n}{\partial v_z} & 0_{1\times 21} & 0 & 1 & 0 & \cdots 0 \end{bmatrix} \tag{4.25}$$

$$Z=\begin{bmatrix} P_j^{GPS}-P_j^{INS} \\ \Phi_j^{GPS}-\Phi_j^{INS} \\ \dot{\Phi}_j^{GPS}-\dot{\Phi}_j^{INS} \\ \vdots \end{bmatrix} \tag{4.26}$$

where $P_j^{GPS},\Phi_j^{GPS},\dot{\Phi}_j^{GPS}$ are the PPP-corrected ionosphere-free pseudorange, carrier phase and Doppler measurements, respectively, $P_j^{INS},\Phi_j^{INS},\dot{\Phi}_j^{INS}$ are the INS-predicted ionosphere-free pseudorange, carrier phase and Doppler measurements, respectively.

### 4.3 Loosely Coupled PPP GPS/MEMS IMU Integrated System

This section describes the loosely coupled integrated PPP GPS/MEMS IMU system, in which the PPP GPS and inertial processing are carried out in two separate, but interacting filters, namely the PPP filter and the integration filter.

Figure 4.3 shows the scheme of the loosely coupled integrated system. As illustrated in the figure, the integrated system contains three components, namely the INS component, the PPP component and the integration filter component. The raw GPS measurements are firstly corrected by the error corrector in the PPP component to mitigate the measurement errors; then the PPP filter processes the corrected GPS measurements to estimate the position and velocity solutions. Meanwhile the INS raw measurements are processed in the INS component to derive the position and velocity solutions. The integration filter then uses the difference between the PPP-derived position and velocity solutions and the INS mechanization-derived solutions as measurements to estimate the error states. The closed loop approach is used to feedback the estimated error states to the INS component to compensate the INS errors. Similar to the tightly coupled integrated system, the outputs of the INS mechanization could also be applied in PPP error corrector to help the quality control.

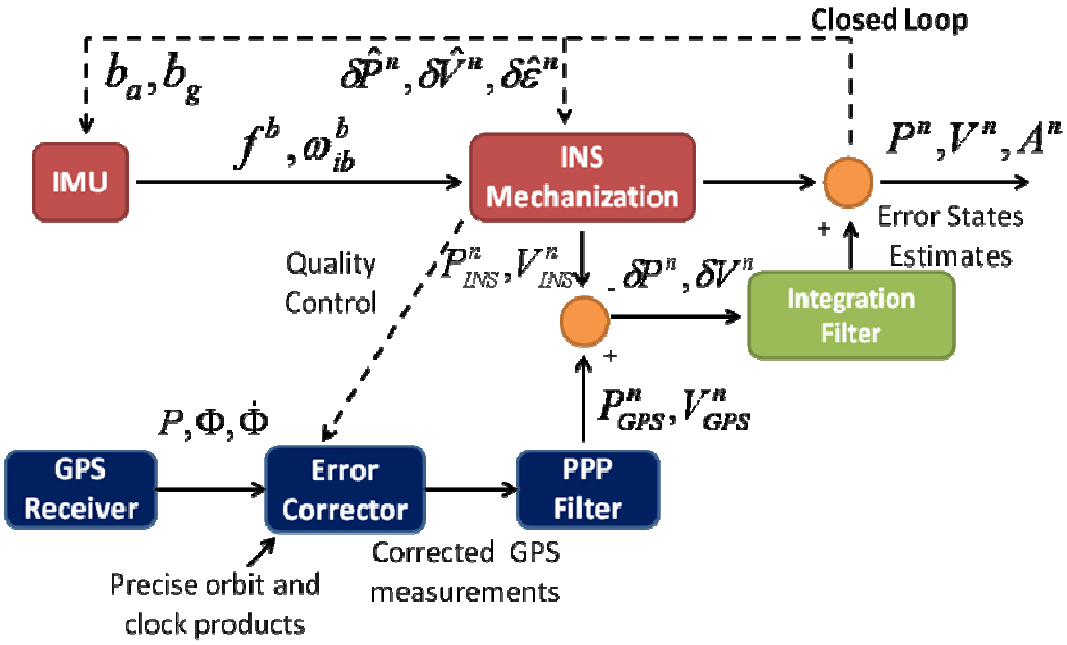


**Figure 4.3 Loosely coupled integrated PPP GPS/MEMS IMU system**

Since the PPP GPS and inertial processing are carried out in two separate filters, the integration filter only deals with the INS error states, which contain 27 error states in total and have been given in Equation (4.14).

The system model of the integration filter is the INS error model only, which has been given through Equation (4.16) to Equation (4.21).

The integration filter uses the residuals between the estimates of PPP-derived position and velocity, and the estimates of INS mechanization-derived position and velocity as measurements to compute the error estimates. Therefore, the measurement design matrix and the misclosure vector of the integration filter can be described as Equation (4.27) and Equation (4.28).

$$H = \begin{bmatrix} I_{3\times3} & 0_{3\times3} & 0_{3\times(n-6)} \\ 0_{3\times3} & I_{3\times3} & 0_{3\times(n-6)} \end{bmatrix} \tag{4.27}$$

$$Z = \begin{bmatrix} r_{GPS}^{l} - r_{INS}^{l} \\ v_{GPS}^{l} - v_{INS}^{l} \end{bmatrix}_{6\times1} \tag{4.28}$$

The measurement noise matrix of the integration filter is generated by transferring the full position and velocity variance covariance matrix from the PPP filter to ensure that the correlation between the PPP-derived position and velocity is properly accounted.

### 4.4 2D Velocity Constraints

It is found that the non-holonomic constraints can improve the attitude accuracies of the integrated GPS/INS system and mitigate the INS error accumulation during the GPS outages (Dissanayake et al., 2001; Shin, 2005; Wang and Gao, 2006). The constraints used in this thesis are the 2D velocity constraints. It is worthy to mention that the 2D velocity constraints are only suitable for the application of ground vehicles.

The 2D velocity constraints are derived based on two assumptions. The first assumption is that the vehicle does not slip, which is a close representation for a vehicle travelling in a constant direction. The second assumption is that the vehicle stays on the ground. If both of the assumptions are true, then the velocity in the direction perpendicular to the movement of the vehicle can be regarded as zero (Shin, 2005; Li, 2009). The constraints can be illustrated in Figure 4.4.

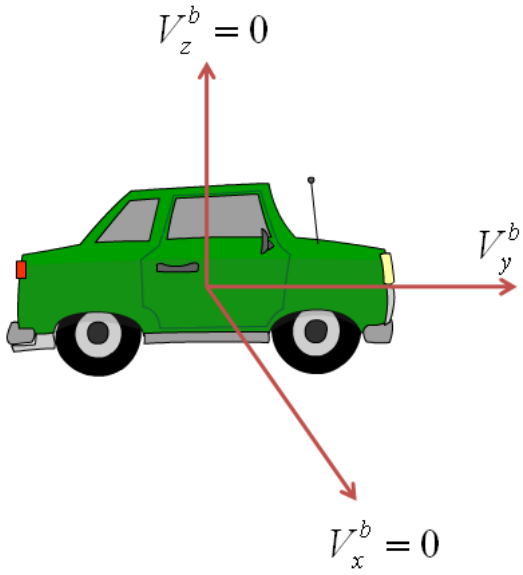


**Figure 4.4 2D velocity constraints**

If the body frame is defined as the Y axis point to the forward direction, the Z axis point to the up direction, and the X axis point to the right direction, the 2D velocity constraints can be mathematically written as Equation (4.29)

$$\begin{aligned} v_x^b &\approx 0 \\ v_z^b &\approx 0 \end{aligned} \tag{4.29}$$

The 2D velocity constraints are applied to the integrated system as illustrated in Figure 4.5. The INS mechanization-derived velocities along X axis (lateral direction) and Z axis (vertical direction) are differenced with the corresponding velocities obtained from the 2D velocity constraints. Then the integration filter processes the velocity residuals to

estimate the error states. The obtained estimates of the error states are then feedback to the INS component to compensate the INS errors.

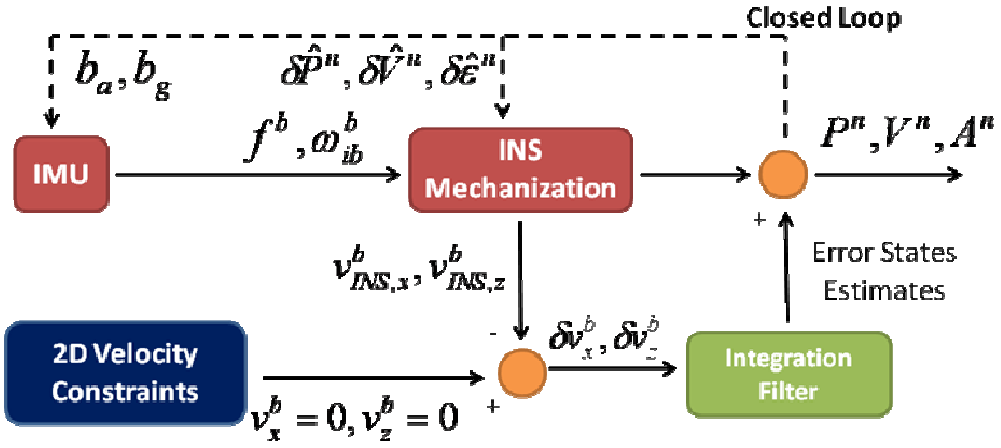


**Figure 4.5 Integration scheme of using 2D velocity constraints**

The 2D velocity constraints can be used as additional observations in the integration filter. The measurement model can be obtained by a perturbation analysis of the body frame velocity as illustrated in Equation (4.30) and (4.31).

$$\hat{v}_{INS}^b = v^b + \delta v^b = [(I + E^l)R_b^l]^T (v^l + \delta v^l) \tag{4.30}$$

$$\delta v^b = R_l^b \delta v^l - R_l^b E^l v^l = R_l^b \delta v^l + V^b R_l^b \varepsilon^l \tag{4.31}$$

where $E^l$ is the skew-symmetric matrix of the attitude error states, and $V^b$ is the skew-symmetric matrix of the velocity expressed in the body frame.

As indicated in Equation (4.31), the velocity error in the body frame is correlated to the attitude estimates. As a result, improvements should be observed on the attitude estimates in theory when the 2D velocity constraints are used. Based on the Equation (4.31), the design matrix and misclosure vector can be written as Equation (4.32) and (4.33), respectively.

$$H_{2D} = \begin{bmatrix} 0_{1\times3} & R_{11} & R_{12} & R_{13} & v_y^b R_{31} - v_z^b R_{21} & v_y^b R_{32} - v_z^b R_{22} & v_y^b R_{33} - v_z^b R_{23} & 0_{1\times(n-9)} \\ 0_{1\times3} & R_{31} & R_{32} & R_{33} & v_x^b R_{21} - v_y^b R_{11} & v_x^b R_{22} - v_y^b R_{12} & v_x^b R_{23} - v_y^b R_{13} & 0_{1\times(n-9)} \end{bmatrix} \quad (4.32)$$

$$Z = \begin{bmatrix} 0 - v_x^b \\ 0 - v_z^b \end{bmatrix} \quad (4.33)$$

where $R_{ij}$ represents the element at i$^{th}$ row and the j$^{th}$ column of a transformation matrix from the body frame to the local-level frame.

The measurement noise of the 2D velocity constraints is calculated based a projection of the forward velocity on the lateral and vertical directions due to the misalignment angles as shown in Equation (4.34).

$$\begin{aligned} v_x^b &= v_y^b \sin\alpha \\ v_z^b &= v_y^b \sin\beta \end{aligned} \quad (4.34)$$

where $\alpha, \beta$ are the misalignment angles.

The typical forward velocity of a land vehicle is 18~20 m/s in most cases, and if the misalignment angle is 2~3 degrees, then the projected velocity on the lateral and vertical directions is around 1 m/s (Shin, 2001; Li, 2009).

### 4.5 Inertial Aided Cycle Slip Detection and Identification

The carrier phase measurements are the primary observables in the PPP GPS. Before they can be used as the most accurate ranging information, their integer ambiguities must be resolved. Unfortunately, high dynamics, signal obstruction and low satellite elevation may cause so called cycle slips, which would cause a jump on the integer ambiguities and deteriorate the obtainable accuracy if the cycle slips remain undetected.

In this thesis, an algorithm of inertial aided cycle slip detection and identification is developed to help the quality control in PPP GPS. The basic idea of this algorithm is to differentiate the double differenced (differencing between two satellites and differencing between two consecutive epochs) GPS carrier phase observations with the calculated double differenced INS-derived geometric ranges to get a decision variable. Then this decision variable is used to detect and identify the possible cycle slips. The proposed algorithm is implemented in 3 steps, namely, widelane (WL) phase based cycle slip detection and identification, extra-widelane (EWL) phase based cycle slip detection and identification, and cycle slip identification on L1 and L2 frequencies.

Step One: Widelane Phase Based Cycle Slip Detection and Identification

The first step contains two tasks, which are decision variable calculation and cycle slip detection and identification. Figure 4.6 illustrates the scheme of the decision variable calculation. As illustrated in the figure, the double differenced GPS WL phase observations are firstly generated. Given the satellites' positions, the double differenced INS-derived geometric ranges are computed based on the INS-predicted user's positions. Then the decision variables are calculated by differencing the double differenced GPS WL phase observations and the double differenced INS-derived geometric ranges. It is worthy to mention that the double differenced algorithm used here means the differencing between two satellites and the differencing between two consecutive epochs; it is not the same as the traditional double difference algorithm in DGPS. The reason of using WL phase combination is that it has a wavelength of 86 cm, which is much longer than the wavelength on L1 and L2 frequencies. As a result the robustness and reliability of the testing procedure are improved.

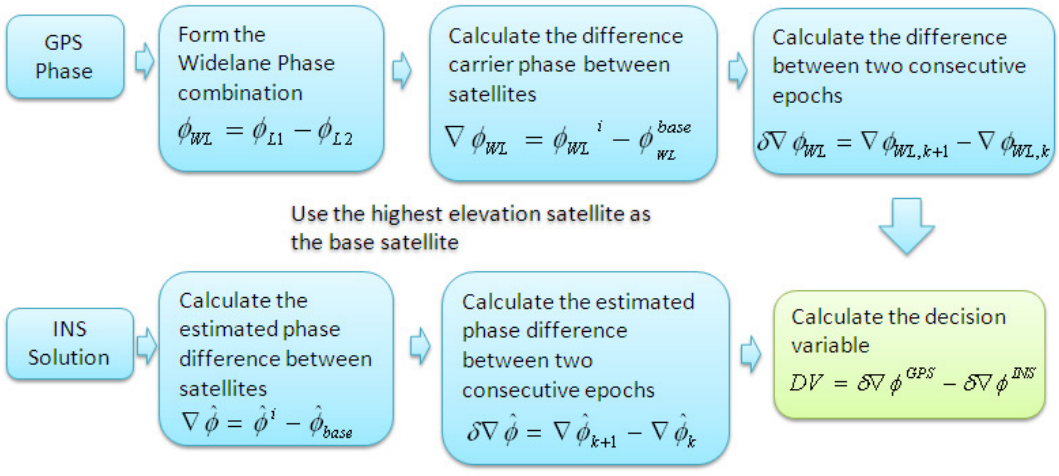


**Figure 4.6 Scheme of WL-based decision variable calculation**

The procedure of the calculation of the WL based decision variable can also be described by the following equations. The differencing of the WL phase measurements between two satellites eliminates the receiver clock error, which can be described in Equation (4.35).

$$\nabla\Phi_{WL} = \nabla\rho + \lambda_{WL}\nabla N_{WL} - \nabla d_{ion,WL} + \nabla d_{trop} + \nabla\varepsilon(\Phi_{WL}) \tag{4.35}$$

where WL represents the widelane phase linear combination, the symbol $\nabla$ represents the differencing between satellites, $\lambda_{WL}$ represents the wavelength of the widelane phase, $N_{WL}$ represents the widelane ambiguity, $d_{ion,WL}$ represents the ionospheric delay in the widelane phase combination, and $\varepsilon$ represents the measurement noise.

The differencing between two consecutive epochs eliminates the ambiguity term if the carrier phase is free of cycle slips over the two consecutive epochs. It can be mathematically described by Equation (4.36).

$$\delta\nabla\Phi_{WL} = \delta\nabla\rho - \delta\nabla d_{ion,WL} + \delta\nabla d_{trop} + \delta\nabla\varepsilon(\Phi_{WL}) \tag{4.36}$$

where $\delta$ represents the differencing between two consecutive epochs, and $\delta\nabla\varepsilon(\Phi_{WL})$ represents the double differenced GPS WL phase error, which primarily includes the phase noise and multipath.

The double differenced INS-derived geometric range can be obtained through the same procedure, which can be described by Equation (4.37).

$$\delta\nabla\Phi_{WL}^{INS} = \delta\nabla\rho + \delta\nabla\varepsilon(\Phi_{WL}^{INS}) \tag{4.37}$$

where $\delta\nabla\varepsilon(\Phi_{WL}^{INS})$ represents the error contained in the calculated double differenced INS-derived geometric range.

The INS-derived geometric range is determined by the INS-predicted user's position and the satellite's position. Since the precise GPS orbit product is able to eliminate the satellite orbit error, the error contained in the INS-derived range highly depends on the INS-predicted position error, which is primarily determined by the sensors errors.

The WL based decision variable is calculated by differencing the double differenced GPS WL phase measurement and the corresponding double differenced INS-derived geometric range. If the GPS carrier phase is free of cycle slips, the decision variable can be described by Equation (4.38).

$$DV = -\delta\nabla d_{ion,WL} + \delta\nabla d_{trop} + \delta\nabla\varepsilon(\Phi_{WL}) - \delta\nabla\varepsilon(\Phi_{WL}^{INS}) \tag{4.38}$$

The double differenced geometric range is eliminated by the differencing procedure. If it is assumed that the ionospheric delay and tropospheric delay do not change much during the two consecutive epochs, then the decision variable can be simplified as described in Equation (4.39).

$$DV = \delta\nabla\varepsilon(\Phi_{WL}) - \delta\nabla\varepsilon(\Phi_{WL}^{INS}) \tag{4.39}$$

As shown in Equation (4.39), the decision variable only contains the double differenced GPS WL phase error and the double differenced INS-derived range error if the carrier phase is free of cycle slips. If we further assume that the GPS WL phase error and INS-derived range error are Gaussian distributed, then the decision variable is a Gaussian random variable with a mean value of zero. Since the noise level of the carrier phase measurement is very low, the standard deviation of the decision variable primarily depends on the error characteristics of the MEMS IMU.

The cycle slip detection and identification scheme is very straightforward, which is shown in Figure 4.7. If the decision variable exceeds a certain threshold, a cycle slip is detected; otherwise no cycle slip is detected. Similarly, if the decision variable falls into an interval determined by an integer number and a certain threshold, such as $\left[m - T_N, m + T_N\right]$, then the slipped cycles are identified as m.

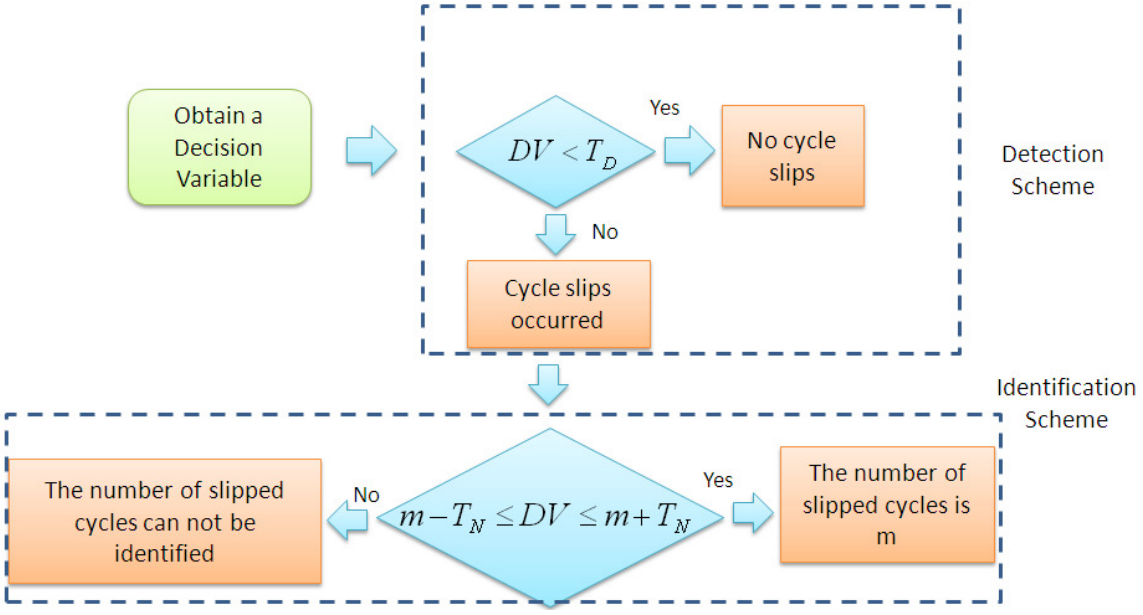


**Figure 4.7 Scheme of cycle slip detection and identification**

The algorithm of cycle slip detection and identification is mathematically derived from the statistical testing. The detection algorithm contains two tasks, namely 1) define hypothesis and 2) form test statistic, which can be described through Equation (4.40) to Equation (4.43).

The null hypothesis means no cycle slip occurred, and the mean value of the decision variable is zero, which is described in Equation (4.40)

$$H_0 : E(DV) = 0 \tag{4.40}$$

The alternative hypothesis means cycle slips are present, and the mean value of the decision variable is not zero, which is described in Equation (4.41).

$$H_a : E(DV) \neq 0 \tag{4.41}$$

If we assume that the decision variable is Gaussian distributed, then the test statistic for null hypothesis follows the Gaussian distribution centered at zero, with variance σ, which can be described by Equation (4.42).

$$H_0 : w = DV \sim N(0, \sigma) \tag{4.42}$$

Similarly the test statistic for the alternative hypothesis also follows the Gaussian distribution but centered at m, with variance σ, which is described as Equation (4.43).

$$H_a : w = DV \sim N(m, \sigma) \tag{4.43}$$

where m is the number of cycle slips.

When the absolute value of the test statistic is less than a certain threshold, the null hypothesis $H_0$ will be accepted, which means no cycle slip occurred; otherwise the alternative hypothesis $H_a$ will be accepted, which means at least one cycle slip is present.

The testing probabilities, such as probabilities of false alarm and missed detection are also derived from the statistical testing. Figure 4.8 shows the probabilities of false alarm and missed detection. False alarm means that the threshold is exceeded though no cycle slip occurred, its probability can be calculated as shown in Equation (4.44) (Altmayer, 2000).

$$P_{FA} = P\left(\left|DV\right| \geq T_D \mid H_0\right) = 2erfc\left(\frac{T_D}{\sigma}\right) \tag{4.44}$$

where the error function $erfc(x) = \frac{2}{\sqrt{\pi}} \int_x^{\infty} e^{-t^2} dt$, and $T_D$ represents the chosen threshold for cycle slip detection.

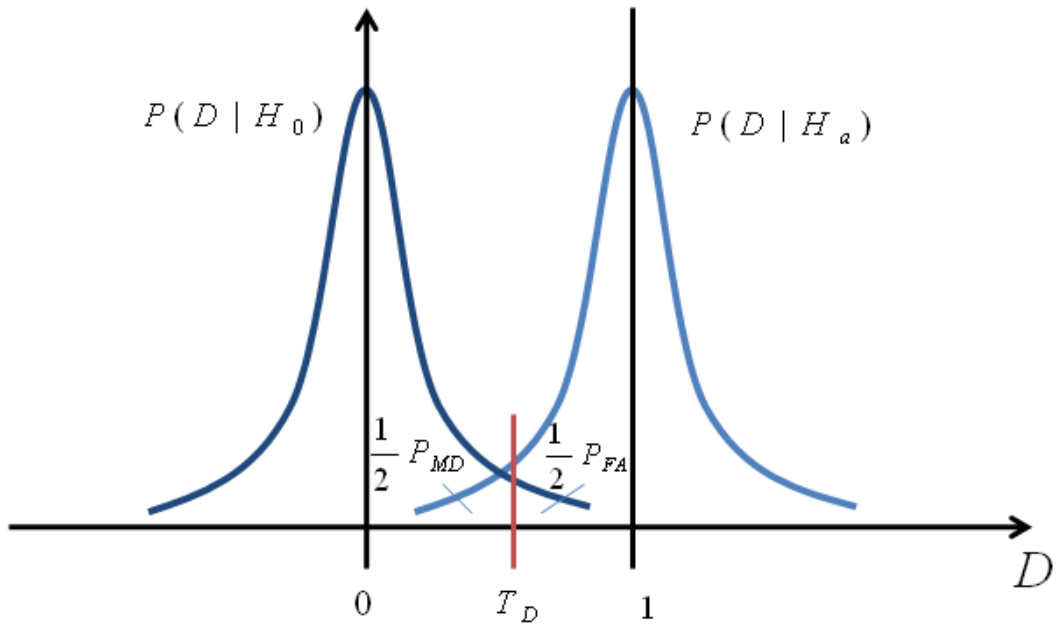


**Figure 4.8 Probability of false alarm and missed detection**

The missed detection means that the threshold is not exceeded though cycle slips are actually present. Its probability can be calculated as described in Equation (4.45) (Altmayer, 2000).

$$P_{MD} = P\left(\left|DV\right| < T_D \mid H_a\right) = erfc\left(\frac{m - T_D}{\sigma}\right) - erfc\left(\frac{m + T_D}{\sigma}\right) \tag{4.45}$$

where m is the slipped cycles in GPS carrier phase measurements.

As illustrated in Figure 4.7, the cycle slip identification is performed only if cycle slips are detected. Similar to the cycle slip detection, the cycle slip identification also includes two tasks, namely 1) define hypothesis and 2) form test statistic. The defined hypothesis is described in Equation (4.46).

$$\begin{aligned} &H_1 : E(DV) = 1 \\ &H_2 : E(DV) = 2 \\ &\vdots \\ &H_m : E(DV) = m \end{aligned} \tag{4.46}$$

where m represents the number of the cycle slips in the GPS carrier phase measurements.

The test statistic for each of the hypothesis follows the Gaussian distribution centered at the number of the slipped cycles with variance σ, which can be described by Equation (4.47).

$$\begin{aligned} &H_1 : w = DV \sim N(1,\sigma) \\ &H_2 : w = DV \sim N(2,\sigma) \\ &\vdots \\ &H_m : w = DV \sim N(m,\sigma) \end{aligned} \tag{4.47}$$

If the test statistic falls into a certain interval that centered at an integer number m then this integer number is said to be the actual number of slipped cycles. The interval can be described by Equation (4.48).

$$I_m = \left[m - T_N, m + T_N\right] \tag{4.48}$$

where $m \in \{\cdots -2,-1,1,2,\cdots\}$, represents the number of cycle slips, and $T_N$ represents the selected threshold for cycle slip identification.

The testing probabilities for the cycle slip identification include the probabilities of right determination and false determination. Right determination means that the test statistic falls into the interval $I_m$ centered at the number m if indeed m is the number of the cycle slips. Its probability can be calculated as shown in Equation (4.49) (Altmayer, 2000).

$$P_{RD} = P(DV \in I_m \mid H_m) = 2erf(\frac{T_N}{\sigma}) - 1 \tag{4.49}$$

where error function $erf(x) = \frac{2}{\sqrt{\pi}} \int_0^x e^{-t^2} dt$, and $T_N$ is the chosen threshold for cycle slip identification.

False determination means that the test statistic lies in the wrong interval $I_k$ leading to a false fixed number of the cycle slips. Its probability can be described in Equation (4.50) (Altmayer, 2000).

$$P_{FD} = P(DV \in I_k \mid H_m)|_{m \neq k} = 2\sum_{i=1}^{\infty} \left( erf(\frac{i + T_N}{\sigma}) - erf(\frac{i - T_N}{\sigma}) \right)|_{i \neq m} \tag{4.50}$$

As it can be seen from Equation (4.44), (4.45), (4.49) and (4.50), the testing probabilities are highly dependent upon the chosen thresholds ($T_N$ and $T_D$) and the standard deviation (σ) of the decision variable. In practice certain critical testing probabilities like $P_{MD}$ and $P_{FD}$ have to be guaranteed and are therefore treated as given values while the thresholds are adjusted according to the estimation of the actual standard deviations (Altmayer, 2000).

Step Two: Extra-Widelane Phase Based Cycle Slip Detection and Identification

The extra-widelane phase based cycle slip detection and identification follows the same testing procedure described in step one. The only difference in step two is that instead of using widelane phase combination, the extra-widelane phase combination is used, which can be generated in the unit of cycle as shown in Equation (4.51).

$$\Phi_{EWL} = 4\Phi_{L1} - 5\Phi_{L2} \tag{4.51}$$

The wavelength of the EWL phase is 183 cm, which is 2 times longer than the wavelength of WL phase.

Step Three: Cycle Slip Identification on L1 and L2 Frequencies

The WL and EWL phases are the linear combinations of the carrier phase observations in L1 and L2 frequencies, so the WL and EWL phase cycle slips are also linear combinations of cycle slips on L1 and L2 frequencies. Based on the identified cycle slips on the WL phase and EWL phase, the cycle slips on L1 and L2 frequencies can be easily determined as shown in Equation (4.52) and Equation (4.53).

$$m_1 = 5m_{WL} - m_{EWL} \tag{4.52}$$

$$m_2 = 4m_{WL} - m_{EWL} \tag{4.53}$$

where $m_1$ and $m_2$ represent the number of the cycle slips on L1 and L2 frequencies, respectively, $m_{WL}$ and $m_{EWL}$ are the number of the cycle slips in the WL phase and EWL phase, respectively. The efficiency of the proposed algorithm of inertial aided cycle slip detection and identification will be evaluated in Chapter 5.

# Chapter Five: Results and Analysis

This chapter uses two van field tests to verify the navigation performance of the proposed integrated PPP GPS/MEMS IMU system. One field test is conducted under a relatively open sky environment and the other one is carried out in a combined environment, which contains an urban canyon environment and a relatively open sky environment. A developed C++ program which implements the proposed integration algorithm with post-mission processing routines has been used to process the data collected from the low cost MEMS IMU and the GPS receiver and to generate the integrated navigation solutions.

## 5.1 Field Test One

This section describes the test and analysis results of the proposed integrated system under a relatively open sky environment. It begins with a field test description which includes the sensors used in the field test, operating environment and procedures adopted for data collection. The performance evaluation is carried out based on the position/velocity/attitude error results. The improvements on attitude estimates by using the 2D velocity constraints are then discussed. The GPS outages are simulated to verify the ability of MEMS IMU to bridge the gaps when GPS outages occur. Later, the efficiency of the proposed algorithm of inertial aided cycle slips detection and identification is evaluated based on a simulated cycle slip scenario and its improvements on positioning accuracy.

### *5.1.1 Field Test Description*

The MEMS IMU used in this study is the Crista IMU from Cloud Cap Technology Inc. It is a six axis measurement system consisting of three MEMS gyroscopes and three accelerometers providing temperature compensated inertial data. One specific advantage of Crista is that it has a built-in GPS pulse per second (PPS) interface which facilitates the accurate time synchronization of IMU and GPS data (Godha, 2006). The size of Crista is small (2.05" × 1.50"×1.00") and only weighs 36.8 grams (Crista- Interface Operation Documents, 2004). The Crista IMU and a NovAtel GPS receiver are built into the NavBox, which was developed by the PLAN group at The University of Calgary. The Crista IMU data is synchronized to GPS time by the NovAtel GPS receiver inside the Navbox.

Apart from the Crista IMU, a NovAtel SPAN$^{TM}$ system is also used. It consists of a NovAtel OEM4 receiver and a tactical grade HG1700AG11 IMU (HG1700). The HG1700 data is time tagged internally by the OEM4 receiver in the SPAN$^{TM}$ system. The motivation behind using the HG1700 IMU is to generate a precise reference solution to facilitate a comparative analysis. The error characteristics of both the Crista and HG1700 have been discussed in Section 1.1.

The field test started with a two minutes static alignment to allow the inertial system to determine initial attitude with sufficient accuracy (conducted only for the tactical grade unit). The equipments used were a SPAN$^{TM}$ system and the NavBox. The raw dual frequency GPS data, which includes pseudorange, carrier phase and Doppler

measurements, were logged from the SPAN$^{TM}$ system with a data rate of 1 Hz and the raw IMU data from HG1700 was logged at a rate of 100 Hz. The Crista IMU data was also collected at 100 Hz. In order to generate a reference solution using a high precision DGPS/INS integrated system, a NovAtel OEM4 receiver was setup on a building roof at The University of Calgary with excellent GPS satellites availability as the base station. The raw GPS pseudorange, carrier phase and Doppler measurements in dual-frequency were logged with a data rate of 1 Hz at the base station.

Figure 5.1 and Figure 5.2 show the field test run trajectory and satellites availability, respectively. The field test is carried out in the residential areas (Hamptons neighborhood) in Northwest Calgary, which has a relatively clear sky view. As shown in Figure 5.2, the relatively poor satellite visibilities are observed at some epochs. This is because the GPS signal from the satellite with low elevation is frequently blocked by houses or trees. The test lasts about 16 minutes and the trajectory is traversed twice.


**Figure 5.1 Field test trajectory (Field Test #1)**

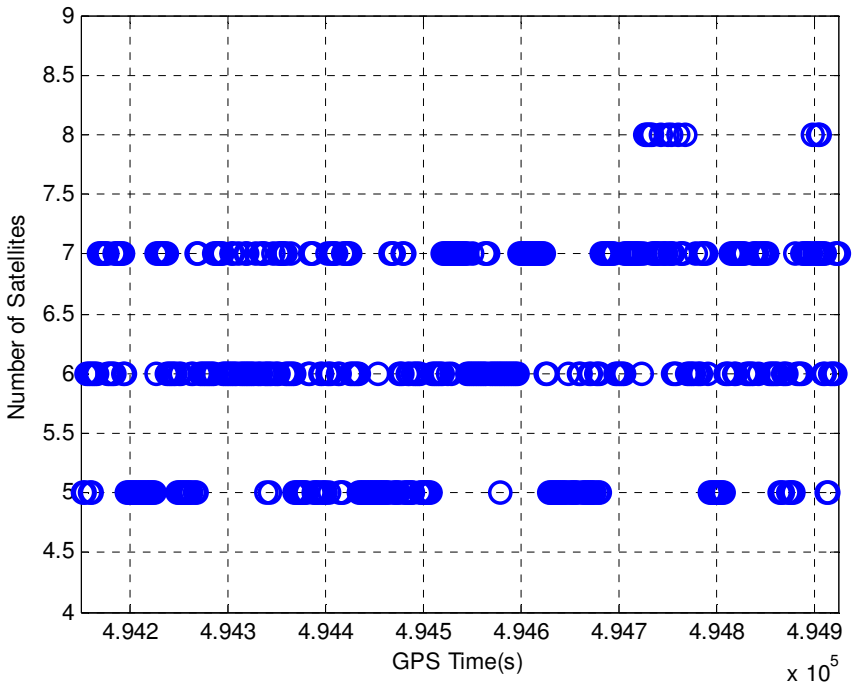


**Figure 5.2 GPS satellites availability (Field Test #1)**

### *5.1.2 Reference Navigation Solution*

In order to evaluate the navigation performance of the proposed integrated PPP GPS/MEMS IMU system, a matlab program has been developed which implements the loosely coupled integrated DGPS/INS algorithm and is used to process the DGPS solution and the HG1700 data to generate the reference navigation solution. The DGPS solution is obtained by using Waypoint GrafNav 8.10 software with ambiguity integer solution enabled. The dual frequency GPS carrier phase, pseudorange, and Doppler measurements are all used in the data processing. The ambiguity fixed position solution is obtained from the Waypoint GrafNav 8.10 software and it is accurate to better than 5 cm. The typical attitude accuracies of using tactical grade IMU, such as HG1700 is about 0.05 degree for both pitch and roll, and 0.17 degree for azimuth (Godha, 2006), which are sufficient to evaluate the performance of MEMS IMU. The noise parameter of HG1700 used in the loosely coupled DGPS/INS system is given in Table 5.1 (Petovello, 2003). Figure 5.3, Figure 5.4 and Figure 5.5 show the reference trajectory, velocity and attitude solution, respectively.

**Table 5.1 Gauss-Markov parameters for HG1700 IMU (Petovello, 2003)**

| Sensor | | Time Constant | Temporal Variance |
|---|---|---|---|
| **Gyro** | **X** | 100 min | 0.35 $deg^2/hr^2$ |
| | **Y** | 55 min | 0.34 $deg^2/hr^2$ |
| | **Z** | 84 min | 0.47 $deg^2/hr^2$ |
| **Accelerometer** | **X** | 170 min | 8.0e-8 $m^2/s^4$ |
| | **Y** | 68 min | 2.5e-7 $m^2/s^4$ |
| | **Z** | 152 min | 4.8e-7 $m^2/s^4$ |

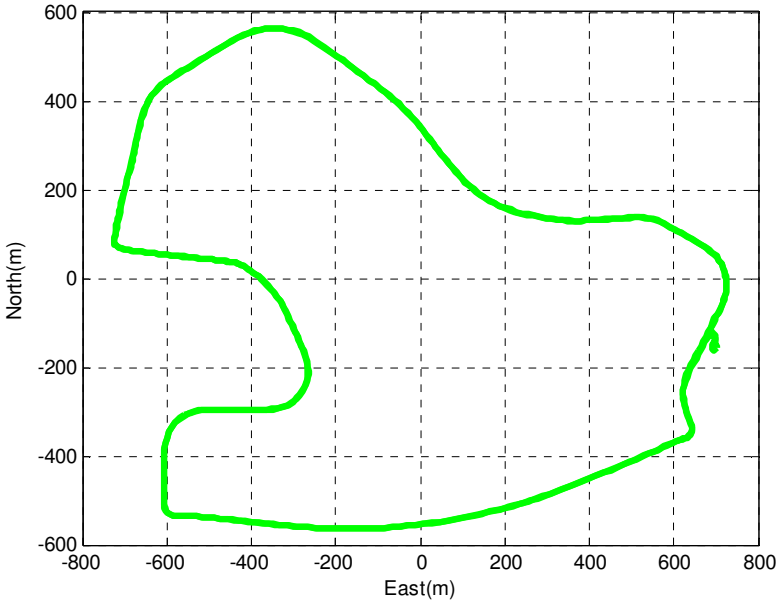


**Figure 5.3 Reference test trajectory (Field Test #1)**

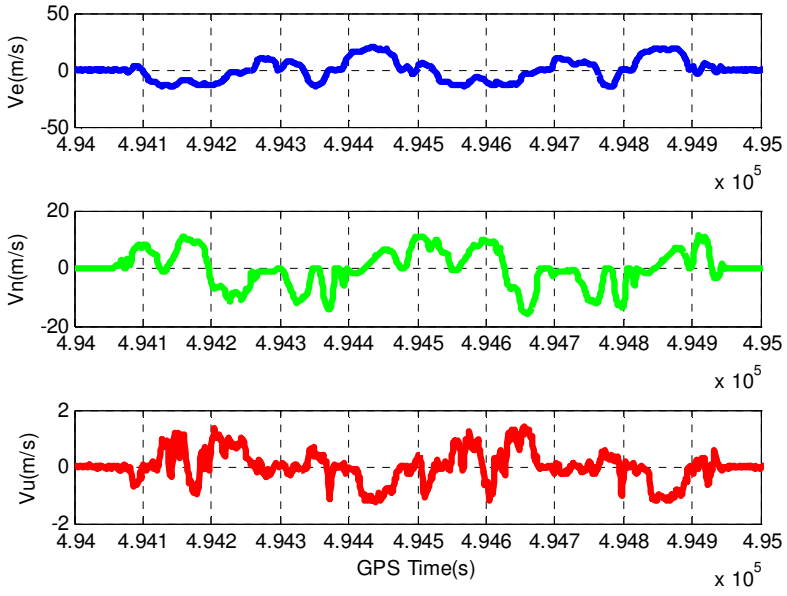


**Figure 5.4 Reference velocity solution (Field Test #1)**

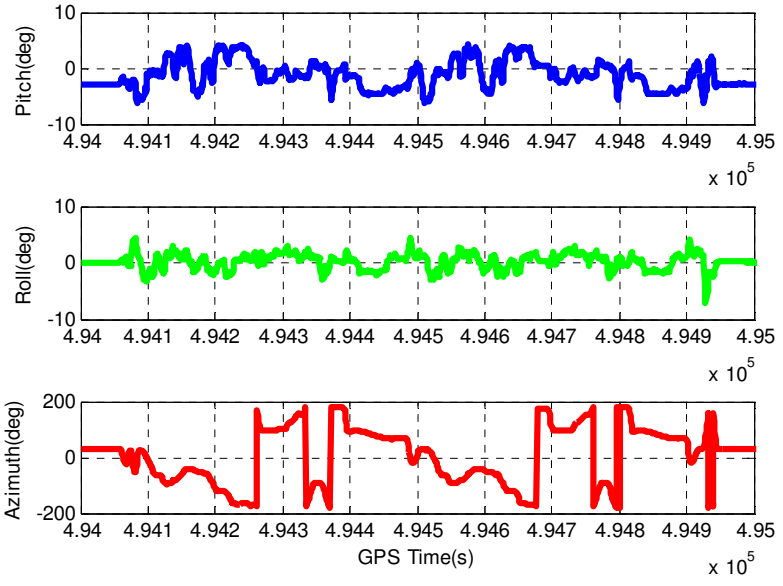


**Figure 5.5 Reference attitude solution (Field Test #1)**

### *5.1.3 PPP GPS Results*

In order to assess the performance of the integrated PPP GPS and MEMS IMU system, it is necessary to verify the performance of the aiding source, which is the PPP GPS. Figure 5.6 presents the satellites geometry. Although the HDOP values are less than 2 in majority of the time, which demonstrates good horizontal satellite geometry, the VDOP values are relatively poor at some epochs. The spectral densities used in the PPP filter (described in Chapter 4) are given in Table 5.2.

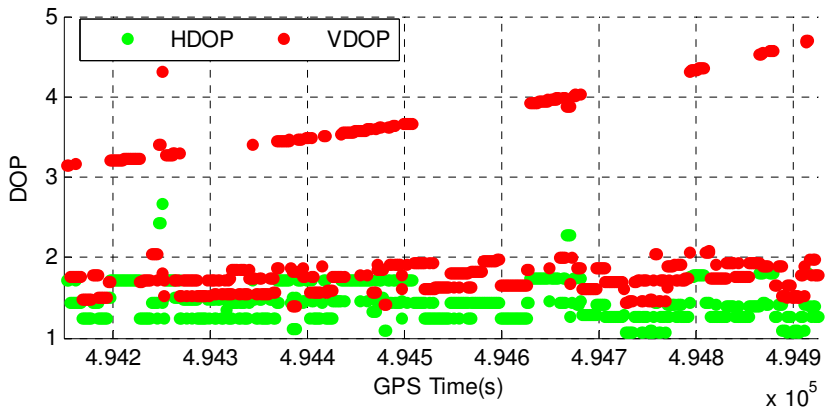


**Figure 5.6 Satellites geometry (Field Test #1)**

**Table 5.2 Spectral densities used in PPP**

| **Spectral Densities** | $q_{V_E}(m^2/s^3)$ | $q_{V_N}(m^2/s^3)$ | $q_{V_U}(m^2/s^3)$ | $q_{V_{dt}}(m^2/s^3)$ | $q_{trop}(m^2/s)$ |
|---|---|---|---|---|---|
| **Values** | 10 | 10 | 10 | 100 | 1e-9 |

Figure 5.7 shows the PPP GPS position error time series. The position solution in PPP GPS requires a convergence time before it can achieve centimetre to decimetre level accuracy due to the fact that the ambiguity terms are estimated as float numbers and they require a time period to converge to their true values. Normally the required convergence time is 20-40 minutes for the solution to be at centimetre to decimetre level. Since the duration of the field test is about 16 minutes, the ambiguities in the carrier phase measurements have not completely converged. As a result, a backward processing is employed to improve the obtainable accuracy.

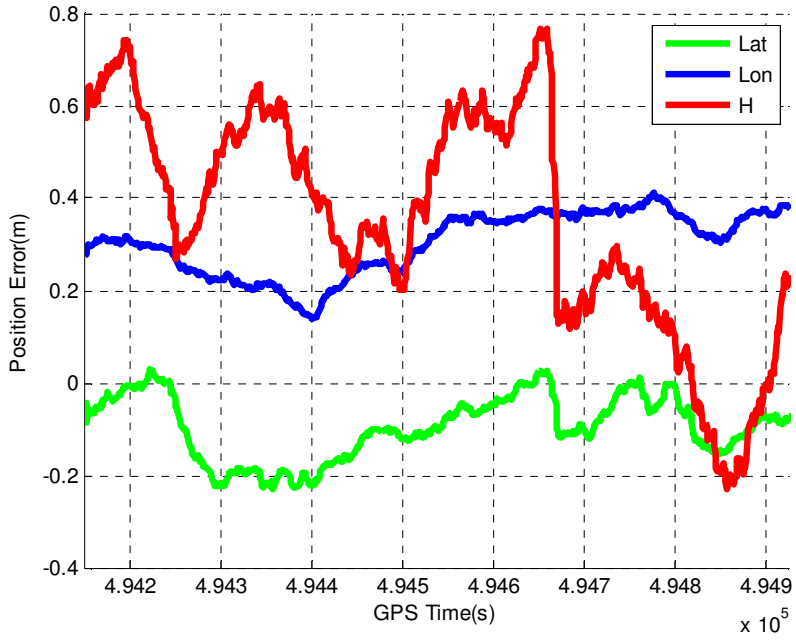


**Figure 5.7 PPP GPS position error (Field Test #1)**

As shown in Figure 5.7, the latitude and longitude errors are well bounded within half-metre during the entire run, while the height error is relatively large comparing to the

latitude and longitude errors due to the larger VDOP values. A statistical summary of the position error is presented in Table 5.2. The horizontal and vertical position errors are 0.34 m and 0.47 m, respectively. With longer duration of the field test, the position accuracy is expected to be further improved.

Figure 5.8 presents the PPP GPS velocity error time series. There is no convergence time required for velocity estimation since the velocity estimate highly depends on the Doppler measurements. The Table 5.2 lists the velocity error statistics. The horizontal and vertical velocity errors are 3.1 cm/s and 7.6 cm/s, respectively.

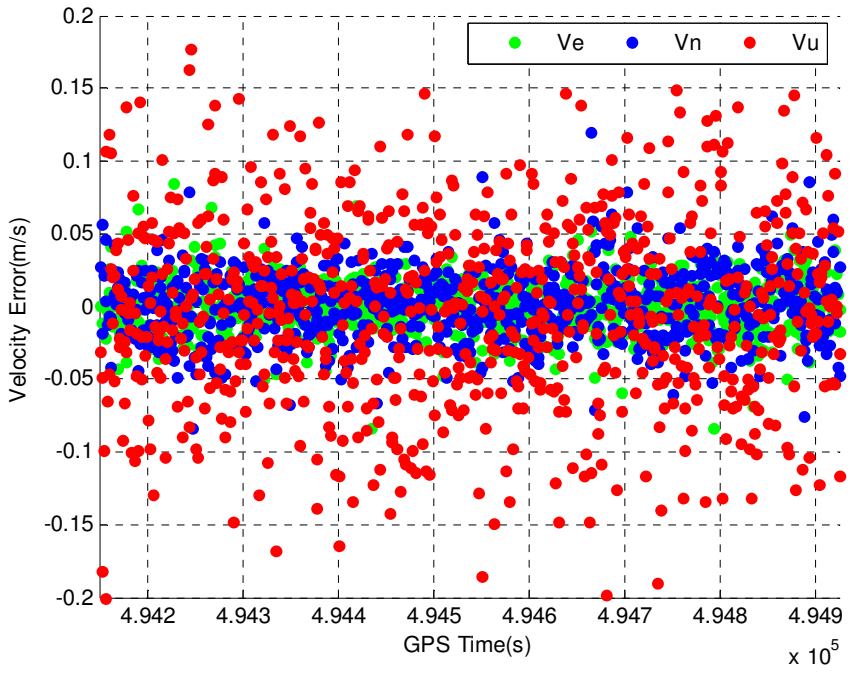


**Figure 5.8 PPP GPS velocity error (Field Test #1)**

**Table 5.3 RMS error results of PPP GPS solution (Field Test #1)**

| **Position Error (m)** | | | | |
|---|---|---|---|---|
| **Lat** | **Lon** | **H** | **Horizontal** | **3D** |
| 0.10 | 0.32 | 0.47 | 0.34 | 0.58 |
| **Velocity Error (m/s)** | | | | |
| **Vn** | **Ve** | **Vu** | **Horizontal** | **3D** |
| 0.019 | 0.025 | 0.076 | 0.031 | 0.082 |

Based on these results, we can see that the PPP GPS offers better than half metre level accuracy for position and centimetre to sub-decimetre per second level accuracy for velocity. Due to the short duration of the field test, the ambiguity did not converge completely and the PPP GPS was not able to achieve the centimetre to decimetre level accuracy. Based on the obtained accuracy of the PPP GPS solution, a similar accuracy is expected from the integrated PPP GPS/MEMS IMU system.

### *5.1.4 Integrated PPP GPS/MEMS IMU System Results*

This section describes the test results of both the tightly and loosely coupled integrated PPP GPS/MEMS IMU system. The GPS pseudorange, carrier phase and Doppler measurements are all used in data processing and the results are obtained with the cycle slip detection and identification enabled. Due to the short duration of the field test, the backward processing is used in both the tightly and loosely coupled integrated systems. The stochastic model parameters for inertial sensors are given in Table 5.4 and 5.5. In

the following sections, the position accuracy is presented first, followed by the velocity and attitude accuracies.

**Table 5.4 Model parameters for bias drifts of gyros and accelerometers**

| | **Gyros** | | **Accelerometers** | |
|---|---|---|---|---|
| | **σ (degree/hr)** | **τ (s)** | **σ ($m/s^2$)** | **τ (s)** |
| **X** | 240 | 400 | 7e-3 | 250 |
| **Y** | 200 | 350 | 7e-3 | 200 |
| **Z** | 180 | 300 | 8e-3 | 340 |

**Table 5.5 Model parameters for scale factors of gyros and accelerometers (Godha, 2006)**

| | **Gyros** | | **Accelerometers** | |
|---|---|---|---|---|
| | **σ (PPM)** | **τ (s)** | **σ (PPM)** | **τ (s)** |
| **X** | 10000 | 18000 | 1000 | 18000 |
| **Y** | 10000 | 18000 | 1000 | 18000 |
| **Z** | 10000 | 18000 | 1000 | 18000 |

5.1.4.1 Position Accuracy

Shown in Figure 5.9 are the position error results obtained from the tightly coupled integrated PPP GPS/MEMS IMU system. Since more than 4 satellites are available throughout the entire run, the position error can be continuously corrected with the GPS updates. As a result, it prevents the INS error accumulation. The tightly coupled

integrated system offers similar results comparing to the PPP GPS. A statistical summary of the position errors are given in Table 5.3. The horizontal and vertical position errors are 0.27 m and 0.38 m, respectively.

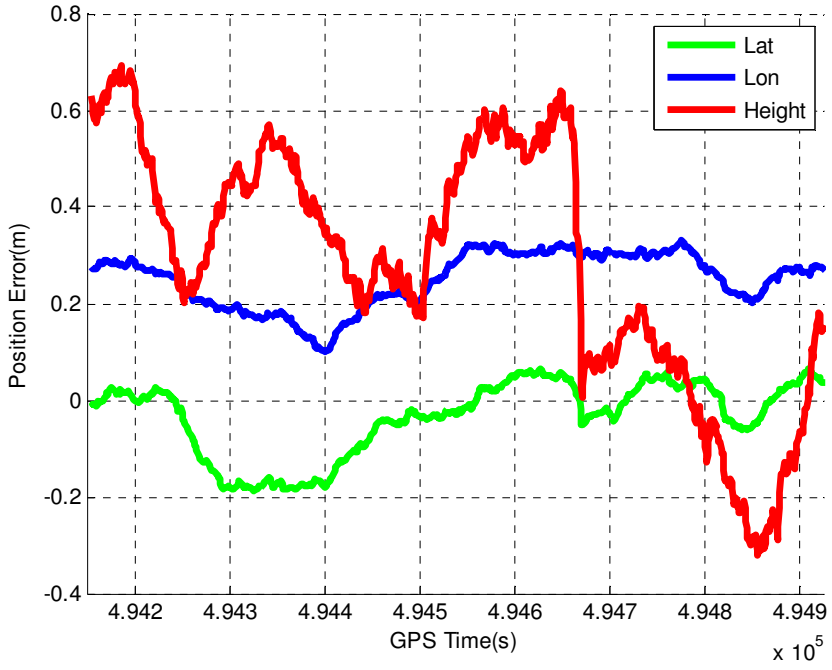


**Figure 5.9 Tightly coupled PPP GPS/MEMS IMU position error (Field Test #1)**

A statistical summary of the position errors of the loosely coupled integrated system is also listed in Table 5.3. The horizontal and vertical position errors are 0.32 m and 0.39 m, respectively. The results indicate that the tightly coupled system slightly outperforms the loosely coupled system under the relatively open sky environments. This is because GPS and INS information are more rigorously modeled in the tightly coupled system than a loosely coupled system.

**Table 5.6 RMS position error results of PPP GPS/MEMS IMU (Field Test #1)**

| RMS | Lat (m) | Lon (m) | Height (m) | Horizontal (m) | 3D (m) |
|---|---|---|---|---|---|
| **TC** | 0.08 | 0.26 | 0.38 | 0.27 | 0.47 |
| **LC** | 0.10 | 0.30 | 0.39 | 0.32 | 0.50 |

As demonstrated in Table 5.3, improvements are observed on the position solutions in the integrated PPP GPS/MEMS IMU system comparing to the PPP GPS position solutions. These improvements are associated with the successful fixing the detected cycle slips by using the developed algorithm of inertial aided cycle slip detection and identification. More details will be discussed later in Section 5.1.5.

5.1.4.2 Velocity Accuracy

Provided in Figure 5.10 are the velocity error time series obtained from the tightly coupled integrated system. The velocity errors in the east and north directions are well bounded in 5 cm/s, and the velocity error in the up direction is well below 10 cm/s in most of the time.

Table 5.4 lists a statistical summary of the velocity errors. In the tightly coupled integrated system, the horizontal and vertical velocity errors are 2.9 cm/s and 7.3 cm/s, respectively. Similar velocity accuracies are obtained in the loosely coupled integrated system.

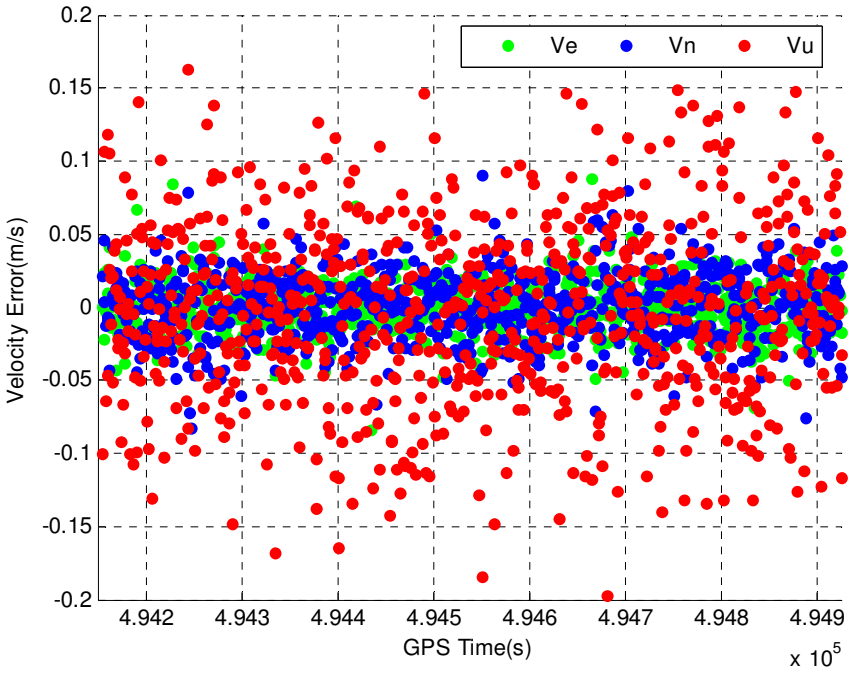


**Figure 5.10 Tightly coupled PPP GPS/MEMS IMU velocity error (Field Test #1)**

**Table 5.7 RMS velocity error results of PPP GPS/MEMS IMU (Field Test #1)**

| RMS | Vn (m/s) | Ve (m/s) | Vu (m/s) | Horizontal (m/s) | 3D (m/s) |
|---|---|---|---|---|---|
| **TC** | 0.018 | 0.023 | 0.073 | 0.029 | 0.079 |
| **LC** | 0.019 | 0.025 | 0.073 | 0.031 | 0.080 |

As shown in Table 5.3 and 5.4, the proposed integrated system offers the horizontal and vertical position accuracies at 0.3 m and 0.4 m, respectively, and the velocity accuracy at centimetre to sub-decimetre per second under relatively open sky environment. Although it does not achieve the centimetre to decimetre level accuracy due to the short duration of

the field test, the results are promising since only a single dual-frequency GPS receiver is used.

5.1.4.3 Attitude Accuracy

Figure 5.11 shows the attitude error time series obtained from the tightly coupled integrated PPP GPS/MEMS IMU system. The pitch and roll errors are well bounded within 1 degree in the majority of the time, while the azimuth error is larger than the pitch and roll errors. Given in Table 5.5 is a statistical summary of the attitude errors in the tightly coupled system. The pitch and roll errors are 0.44 degree and 0.37 degree, respectively, while the azimuth error is as large as 1.41 degrees. In INS there are strong couplings between the velocity error in the east direction and the roll error, and between the velocity error in the north direction and the pitch error. The coupling between the horizontal velocity errors and the azimuth error is much weaker. If two INS error states are strongly coupled and one of them can be accurately estimated, then the other error state can be estimated accurately too. As a result, the accurate estimation of the velocity in the integrated system leads to more accurate roll and pitch solutions than the azimuth solution.

Since the low cost MEMS IMU has much higher magnitudes of sensor errors comparing to the tactical grade IMU, the attitude accuracies are much poorer than the tactical grade IMU. The results indicate that the attitude accuracies heavily depend on the grade of the IMU used.

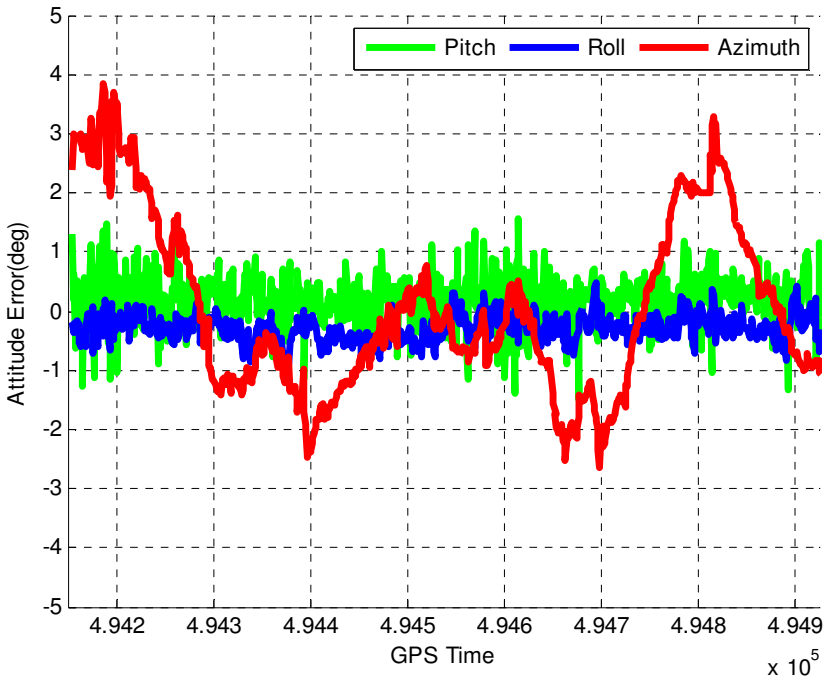


**Figure 5.11 Tightly coupled PPP GPS/MEMS IMU attitude error (Field Test #1)**

The statistics of the attitude errors in the loosely coupled system are also summarized in Table 5.5. Similar attitude accuracies are obtained from the loosely coupled integrated system. Godha (2006) and Li (2009) investigated the integrated DGPS/MEMS IMU system using the same equipments and their results indicated that the integrated DGPS/MEMS IMU system offers the pitch and roll accuracies at 0.3~0.5 degree, and the azimuth accuracy at 1.2~1.6 degrees without applying any non-holonomic dynamic constraints. The proposed integrated PPP GPS/MEMS IMU system offers similar attitude accuracies comparing to their results.

**Table 5.8 RMS attitude error results of PPP GPS/MEMS IMU (Field Test #1)**

| RMS | Pitch (degree) | Roll (degree) | Azimuth (degree) |
|---|---|---|---|
| **TC** | 0.44 | 0.37 | 1.41 |
| **LC** | 0.46 | 0.43 | 1.42 |

### *5.1.5 Results with 2D Velocity Constraints*

For the ground vehicles, it has been found that the non-holonomic constraints can be used in the integrated GPS/INS system under benign environments to improve the attitude accuracies (Li, 2009; Niu et al, 2006). The constraints used in this study are the 2D velocity constraints. Shown in Figure 5.12 is the attitude error time series with the tightly coupled integrated system after applying the 2D velocity constraints. Although improvements on both pitch and roll estimates are relatively small, significant improvements are observed on the azimuth estimate.

Table 5.6 presents a statistical summary of the tightly coupled integrated system attitude errors after applying the constraints. Improvements are observed on all attitude components, for instance, the pitch and roll accuracies are improved by 4.6% and 5.4%, respectively, and the azimuth accuracy is improved by 46.8%. As discussed before, the velocity error in the body frame is correlated with the attitude error states, as a result the use of the 2D velocity constraints improves the observability of the attitude estimates, and eventually improve the attitude accuracies.

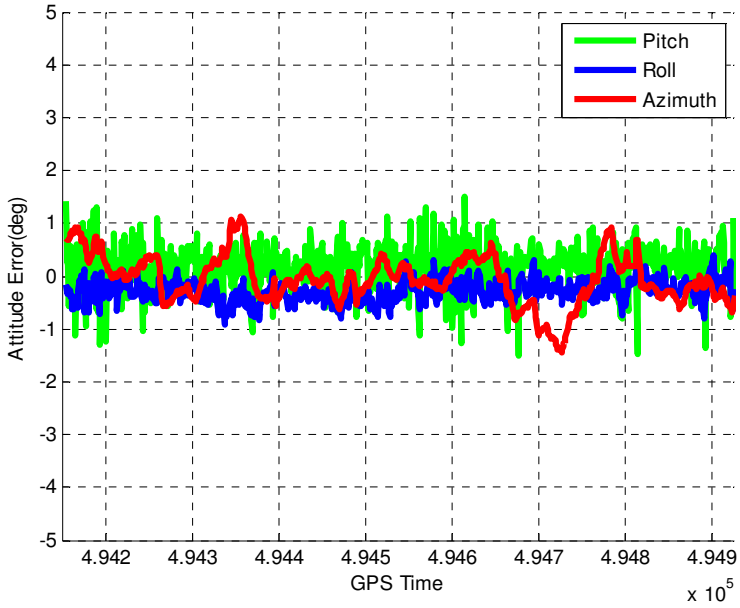


**Figure 5.12 Tightly coupled PPP GPS/MEMS IMU attitude error with 2D velocity constraints (Field Test #1)**

**Table 5.9 RMS attitude error results of tightly coupled PPP GPS/MEMS IMU with 2D velocity constraints (Field Test #1)**

| | **Pitch (degree)** | **Roll (degree)** | **Azimuth (degree)** |
|---|---|---|---|
| **No Constraints** | 0.44 | 0.37 | 1.41 |
| **2D Velocity** | 0.42 | 0.35 | 0.75 |
| **Improvements** | 4.6% | 5.4% | 46.8% |

Table 5.7 presents a statistical summary of the loosely coupled integrated system attitude errors after applying the 2D velocity constraints. The pitch and roll accuracies are improved by 6.5% and 4.7%, respectively, and the azimuth accuracy is improved by 43.7%.

**Table 5.10 RMS attitude error results of loosely coupled PPP GPS/MEMS IMU with 2D velocity constraints (Field Test #1)**

| | Pitch (degree) | Roll (degree) | Azimuth (degree) |
|---|---|---|---|
| **No Constraints** | 0.46 | 0.43 | 1.42 |
| **2D Velocity** | 0.43 | 0.41 | 0.80 |
| **Improvements** | 6.5% | 4.7% | 43.7% |

### *5.1.6 Results with GPS outages*

One advantage of the integrated GPS/INS system is that the INS can bridge the GPS outages when GPS signals are blocked or subject to severe degradation. This section discusses the ability of the MEMS IMU in the integrated PPP GPS/MEMS IMU system to bridge the GPS outages, which include both complete and partial outages. The GPS outages are simulated by rejecting the GPS satellites in data processing. The position error results under complete GPS outages are firstly presented, and then followed by the results under partial GPS outages. The GPS data and Crista IMU data are processed with the tightly coupled integrated system because of its specific advantages under partial GPS availability. The positioning accuracy improvements by using the 2D velocity constraints during the GPS outages are also discussed.

#### 5.1.6.1 Results with Complete GPS Outage

A total of six GPS complete outages are simulated at different dynamic environments: 2 over high dynamic periods, 2 over moderate dynamic periods and 2 over low dynamic periods. All outages last for 30 seconds and it is given at least 55 seconds for the

integration filter to re-converge before the next outage. The GPS data and Crista IMU data are firstly processed without the constraints to obtain a baseline performance of the integrated system under complete GPS outages. The position errors are computed as a function of the time elapsed since the last GPS update for each outage.

Figure 5.13 shows the horizontal position error during the six GPS outages. During the GPS outages, the integration filter works in a pure prediction mode, and its solution therefore entirely relies on the INS mechanization algorithm. The position error is accumulated since the GPS outages start. The drifting INS error during the GPS outages primarily depends on the inertial sensor errors and the time-span of the GPS outage. For all the GPS gaps, the maximum errors range from about 17 m to about 50 m.

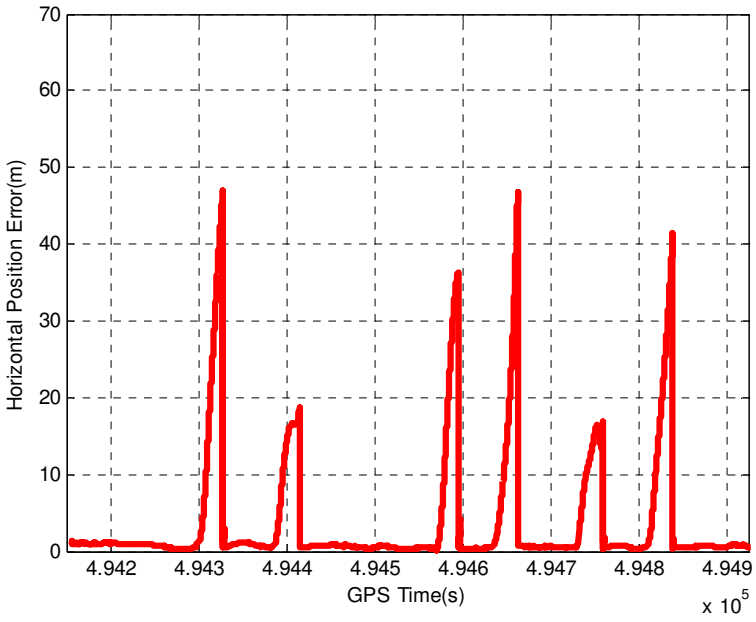


**Figure 5.13 Horizontal position error of PPP GPS/MEMS IMU under complete GPS outages (Field Test #1)**

As discussed previously, one way to improve the system performance during GPS outages is to use the non-holonomic constraints. Figure 5.14 shows the horizontal position error during the GPS outages after applying the 2D velocity constraints. As shown in the figure, the performance is significantly improved, the maximum horizontal position error is less than 13 m during all complete GPS outages.

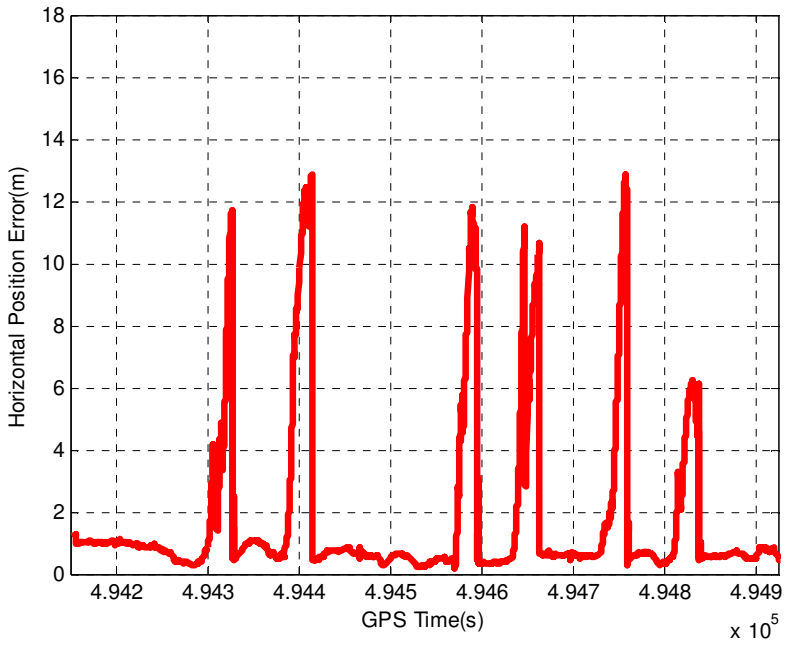


**Figure 5.14 Horizontal position error of PPP GPS/MEMS IMU under complete GPS outages with 2D velocity constraints (Field Test #1)**

The RMS position error during GPS outages is calculated (Petovello, 2003; Godha, 2006) and provided in Figure 5.15. The green and red lines represent the RMS position error with and without applying the 2D velocity constraints. As demonstrated in the figure, the RMS position error starts to grow right after the GPS outage occurs. During a 30-second

complete GPS outage, the RMS position error increases to about 37 m. The position drift error is typically large. By applying the 2D velocity constraints, the positioning performance is significantly improved, since the maximum RMS position error is reduced to about 11 m.

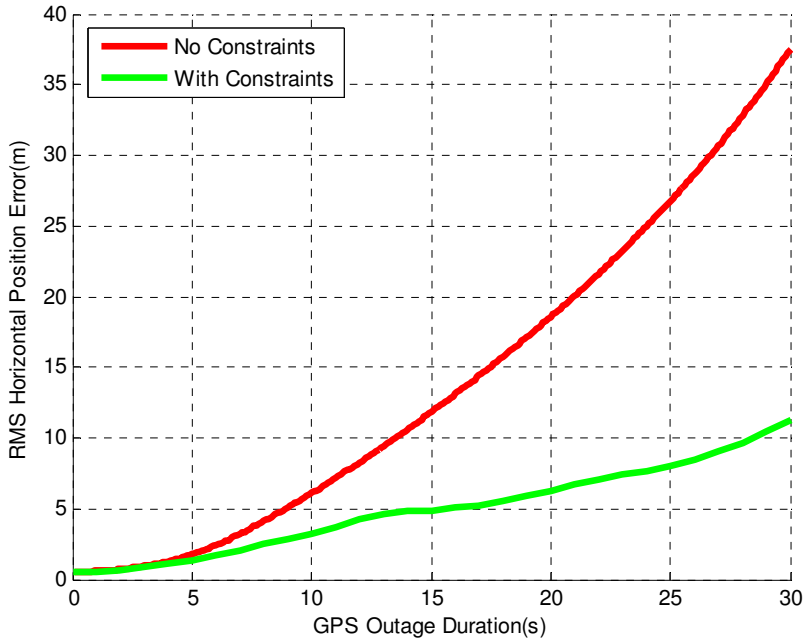


**Figure 5.15 RMS horizontal position error during complete GPS outages (Field Test #1)**

5.1.6.2 Results with Partial GPS Outages

Having discussed the ability of the MEMS IMU in the integrated system to bridge the complete GPS outages, its positioning performance under partial GPS outages are discussed here. The six time periods used to simulate the complete GPS outages are adopted again to simulate the partial GPS outages, during which only 2 or 3 satellites are available. The partial GPS outages with 3 satellites available are firstly simulated by

increasing the satellite elevation mask for the adopted six periods of time; then the elevation mask are further raised for these periods to simulate the partial GPS outages with 2 satellites available.

Shown in Figure 5.16 is the computed RMS position error for all 30-second partial GPS outages. The solid line represents the RMS position errors when 2 satellites are available, while the dot line represents the RMS position errors when 3 satellites are available. The green and red colors represent the RMS position errors with and without applying the 2D velocity constraints, respectively.

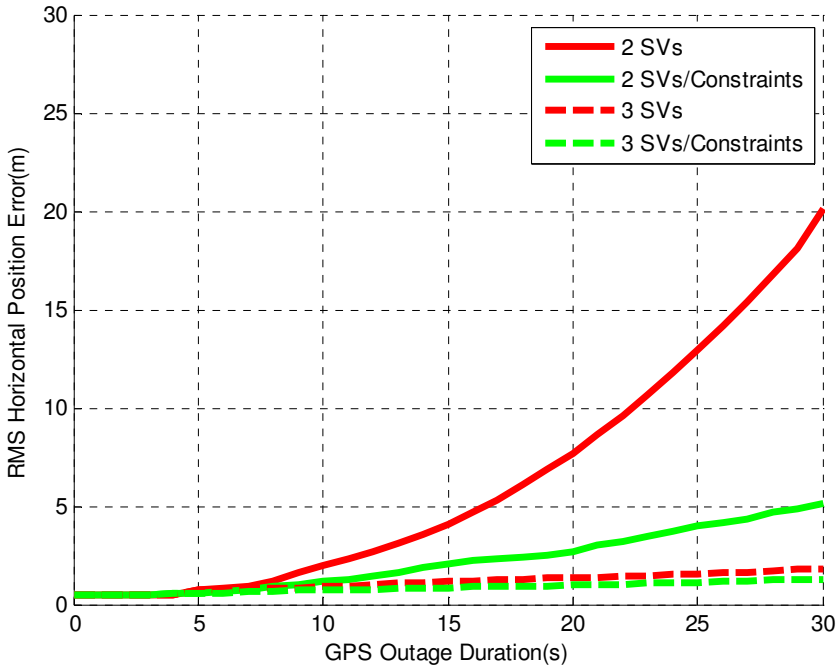


**Figure 5.16 RMS horizontal position error during partial GPS outages (Field Test #1)**

During the partial GPS outages, the performance of the integrated system mainly depends on the sensor error characteristics, the number of satellites, and the geometry of the available satellites (Godha, 2006). As shown in the figure, when with 2 satellites available, the INS error is still accumulating, although the rate of accumulation is damped. As a result, the RMS horizontal position error is reduced to about 20m. When with 3 satellites available, the RMS horizontal position error is further reduced to be less than 2 m. Improvements are still observed on positioning accuracy after applying the 2D velocity constraints. The RMS horizontal position error is reduced to about 5 m when with 2 satellites available and 1.5 m when with 3 satellites available by using the 2D velocity constraints.

### *5.1.7 Inertial Aided Cycle Slip Detection and Identification Results*

It is well known that undetected cycle slips would deteriorate the accuracy of carrier phase measurements and eventually degrade the navigation performance. This section discusses the efficiency of the proposed inertial aided cycle slip detection and identification algorithm. As it is difficult to verify the efficiency of the algorithm without knowing the truth, a cycle slip scenario is simulated. The improvements on the positioning accuracy are also presented.

Before any cycle slip scenario is simulated, the decision variables (referred to Section 4.5) should be analyzed. Provided in Figure 5.17 and Figure 5.18 are the decision variables for the GPS satellites during the entire test period. The GPS satellite PRN20 has the highest elevation and is used as the base satellite to compute the decision variables. The

blue dot and the red dot represent the computed decision variable based on the widelane phase combination and the extra-widelane phase combination, respectively. The epochs which have cycle slips have been removed in both Figure 5.17 and 5.18 to provide a clear view of the values of the decision variables.

Based on the assumptions made in the Section 4.5, if the carrier phase measurement to a GPS satellite is free of cycle slips, then the decision variable is Gaussian distributed with a mean value of zero. This can be confirmed in Figure 5.17 and Figure 5.18 that all decision variables are normal distributed and centered at zero. As shown in the figures, PRN4, PRN13, PRN25 and PRN30 have low elevations ranging 7~18 degrees and they can only be tracked for certain periods of time due to the signal blockage by trees or houses, whereas the satellites (PRN23, PRN31 and PRN32) with high elevation angles can be tracked continuously during the entire time period. Due to the lower elevation angles, the decision variables for PRN4, PRN13, PRN25 and PRN30 are much noisier than the decision variables for the rest satellites.

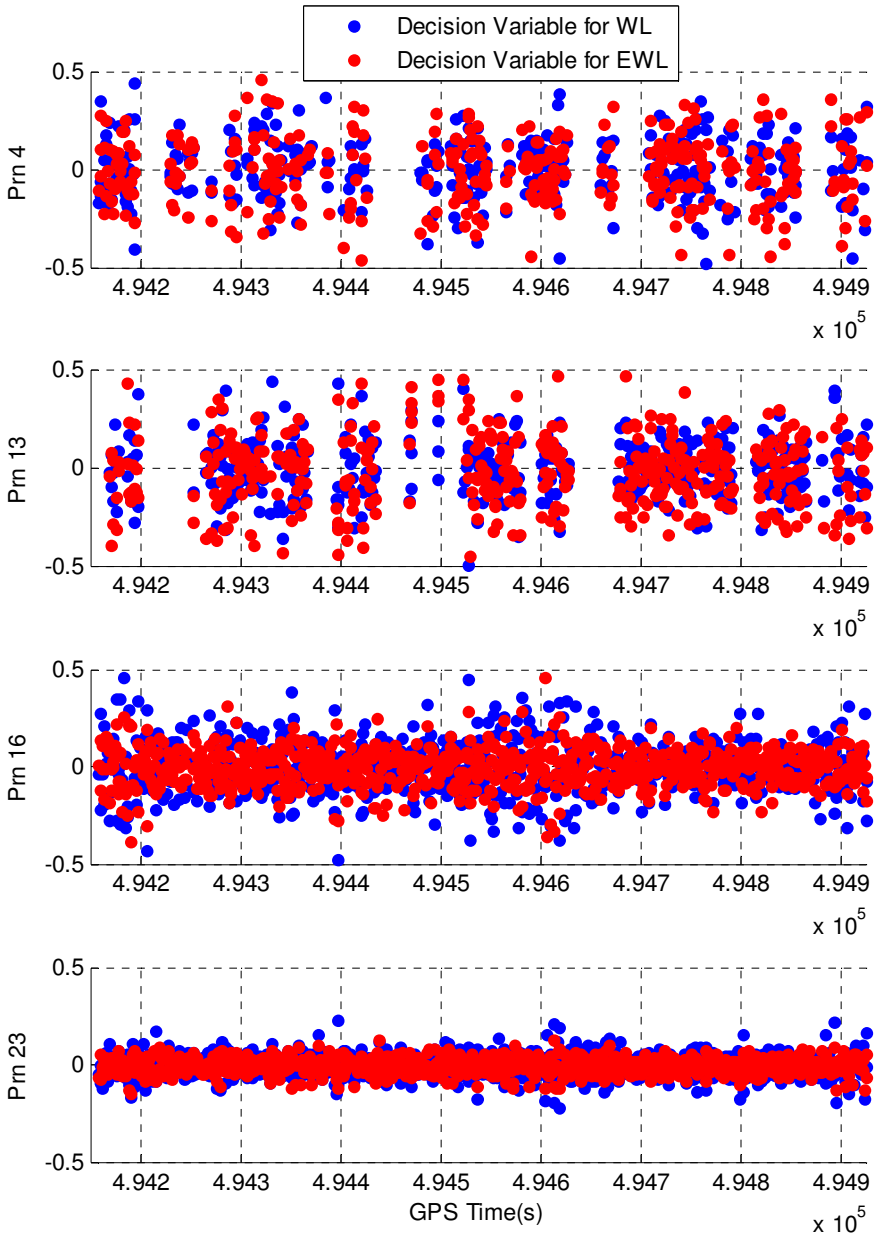


**Figure 5.17 Decision variables for PRN4, PRN13, PRN16 and PRN23 (Field Test #1)**

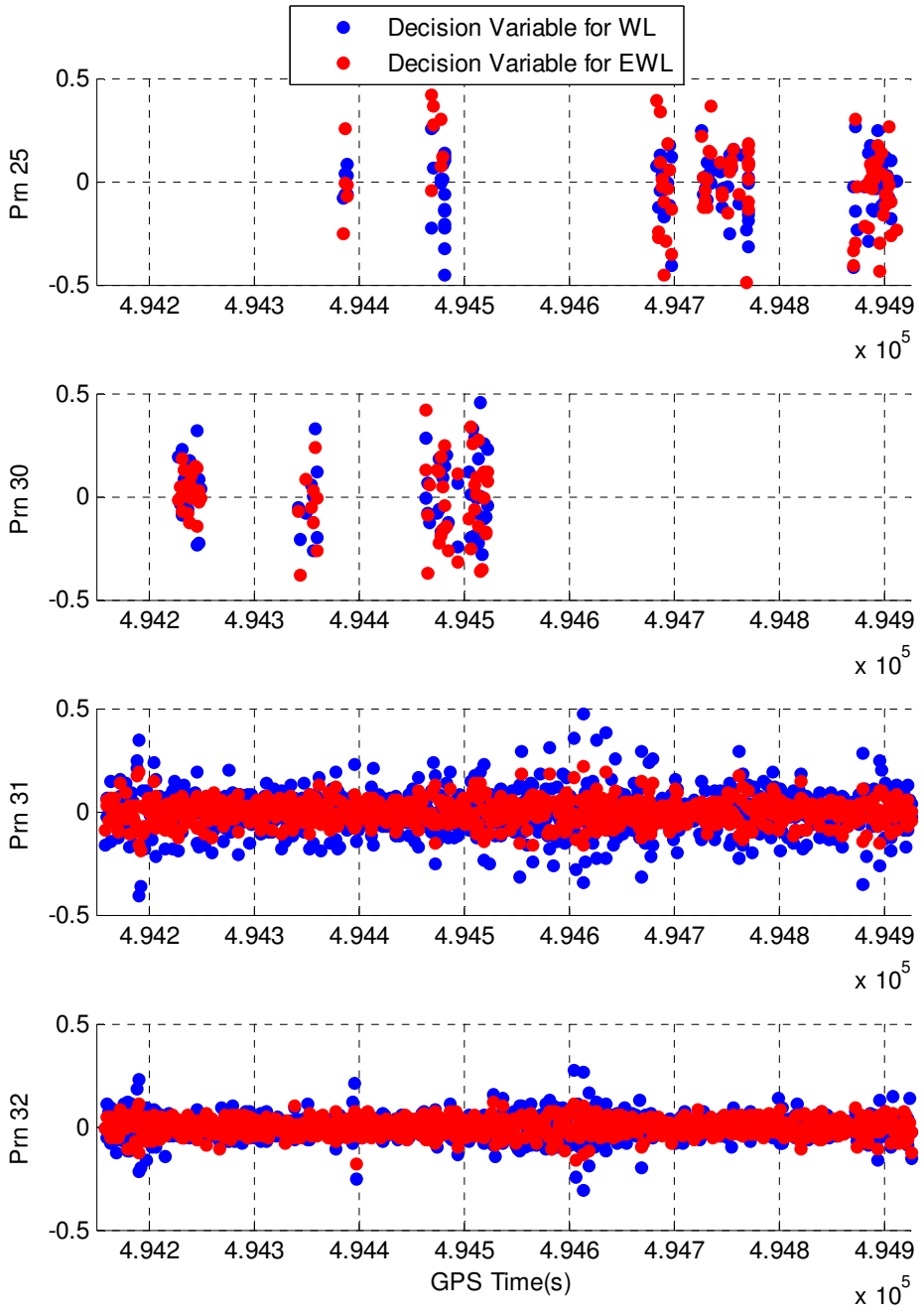


**Figure 5.18 Decision variables for PRN25, PRN30, PRN31 and PRN32 (Field Test #1)**

As discussed in Section 4.5, the testing probabilities such as the probabilities of the false alarm, missed detection, right determination and false determination are highly dependent upon the selected threshold and the estimated standard deviation of the decision variable. Summarized in Table 5.8 are the standard deviations of the decision variables for all satellites in view.

**Table 5.11 STD of the decision variables (Field Test #1)**

| **PRN** | **4** | **13** | **16** | **23** | **25** | **30** | **31** | **32** |
|---|---|---|---|---|---|---|---|---|
| **DV for WL (cycle)** | 0.15 | 0.13 | 0.12 | 0.06 | 0.13 | 0.17 | 0.10 | 0.06 |
| **DV for EWL (cycle)** | 0.17 | 0.17 | 0.09 | 0.04 | 0.18 | 0.17 | 0.06 | 0.04 |

As shown in the table, the standard deviations of the decision variables for all satellites in view are less than 0.2 cycles. The standard deviations of the decision variables for PRN4, PRN13, PRN25 and PRN30 are larger than that of the rest satellites due to the lower elevation angles.

Having analyzed the decision variables for widelane and extra-widelane phase combinations, the cycle slip scenario is simulated as shown in Table 5.9. Different number of cycle slips is simulated on both L1 and L2 frequencies for all satellites in view.

**Table 5.12 Simulated cycle slips scenario I**

| Satellite PRN | GPS time (s) | Cycle Slips on L1 (cycle) | Cycle Slip on L2 (cycle) |
|---|---|---|---|
| **4** | 494410 | 1 | 0 |
| **13** | 494196 | 0 | -1 |
| **16** | 494330 | 5 | -8 |
| **23** | 494550 | 1 | 10 |
| **25** | 494386 | -20 | 3 |
| **30** | 494232 | 5 | 6 |
| **31** | 494610 | 3 | 1 |
| **32** | 494730 | 15 | 12 |

In this study, the threshold of cycle slip detection and identification for all satellites in view are set to 0.5 cycles and the corresponding testing probabilities are provided in Table 5.10 based on Equation (4.44), (4.45), (4.49) and (4.50). The FA, MD, RD and FD represent the false alarm, missed detection, right determination and the false determination, respectively. If the calculated probability is smaller than 1e-10, it will be given as zero, and if it is larger than 1-1e-10, then it will be given as one.

**Table 5.13 Testing probabilities (Field Test #1)**

| | Widelane Phase Combination | | | | Extra-Widelane Phase Combination | | | |
|---|---|---|---|---|---|---|---|---|
| **PRN** | **FA** | **MD** | **RD** | **FD** | **FA** | **MD** | **RD** | **FD** |
| **4** | 3e-6 | 1e-6 | 1-3e-6 | 3e-6 | 4e-5 | 2e-5 | 1-4e-5 | 4e-5 |
| **13** | 3e-7 | 1e-7 | 1-3e-7 | 3e-7 | 8e-5 | 4e-5 | 1-8e-5 | 8e-5 |
| **16** | 2e-8 | 9e-9 | 1-2e-8 | 2e-8 | 0 | 0 | 1 | 0 |
| **23** | 0 | 0 | 1 | 0 | 0 | 0 | 1 | 0 |
| **25** | 7e-8 | 4e-8 | 1-7e-8 | 7e-8 | 2e-4 | 1e-4 | 1-2e-4 | 2e-4 |
| **30** | 5e-5 | 2e-5 | 1-5e-5 | 5e-5 | 9e-5 | 4e-5 | 1-9e-5 | 9e-5 |
| **31** | 0 | 0 | 1 | 0 | 0 | 0 | 1 | 0 |
| **32** | 0 | 0 | 1 | 0 | 0 | 0 | 1 | 0 |

Figure 5.19 and Figure 5.20 show the decision variables for the GPS satellites with simulated cycle slips. As expected the cycle slips deteriorate the Gaussian characteristics of the decision variable. Some large values of the decision variables are observed at some epochs and they indicate that cycle slips occurred.

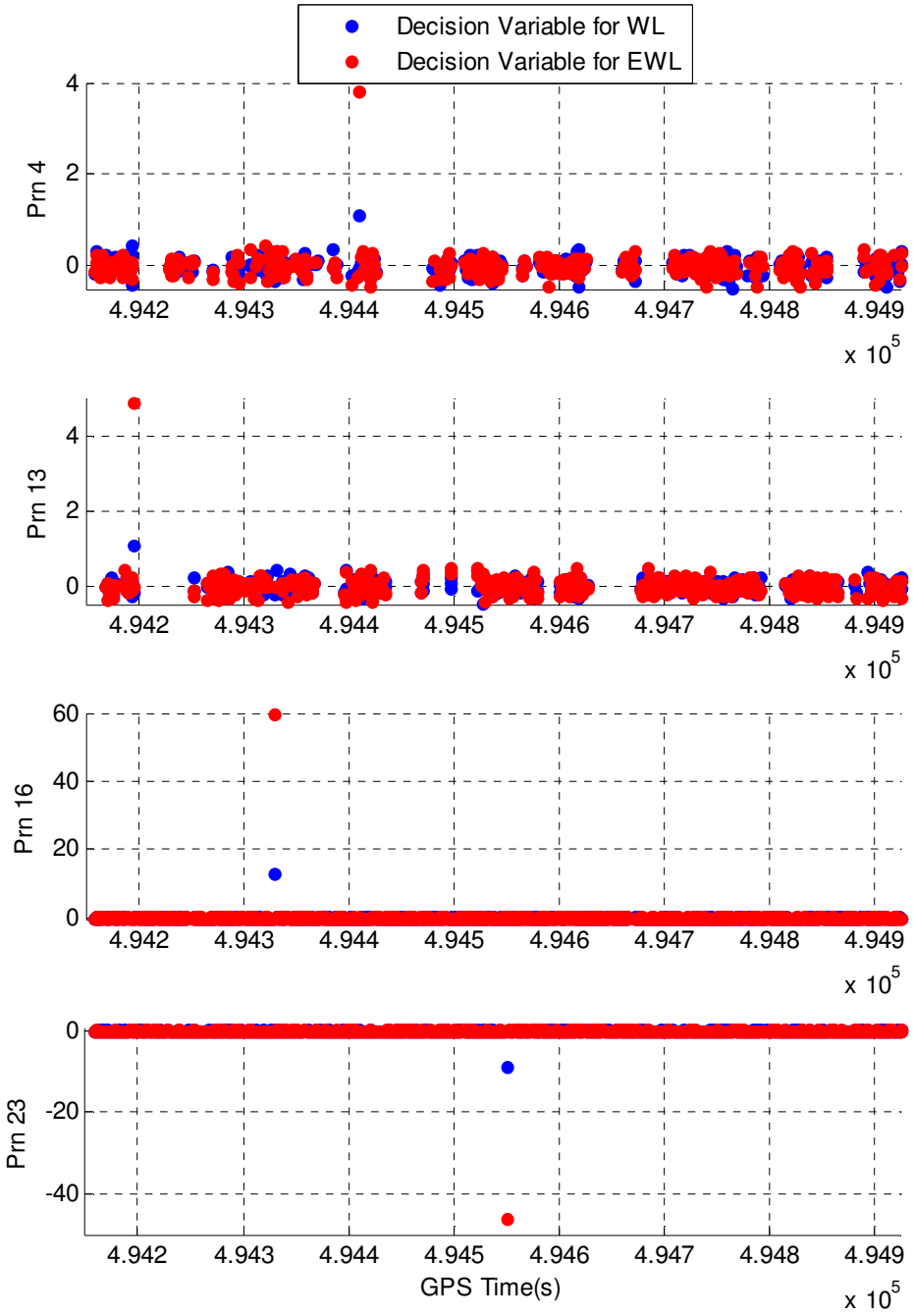


**Figure 5.19 Decision variables for PRN4, PRN13, PRN16 and PRN23 with simulated cycle slips (Field Test #1)**

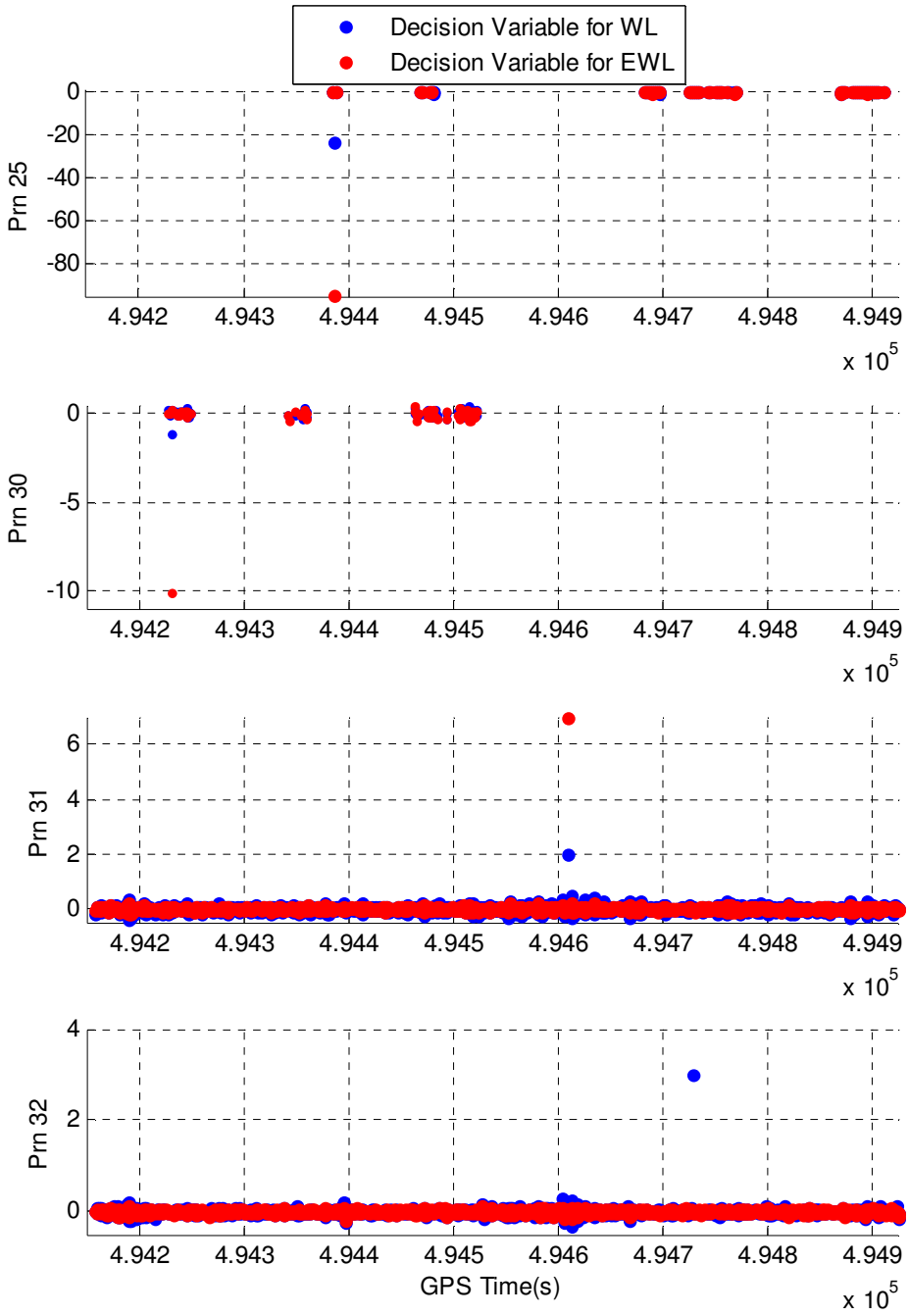


**Figure 5.20 Decision variables for PRN25, PRN30, PRN31 and PRN 32 with simulated cycle slips (Field Test #1)**

Table 5.11 summarized the detected and identified cycle slips using the proposed algorithm. The columns 5-8 give the identified cycle slips on WL phase, EWL phase, L1 phase and L2 phase, respectively. Based on the identified WL and EWL cycle slips, the cycle slips on both L1 and L2 frequencies are identified. Comparing to the simulated cycle slip scenario given in Table 5.9, all simulated cycle slips have been correctly identified.

**Table 5.14 Identified cycle slips in simulated cycle slip scenario I**

| PRN | GPS time (s) | DV/WL (cycle) | DV/EWL (cycle) | CS/WL (cycle) | CS/EWL (cycle) | CS/L1 (cycle) | CS/L2 (cycle) |
|---|---|---|---|---|---|---|---|
| **4** | 494410 | 1.12 | 3.83 | 1 | 4 | 1 | 0 |
| **13** | 494196 | 1.07 | 4.89 | 1 | 5 | 0 | -1 |
| **16** | 494330 | 12.90 | 59.96 | 13 | 60 | 5 | -8 |
| **23** | 494550 | -9.04 | -46.05 | -9 | -46 | 1 | 10 |
| **25** | 494386 | -22.96 | -94.75 | -23 | -95 | -20 | 3 |
| **30** | 494232 | -1.09 | -10.07 | -1 | -10 | 5 | 6 |
| **31** | 494610 | 1.98 | 6.99 | 2 | 7 | 3 | 1 |
| **32** | 494730 | 2.98 | -0.00 | 3 | 0 | 15 | 12 |

Having verified the efficiency of the developed algorithm for inertial aided cycle slip detection and identification, the improvements on the positioning performance by the proposed algorithm are now discussed. As the GPS data was collected at a residential area and GPS signals from low elevation satellites were blocked frequently by trees and houses. As a result, a large number of cycle slips are expected. By applying the developed algorithm, there are 156 epochs in total at which the cycle slips were detected. The details are shown in Table 5.12. There is no cycle slips on the carrier phase measurements corresponding to PRN23, PRN31 and PRN32. The results are consistent with the fact that PRN23, PRN31 and PRN32 have higher elevations than other satellites and they can be continuously tracked during the entire test period.

**Table 5.15 Cycle slip detection results (Field Test #1)**

| **PRN** | **4** | **13** | **16** | **23** | **25** | **30** | **31** | **32** | **Total** |
|---|---|---|---|---|---|---|---|---|---|
| **No. of Epochs** | 54 | 33 | 12 | 0 | 43 | 14 | 0 | 0 | 156 |

Figure 5.21 shows the improvements on the position accuracy by using the proposed algorithm. The green and red lines represent the 3D position error with and without fixing the cycle slips, respectively. Table 5.13 summarizes the improvements on the position solutions. By fixing the cycle slips, the horizontal and vertical position accuracies are improved by 20.6% and 20.8%, respectively. Although large improvements are observed on position solutions, the improvements on velocity solutions are very small. This is

because that the velocity estimate highly relies on the Doppler measurements, which do not contain any ambiguity term and will not be affected by cycle slips.

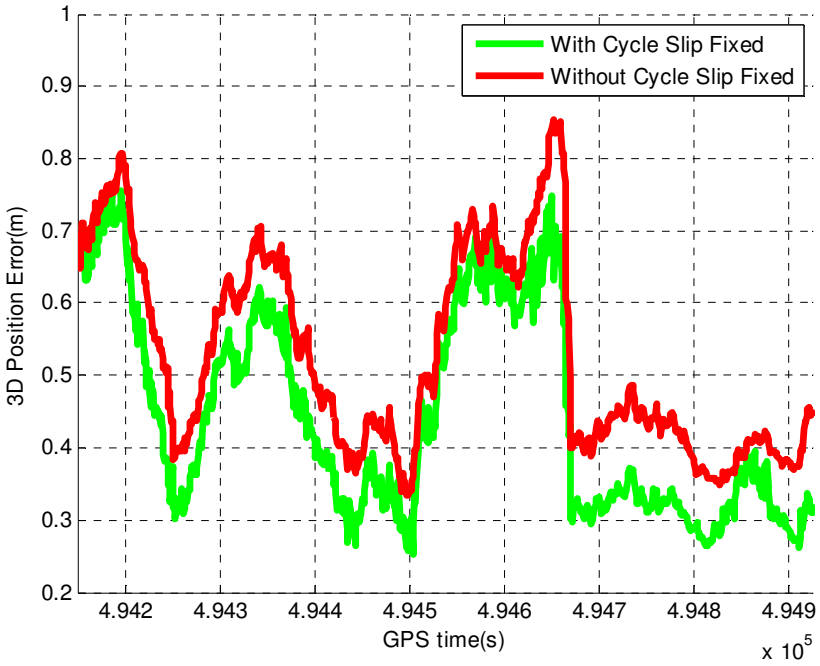


**Figure 5.21 Position accuracy improvements (Field Test #1)**

**Table 5.16 Summary of position accuracy improvements (Field Test #1)**

| | Lat (m) | Lon (m) | H (m) | Horizontal (m) | 3D (m) |
|---|---|---|---|---|---|
| **no CS fixed** | 0.11 | 0.32 | 0.48 | 0.34 | 0.59 |
| **CS fixed** | 0.08 | 0.26 | 0.38 | 0.27 | 0.47 |
| **Improvement** | 27.2% | 18.8% | 20.8% | 20.6% | 20.3% |

## 5.2 Field Test Two

This section evaluates the navigation performance of the developed integrated system by using a van test that carried out under a combined environment, which includes an urban canyon environment and a relatively open sky environment (Bancroft, 2009). Similar to Section 5.1, the description of the field test, which includes the GPS and IMU sensors used, the data collection environments and procedures, is firstly introduced. The analysis results obtained under the urban canyon environment and the relatively open sky environment are then discussed separately in Section 5.2.3 and Section 5.2.4.

### *5.2.1 Field Test Description*

The sensors used in the field test are the Crista IMU and the NovAtel SPAN$^{TM}$ system, which are already described in Section 5.1.1. The raw dual frequency GPS data, which includes pseudorange, carrier phase and Doppler measurements, was logged from the SPAN$^{TM}$ system with a data rate of 1 Hz. The raw HG1700 IMU data as well as the Crista IMU data were logged at a rate of 100 Hz. In order to generate a reference solution using a high precision DGPS/INS integrated system, a NovAtel OEM4 receiver was setup on the roof of a building with good satellite visibility at The University of Calgary to act as the base station. The dual-frequency GPS pseudorange, carrier phase and Doppler measurements were also logged at 1 Hz at the base station.

Data collection for the rover receiver installed on a vehicle began in a static mode under a relatively open sky environment. Then the vehicle was driven to the Calgary downtown area and then driven to the University region as shown in Figure 5.22 and the test lasted

for about 31 minutes (about 17 minutes in downtown area and 14 minutes in relatively open sky area). The velocity during the test ranged from zero to 70 km/h, with several stops due to traffic lights.

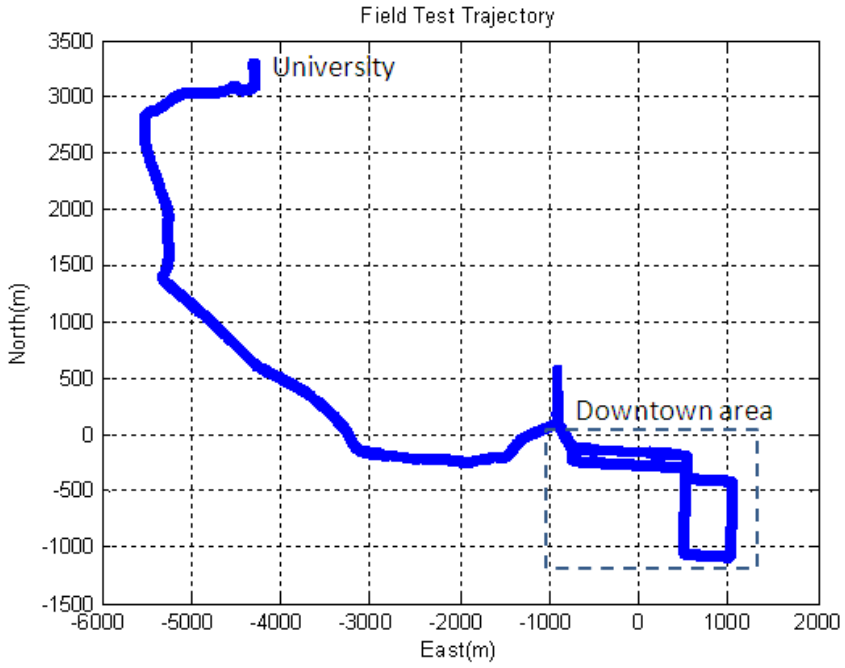


**Figure 5.22 Field test trajectory (Field Test #2)**

### *5.2.2 Reference Navigation Solution*

In order to facilitate a comparative analysis, a high precision DGPS/INS integrated system based on the NovAtel OEM4 receivers and HG1700 IMU is used. The collected GPS and INS data are processed by SAINT$^{TM}$ (Petovello 2003) with ambiguity resolution enabled to generate a precise reference solution. Figure 5.23 shows the standard deviation of the reference position solution. In the relatively open sky area, the fixed ambiguity navigation solution is obtained and the position standard deviation is maintained at less

than 4 cm. However the standard deviation is much larger in the urban canyon area due to the poor satellites availability. The largest horizontal and vertical standard deviations of the position solution are about 1 m and 1.8 m, respectively.

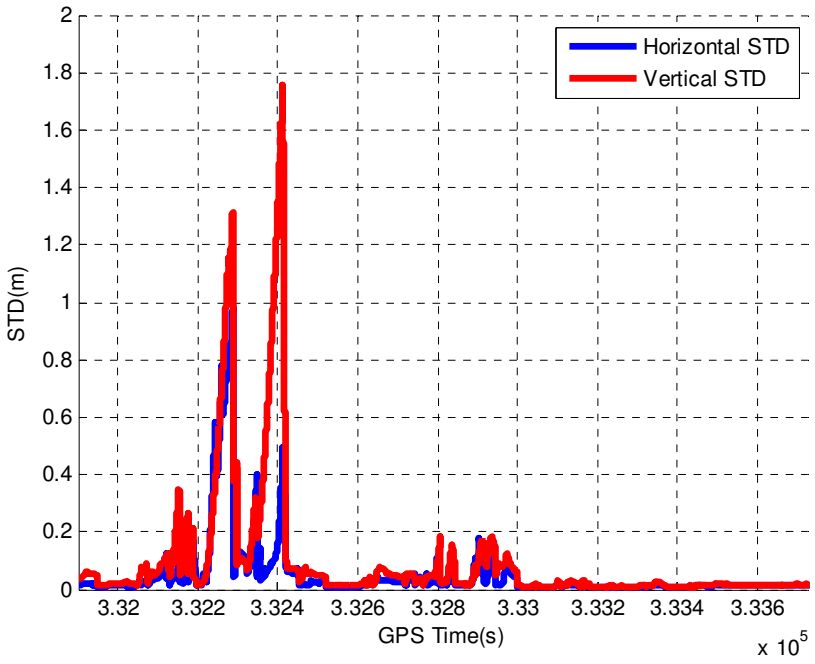


**Figure 5.23 STD of reference position solution (Field Test #2)**

Figure 5.24 shows the standard deviation of the reference velocity solution. In the relatively open sky area, the velocity standard deviation is maintained at better than 1 cm/s in most of the time. Similarly, larger standard deviations are observed in the urban canyons. The largest horizontal and vertical velocity standard deviations are about 4 cm/s and 5 cm/s, respectively.

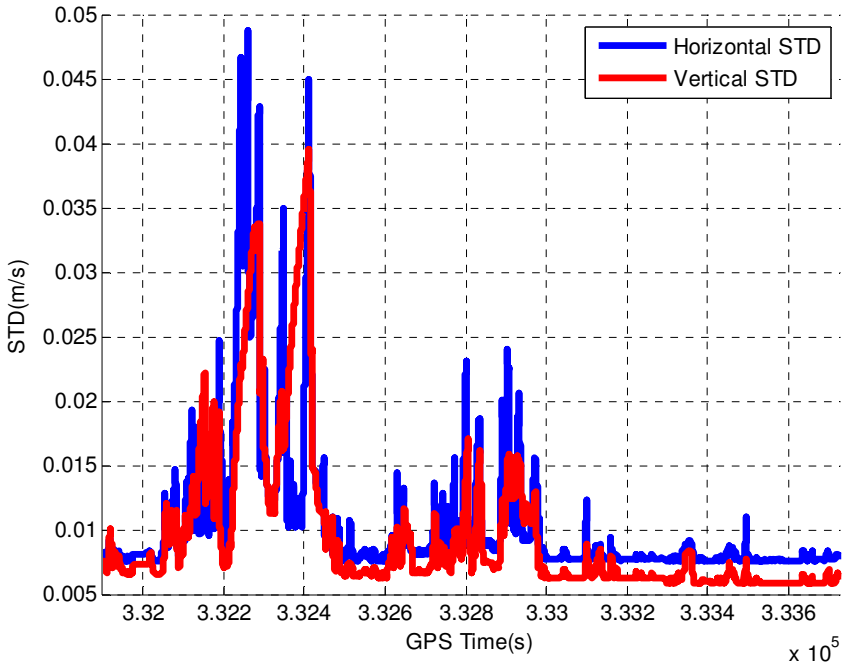


**Figure 5.24 STD of reference velocity solution (Field Test #2)**

### *5.2.3 Results in Downtown Area*

This section evaluates the navigation performance of the developed integrated system under realistic urban environments. There are a variety of medium or tall buildings in downtown area, which causes severe signal blockage. As a result, the satellite availability in the downtown area is pretty poor as shown in Figure 5.25. GPS outages occurred frequently and their duration varied from several to tens of seconds. The number of visible satellites changed from 0~3 at most times in the core area of downtown. Table 5.14 summarizes the satellites availability statistics during the time period spent in the downtown area.

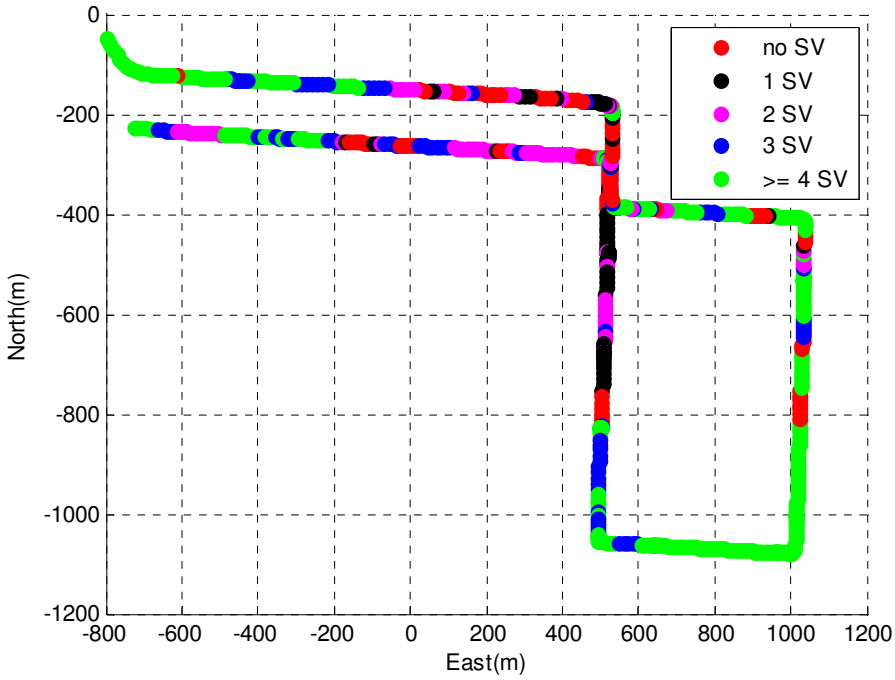


**Figure 5.25 GPS satellites availability in downtown area (Field Test #2)**

**Table 5.17 Statistics of satellites availability in downtown area (Field Test #2)**

| Number of Satellites Used in KF | Number of Epochs | Percentage (%) |
|---|---|---|
| **0** | 123 | 11.65 |
| **1** | 148 | 14.02 |
| **2** | 167 | 15.81 |
| **3** | 140 | 13.26 |
| **>= 4** | 478 | 45.27 |

Given in Table 5.15 are the position error statistics of both tightly and loosely coupled integrated systems. Due to the poor satellites availability in downtown area, the INS error cannot be continuously updated and corrected, and therefore accumulates. As a result, the positioning accuracy is typically poor, for instance, the horizontal position error can be as large as about 10 m. As demonstrated in the table, the tightly coupled system outperforms the loosely coupled system in the urban canyon environment because of the centralized processing in the tightly coupled system. The tightly coupled system uses the raw GPS measurements to update the INS error states whereas the loosely coupled system uses the calculated GPS position and velocities. During partial GPS outages the loosely coupled system solution still depends on GPS-only solutions, which are typically poor, thus degrading the quality of the updates available to the INS. The tightly coupled system relies on the raw GPS measurements, which offer updates to INS with better quality.

**Table 5.18 RMS position error results of PPP GPS/MEMS IMU in downtown area (Field Test #2)**

| | **Lat (m)** | **Lon (m)** | **Height (m)** | **Horizontal (m)** | **3D (m)** |
|---|---|---|---|---|---|
| **TC** | 5.48 | 6.31 | 7.19 | 8.35 | 11.02 |
| **LC** | 6.55 | 7.25 | 8.43 | 9.77 | 12.90 |

As discussed before, one remedy to improve the navigation performance of the integrated GPS/INS system under GPS outages is the non-holonomic constraints. The 2D velocity constraints are used during the GPS outages to improve the obtainable navigation

performance of the proposed integrated system. A statistical summary of the position errors from both the tightly and loosely coupled integrated systems with applying the 2D velocity constraints is given in Table 5.16. Improvements are observed on the position solutions in both the tightly and loosely coupled systems. For example, the horizontal position accuracy is improved by 41.4% and 35.4% in the tightly and loosely coupled integrated systems, respectively.

**Table 5.19 RMS position error results of PPP GPS/MEMS IMU with 2D velocity constraints in downtown area (Field Test #2)**

| | | Lat | Lon | Height | Horizontal | 3D |
|---|---|---|---|---|---|---|
| **TC** | **Position Error (m)** | 3.42 | 3.50 | 5.58 | 4.89 | 7.42 |
| | **Improvements (%)** | 37.6 | 44.5 | 22.4 | 41.4 | 32.6 |
| **LC** | **Position Error (m)** | 4.67 | 4.25 | 6.55 | 6.31 | 9.09 |
| | **Improvements (%)** | 28.7 | 41.4 | 22.3 | 35.4 | 29.5 |

Although improvements are obtained by using the 2D velocity constraints, the navigation performance of the proposed integrated PPP GPS/MEMS IMU system is still poor in urban areas, for instance, about 7 ~ 9 m accuracy for 3D position solution. For the applications requiring higher positioning accuracy under such conditions, more investigations are needed with the proposed integrated system.

### *5.2.4 Results in Relatively Open Sky Area*

The analysis results of the proposed integrated system under the relatively open sky environment in Field Test #2 are presented here.

#### 5.2.4.1 PPP GPS Results

Figure 5.26 and Figure 5.27 show the GPS satellites availability and the DOP values, respectively. More than 4 satellites are available throughout the time spent in the relatively open sky area. The HDOP and VDOP values are less than 2 in most of the time, although some relatively poor satellite geometry is observed at some epochs due to that the satellites with low elevations are frequently blocked by the buildings aside the road.

Provided in Figure 5.28 is the PPP GPS position error time series. As discussed in Section 5.1.3, a convergence time is needed for the position solution to achieve centimetre to decimetre level accuracy. However due to the van test in the relatively open sky area only lasts about 14 minutes, the backward processing is used to improve the obtainable accuracy. As shown in the figure, the latitude and longitude errors are well bounded within half metre in most of the time, while the height error is relatively large. A statistical summary of the position error is listed in Table 5.17. The horizontal and vertical position errors are 0.39 m and 0.55 m, respectively.

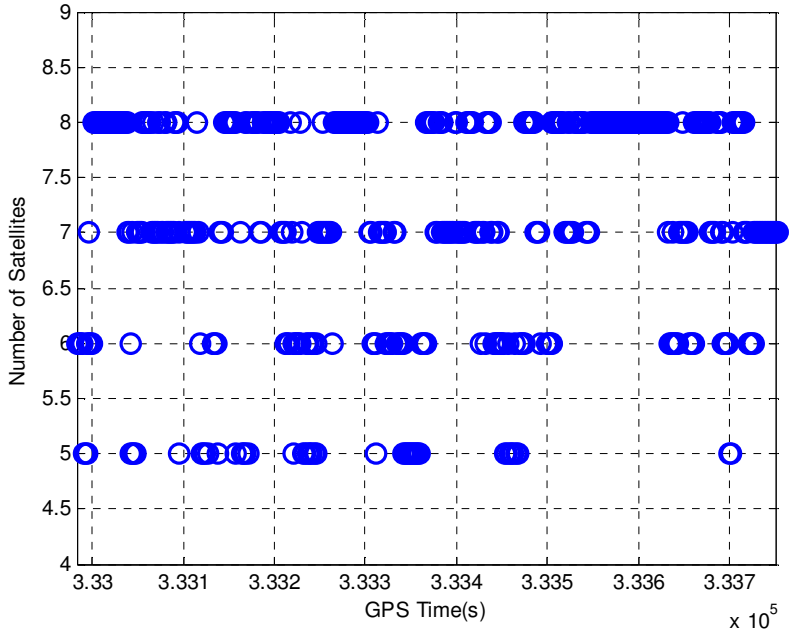


**Figure 5.26 GPS satellites availability in relatively open sky area (Field Test #2)**

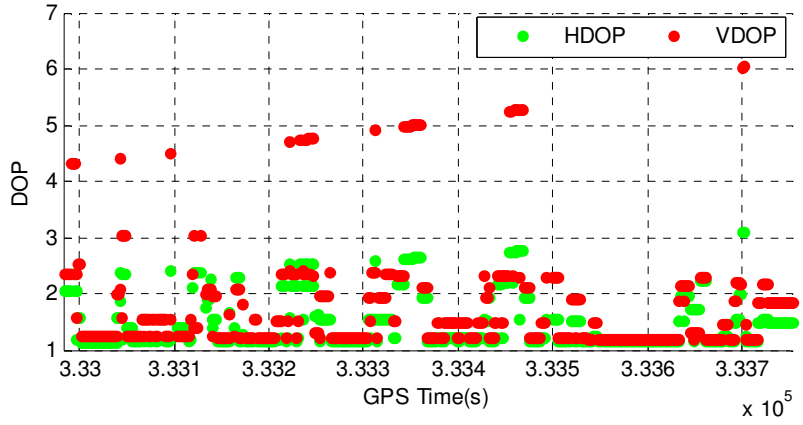


**Figure 5.27 Satellites geometry in relatively open sky area (Field Test #2)**

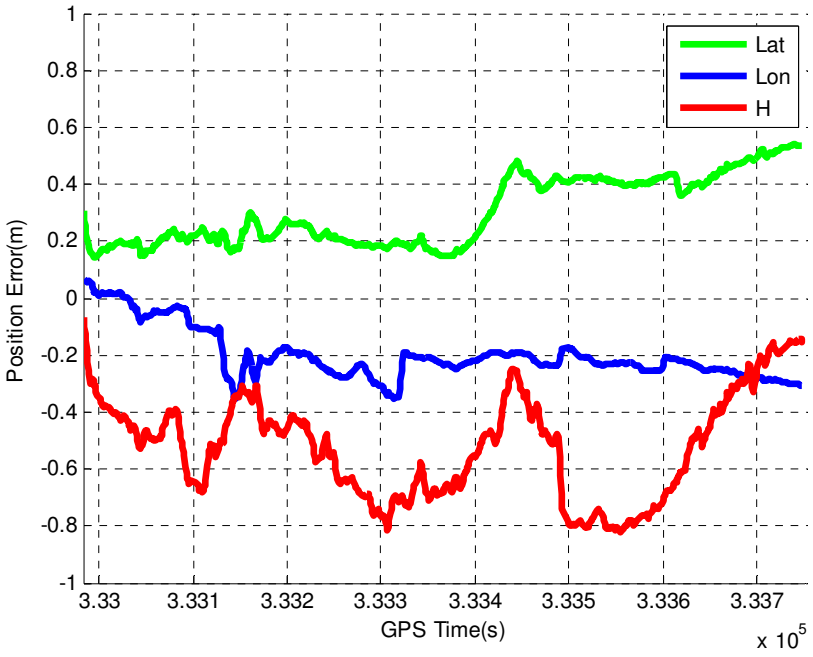


**Figure 5.28 PPP GPS position error in relatively open sky area (Field Test #2)**

Figure 5.29 shows the velocity error time series and Table 5.17 summarizes the velocity error statistics. The horizontal and vertical velocity errors are 3.3 cm/s and 5.6 cm/s, respectively. Since the velocity estimate mainly relies on the Doppler measurements, the velocity estimation does not require a convergence time. Based on the PPP GPS results, similar results are expected from the proposed integrated PPP GPS/MEMS IMU system.

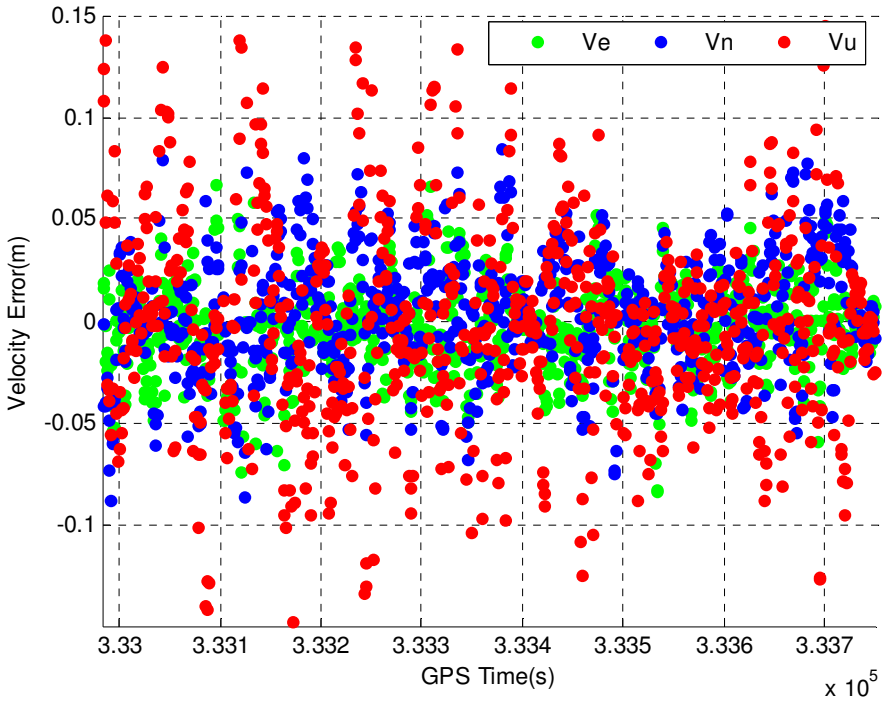


**Figure 5.29 PPP GPS velocity error in relatively open sky area (Field Test #2)**

**Table 5.20 RMS position/velocity error results of PPP GPS in relatively open sky area (Field Fest #2)**

| **Position Error (m)** | | | | |
|---|---|---|---|---|
| **Lat** | **Lon** | **H** | **Horizontal** | **3D** |
| 0.33 | 0.22 | 0.55 | 0.39 | 0.67 |
| **Velocity Error (m/s)** | | | | |
| **Vn** | **Ve** | **Vu** | **Horizontal** | **3D** |
| 0.027 | 0.019 | 0.056 | 0.033 | 0.065 |

#### 5.2.4.2 Integrated PPP GPS/MEMS IMU System Results

This section discusses the results obtained from both the tightly and loosely coupled integrated PPP GPS/MEMS IMU systems under the relatively open sky environments in Field Test #2. All GPS pseudorange, carrier phase and Doppler measurements are used in data processing and the results are obtained with the cycle slip detection and identification enabled. A backward processing method is also used due to the short duration of dataset. Similar to Section 5.1.4, the position accuracy is given first, then followed by the velocity and attitude accuracies.

##### Position Accuracy

Figure 5.30 shows the position error time series of the tightly coupled integrated system. The latitude and longitude errors are well bounded within 0.4 m, while the height error is less than 0.6 m in majority of the time. Listed in Table 5.18 are the position error statistics of both the tightly and loosely coupled integrated systems. The horizontal and vertical position errors for the tightly coupled system are 0.31 m and 0.42 m, respectively, and similar results are obtained in the loosely coupled system.

Similarly the tightly coupled integrated system slightly outperforms the loosely coupled system; the reason has been discussed in Section 5.1. Improvements on positioning accuracy raised by the proposed algorithm of inertial aided cycle slip detection and identification algorithm can still be observed. The details will be discussed later.

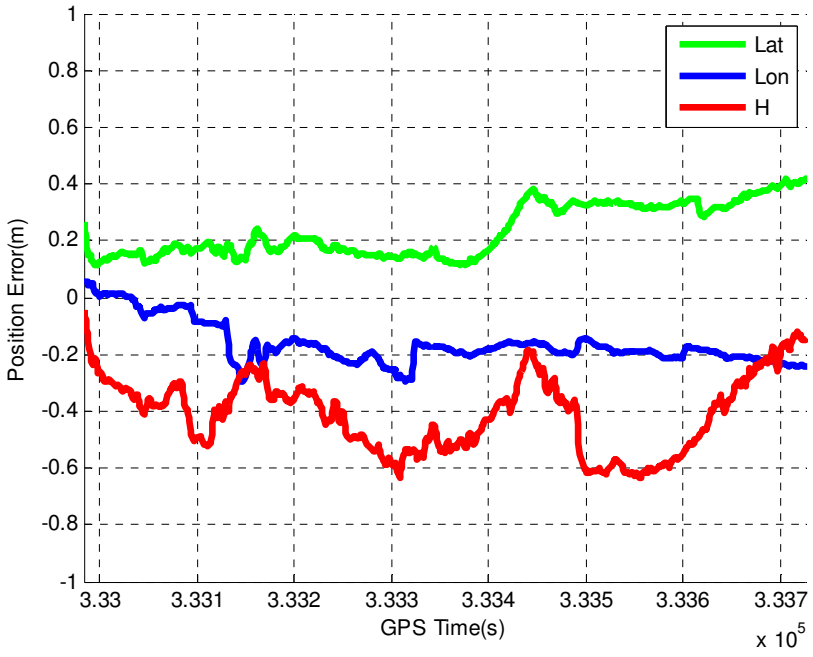


**Figure 5.30 Tightly coupled PPP GPS/MEMS IMU position error in relatively open sky area (Field Test #2)**

**Table 5.21 RMS position error results of PPP GPS/MEMS IMU in relatively open sky area (Field Test #2)**

| RMS | Lat (m) | Lon (m) | Height (m) | Horizontal (m) | 3D (m) |
|---|---|---|---|---|---|
| **TC** | 0.26 | 0.18 | 0.42 | 0.31 | 0.53 |
| **LC** | 0.28 | 0.18 | 0.44 | 0.33 | 0.55 |

Velocity Accuracy

Figure 5.31 presents the velocity error time series of the tightly coupled system. The velocity errors in the east and the north directions are well bounded within 5 cm/s in most of the time. A statistical summary of the velocity errors in both the tightly and loosely

coupled integrated systems is listed in Table 5.18. The horizontal and vertical velocity errors for the tightly coupled integrated system are 2.9 cm/s and 5.3 cm/s, respectively. Similar results are obtained in the loosely coupled integrated system.

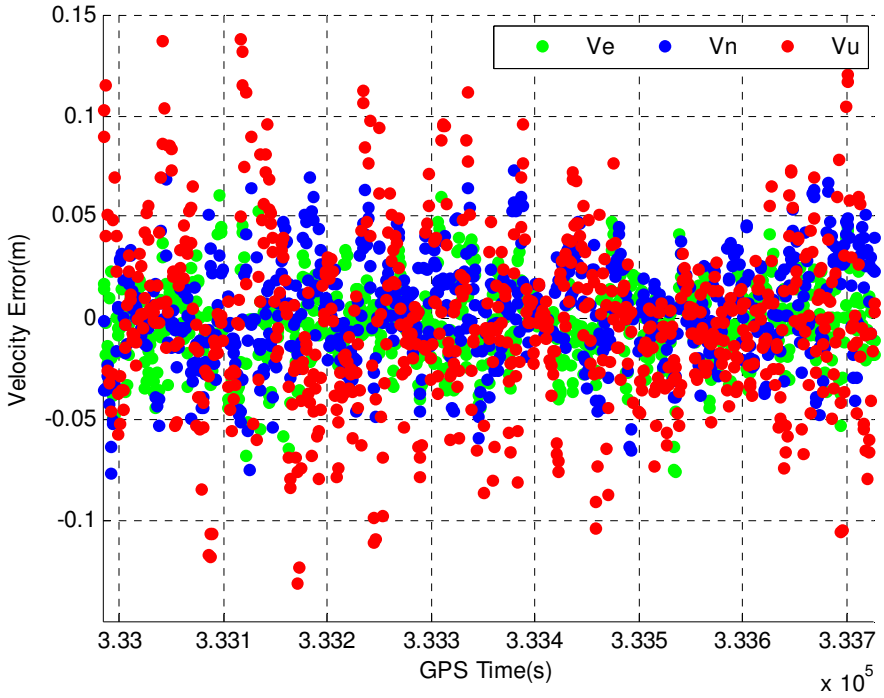


**Figure 5.31 Tightly coupled PPP GPS/MEMS IMU velocity error in relatively open sky area (Field test #2)**

**Table 5.22 RMS velocity error results of PPP GPS/MEMS IMU in relatively open sky area (Field Test #2)**

| RMS | Vn (m/s) | Ve (m/s) | Vu (m/s) | Horizontal (m/s) | 3D (m/s) |
|---|---|---|---|---|---|
| **TC** | 0.023 | 0.018 | 0.053 | 0.029 | 0.061 |
| **LC** | 0.025 | 0.019 | 0.054 | 0.031 | 0.062 |

Due to the short duration of the dataset, the ambiguity did not completely converge to its real value. As a result, the proposed integrated system was not able to achieve centimetre to decimetre level positioning accuracy. With longer duration of dataset, the position accuracy is expected to be further improved. Since no convergence time is needed for velocity estimation, the velocity solution accuracy is at centimetre per second level.

Attitude Accuracy

The attitude error time series of the tightly coupled integrated system is plotted in Figure 5.32. As discussed before, the significant sensor errors and poor observability result in relatively poor accuracies for attitude estimates, especially for the azimuth estimate. As shown in the figure, the pitch and roll errors are well below 1 degree in most times, while the azimuth error can be as large as about 3 degrees at some epochs.

Table 5.20 presents the attitude error statistics of both the tightly and loosely coupled integrated systems. Similar attitude accuracies are obtained in both systems. The pitch and roll errors are about 0.4 degree and the azimuth error is about 1.5 degrees.

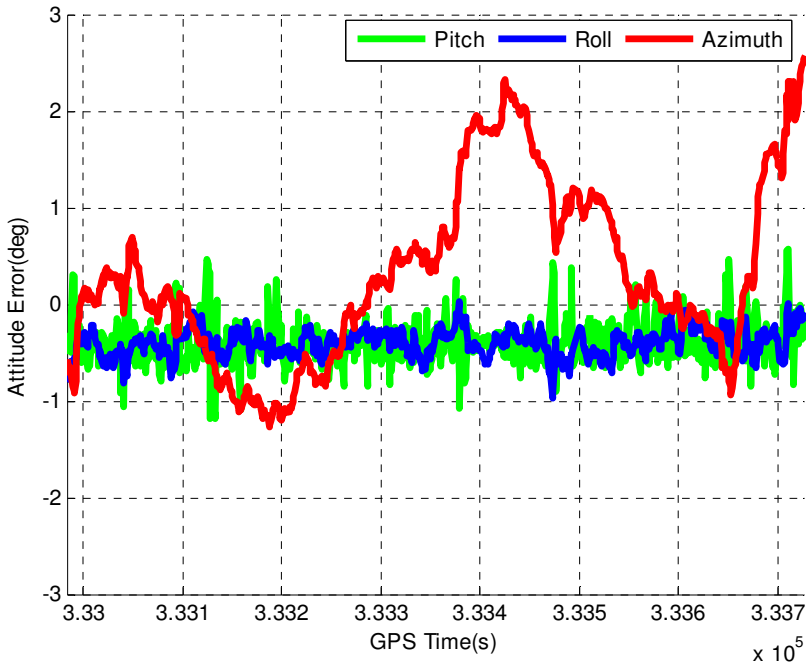


**Figure 5.32 Tightly coupled PPP GPS/MEMS IMU attitude error in relatively open sky area (Field Test #2)**

**Table 5.23 RMS attitude error results of PPP GPS/MEMS IMU in relatively open sky area (Field Test #2)**

| RMS | Pitch (degree) | Roll (degree) | Azimuth (degree) |
|---|---|---|---|
| **TC** | 0.45 | 0.42 | 1.47 |
| **LC** | 0.41 | 0.44 | 1.52 |

5.2.4.3 Results with 2D Velocity Constraints

As discussed before, the 2D velocity constraints are able to improve the attitude accuracies. Figure 5.33 shows the tightly coupled system attitude error time series after using the constraints. The improvements on the pitch and roll estimates are relatively

small comparing to the major improvements on the azimuth estimate. Table 5.21 summarizes the tightly coupled system attitude error statistics after using the 2D velocity constraints. The pitch and roll accuracies are improved by 6.7% and 7.1%, respectively, and the azimuth accuracy is improved by about 48%.

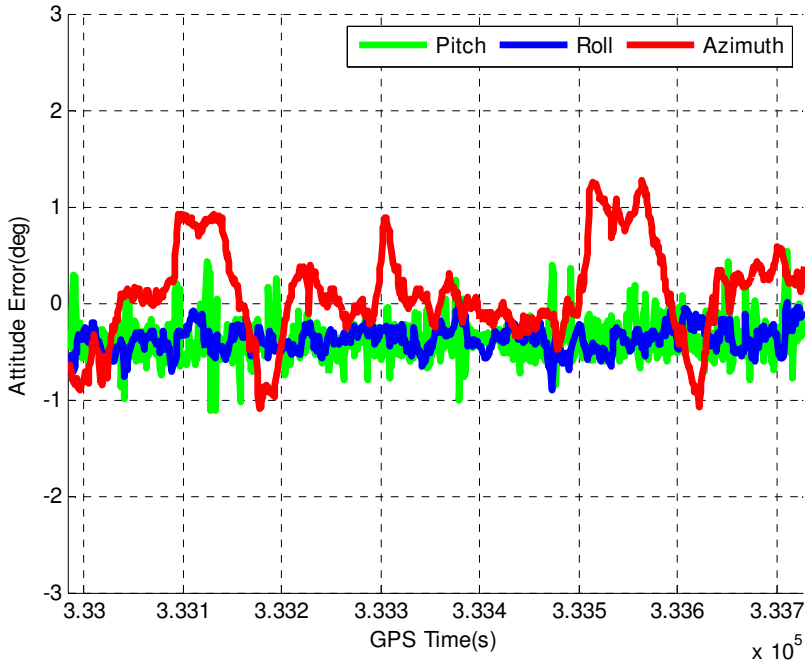


**Figure 5.33 Tightly coupled PPP GPS/MEMS IMU attitude error with 2D velocity constraints in relatively open sky area (Field Test #2)**

**Table 5.24 RMS attitude error results of tightly coupled PPP GPS/MEMS IMU with 2D velocity constraints in relatively open sky area (Field Test #2)**

| | **Pitch (degree)** | **Roll (degree)** | **Azimuth (degree)** |
|---|---|---|---|
| **No Constraints** | 0.45 | 0.42 | 1.47 |
| **2D Velocity** | 0.42 | 0.39 | 0.76 |
| **Improvements** | 6.7% | 7.1% | 48.3% |

Summarized in Table 5.22 are the improvements on the attitude accuracies in the loosely coupled integrated system after using the 2D velocity constraints. The pitch and roll accuracies are improved by 7.3% and 9.0%, respectively, and azimuth accuracy is improved by 46%.

**Table 5.25 RMS attitude error results of loosely coupled PPP GPS/MEMS IMU with 2D velocity constraints in relatively open sky area (Field test #2)**

| | **Pitch (degree)** | **Roll (degree)** | **Azimuth (degree)** |
|---|---|---|---|
| **No Constraints** | 0.41 | 0.44 | 1.52 |
| **2D Velocity** | 0.38 | 0.40 | 0.81 |
| **Improvements** | 7.3% | 9.0% | 46.7% |

5.2.4.4 Results with GPS outages

This section evaluates the ability of the MEMS IMU to bridge the GPS outages. Similar to the Field Test #1, GPS outages are simulated by rejecting the satellites in data processing. The results under complete GPS outages are firstly presented and then followed by the results under partial GPS outages. The 2D velocity constraints are used during the GPS outages to investigate the obtainable performance of the proposed integrated system. The GPS data and Crista IMU data are processed with the tightly coupled integrated system.

Results with Complete GPS Outages

A total of five complete GPS outages are simulated, which are selected as 2 over high dynamic periods, 2 over moderate dynamic periods and 1 over low dynamic period. The outages last for 30 seconds and it is given at least 70 seconds for the integration filter to re-converge before the next outage.

Figure 5.34 shows the horizontal position error during the five complete GPS outages. As expected the position error is accumulated over time when GPS update is absent. The accumulated INS error primarily depends on the grade of IMU used and the time span of the GPS outages. For all GPS outages, the maximum horizontal position errors range from 23 m to 58m.

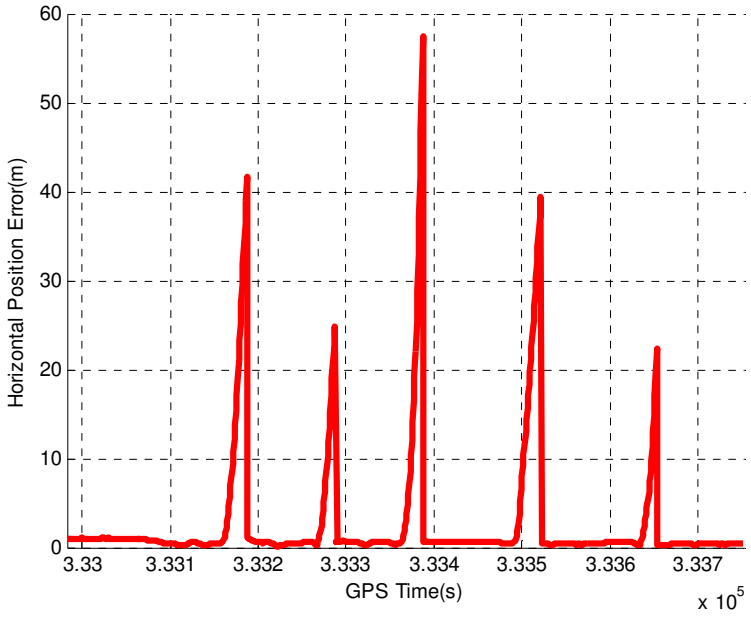


**Figure 5.34 Horizontal position error of PPP GPS/MEMS IMU in relatively open sky area under complete GPS outages (Field Test #2)**

Shown in Figure 5.35 is the horizontal position error during complete GPS outages with applying the 2D velocity constraints. The position accuracy is improved significantly after using the 2D velocity constraints. The maximum horizontal position errors are limited to be less than 15 m for all simulated GPS outages.

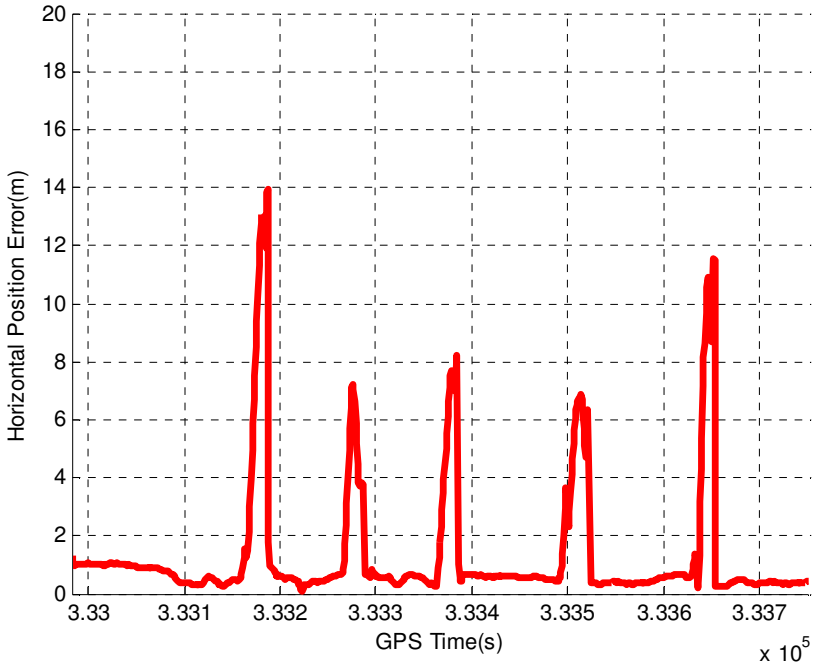


**Figure 5.35 Horizontal position error of PPP GPS/MEMS IMU with 2D velocity constraints in relatively open sky area under complete GPS outages (Field Test #2)**

The RMS position error during complete GPS outages is calculated and provided in Figure 5.36. The green and red solid lines represent the RMS position error with and without applying the 2D velocity constraints, respectively. The RMS position error starts to grow right after the GPS outage occurs and it is accumulated to 39 m within 30

seconds. By applying the constraints, the maximum RMS horizontal position error is reduced to about 10 m.

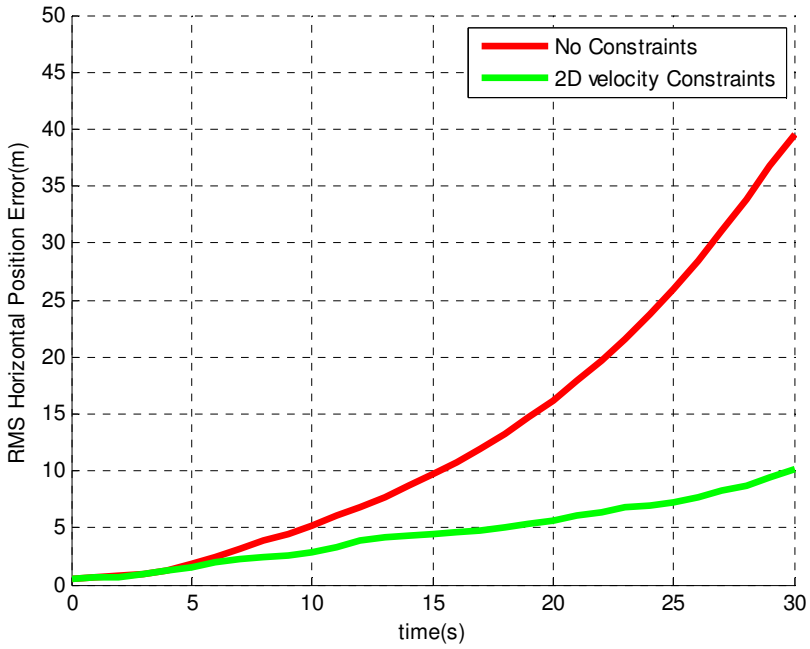


**Figure 5.36 RMS horizontal position error of PPP GPS/MEMS IMU in relatively open sky area during complete GPS outages (Field Test #2)**

Results with Partial GPS Outages

The five time periods used to simulate complete GPS outages are adopted again to simulate the partial GPS outages, during which only 2 or 3 satellites are available. As introduced in Section 5.1.6, the partial GPS outages are simulated by raising the satellite elevation mask during the certain time periods. Figure 5.37 presents the computed RMS position error for all the partial GPS outages.

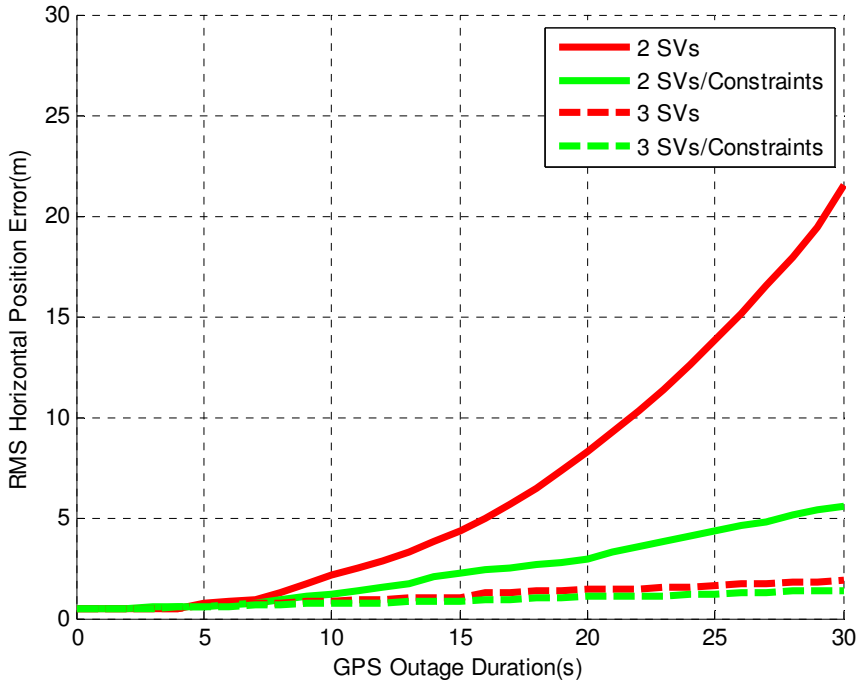


**Figure 5.37 RMS horizontal position error of PPP GPS/MEMS IMU in relatively open sky area during partial GPS outages (Field Test #2)**

When 2 GPS satellites are available, the INS error still accumulates, although the rate of accumulation is damped. It accumulates to about 22 m over 30 seconds. After applying the 2D velocity constraints, the maximum RMS position error is reduced to about 6 m. With 3 GPS satellites available, the maximum RMS position error is reduced to about 2 m, and it is further reduced to about 1.5 m when the constraints are used.

5.2.4.5 Inertial Aided Cycle Slip Detection and Identification Results

This section presents the results of the inertial aided cycle slip detection and identification. Similar to Section 5.1.7, the calculated decision variables are firstly analyzed, and a simulated cycle slip scenario is used to evaluate the efficiency of the developed algorithm; then the improvements on positioning accuracy are discussed at last.

Shown in Figure 5.38 and Figure 5.39 are the decision variables for the GPS satellites. The blue dot and red dot represent the computed decision variable based on the widelane phase combination and the extra-widelane phase combination, respectively. The GPS satellite PRN12 has the highest elevation and is used as the base satellite to compute the decision variables. To provide a clear view of the values of the decision variables, the epochs which have cycle slips have been removed in both Figure 5.38 and Figure 5.39.

As shown in the figures, the decision variables are Gaussian distributed and centered at zero. The PRN9, PRN17 and PRN29 have the lower elevations that range from 7 to 19 degrees and they can only be tracked in certain periods of time. Due to the low elevations, the decision variables for PRN9, PRN17 and PRN29 are much noisier than that of the rest satellites.

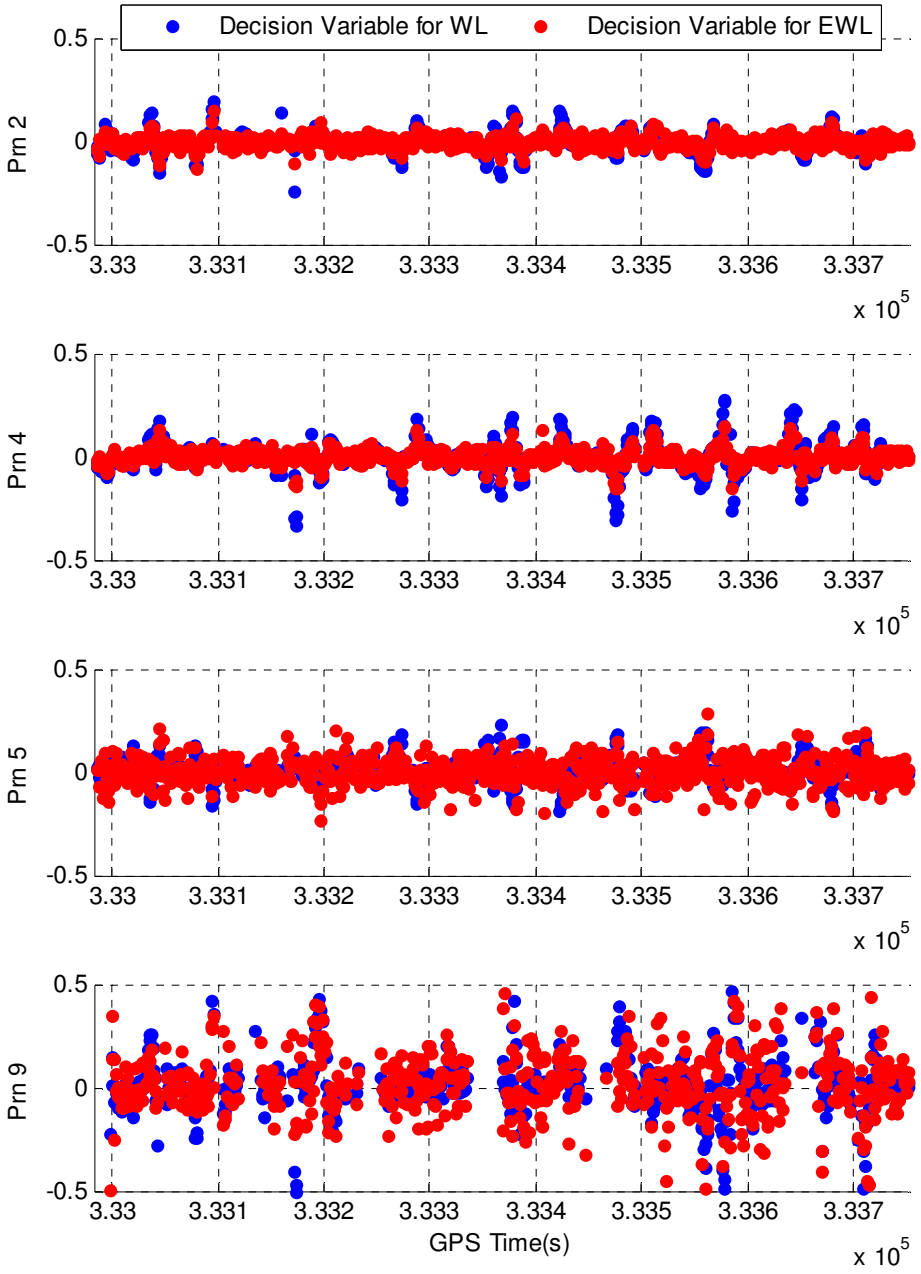


**Figure 5.38 Decision variables for PRN2, PRN4, PRN5 and PRN9 in relatively open sky area (Field Test #2)**

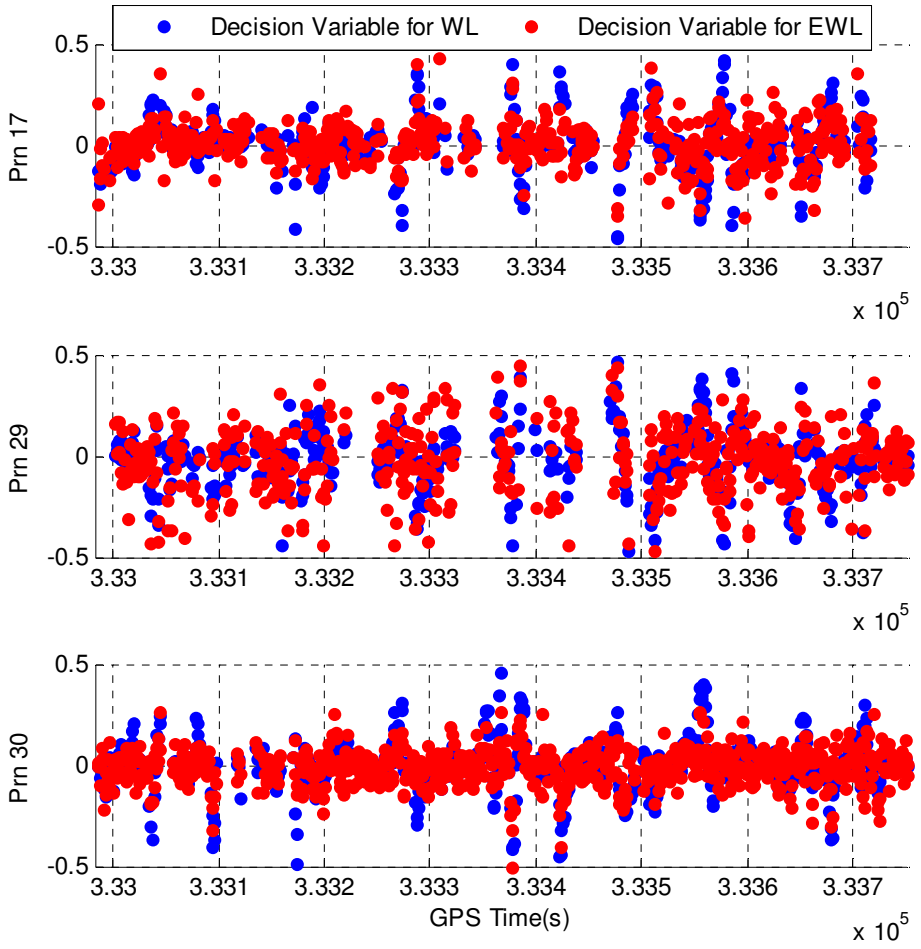


**Figure 5.39 Decision variables for PRN17, PRN29 and PRN30 in relatively open sky area (Field Test #2)**

Listed in Table 5.23 are the estimated standard deviations of the decision variables for all satellites in view. It can be seen that the standard deviations for all decision variables are less than 0.2 cycles.

**Table 5.26 STD of decision variables in relatively open sky area (Field Test #2)**

| PRN | 2 | 4 | 5 | 9 | 17 | 29 | 30 |
|---|---|---|---|---|---|---|---|
| **DV for WL (cycle)** | 0.04 | 0.06 | 0.05 | 0.14 | 0.12 | 0.15 | 0.11 |
| **DV for EWL (cycle)** | 0.03 | 0.04 | 0.06 | 0.16 | 0.10 | 0.19 | 0.09 |

Shown in Table 5.24 is the simulated cycle slip scenario. The cycle slips are simulated on L1 and L2 frequencies for all satellites in view with different numbers.

**Table 5.27 Simulated cycle slip scenario II**

| Satellite PRN | GPS time (s) | Cycle Slips on L1 (cycle) | Cycle Slip on L2 (cycle) |
|---|---|---|---|
| **2** | 333000 | 1 | 0 |
| **4** | 333123 | 0 | -1 |
| **5** | 333211 | 5 | -8 |
| **9** | 333311 | 1 | 10 |
| **17** | 333426 | -20 | 3 |
| **29** | 333527 | 5 | 6 |
| **30** | 333688 | 3 | 1 |

The threshold for both cycle slip detection and identification is selected as 0.5 cycles in this study, and the testing probabilities computed based on the threshold and the estimated standard deviations of decision variables are given in Table 5.25.

**Table 5.28 Testing probabilities in relatively open sky area (Field Test #2)**

| | **Widelane Phase Combination** | | | | **Extra-Widelane Phase Combination** | | | |
|---|---|---|---|---|---|---|---|---|
| **PRN** | FA | MD | RD | FD | FA | MD | RD | FD |
| **2** | 0 | 0 | 1 | 0 | 0 | 0 | 1 | 0 |
| **4** | 0 | 0 | 1 | 0 | 0 | 0 | 1 | 0 |
| **5** | 0 | 0 | 1 | 0 | 0 | 0 | 1 | 0 |
| **9** | 9e-7 | 4e-7 | 1-9e-7 | 9e-7 | 2e-5 | 1e-5 | 1-2e-5 | 2e-5 |
| **17** | 7e-9 | 4e-9 | 1-8e-9 | 8e-9 | 0 | 0 | 1 | 0 |
| **29** | 5e-6 | 2e-6 | 1-5e-6 | 5e-6 | 4e-4 | 2e-4 | 1-4e-4 | 4e-4 |
| **30** | 3e-10 | 1e-10 | 1-3e-10 | 3e-10 | 0 | 0 | 1 | 0 |

As discussed before, with the cycle slips, the normal distribution characteristic of the decision variable is deteriorated. This can be seen in Figure 5.40 and Figure 5.41 which show the decision variables with the cycle slips. Some large values of decision variables are observed at some epochs and they indicate that the cycle slips occurred.

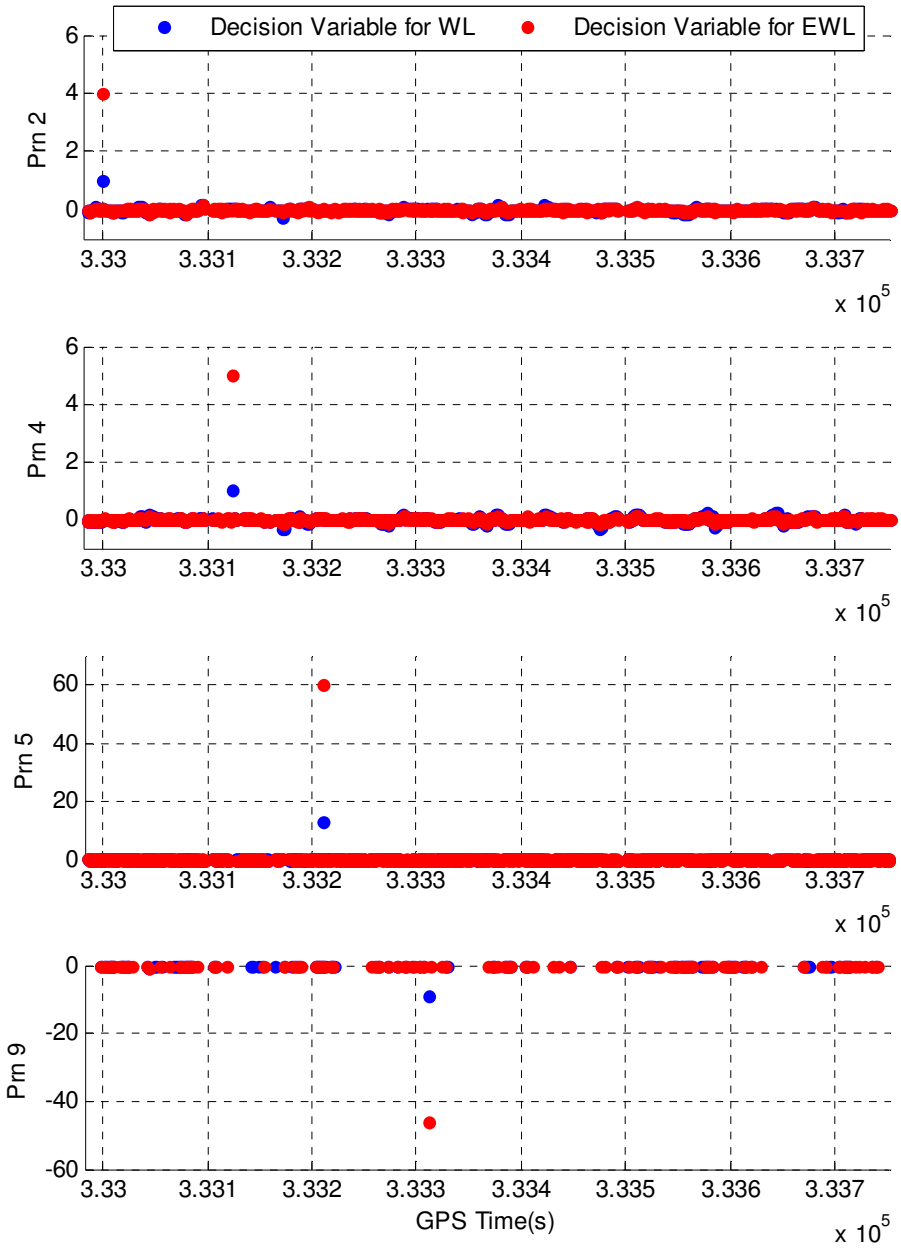


**Figure 5.40 Decision variables for PRN2, PRN4, PRN5 and PRN9 with simulated cycle slips in relatively open sky area (Field Test #2)**

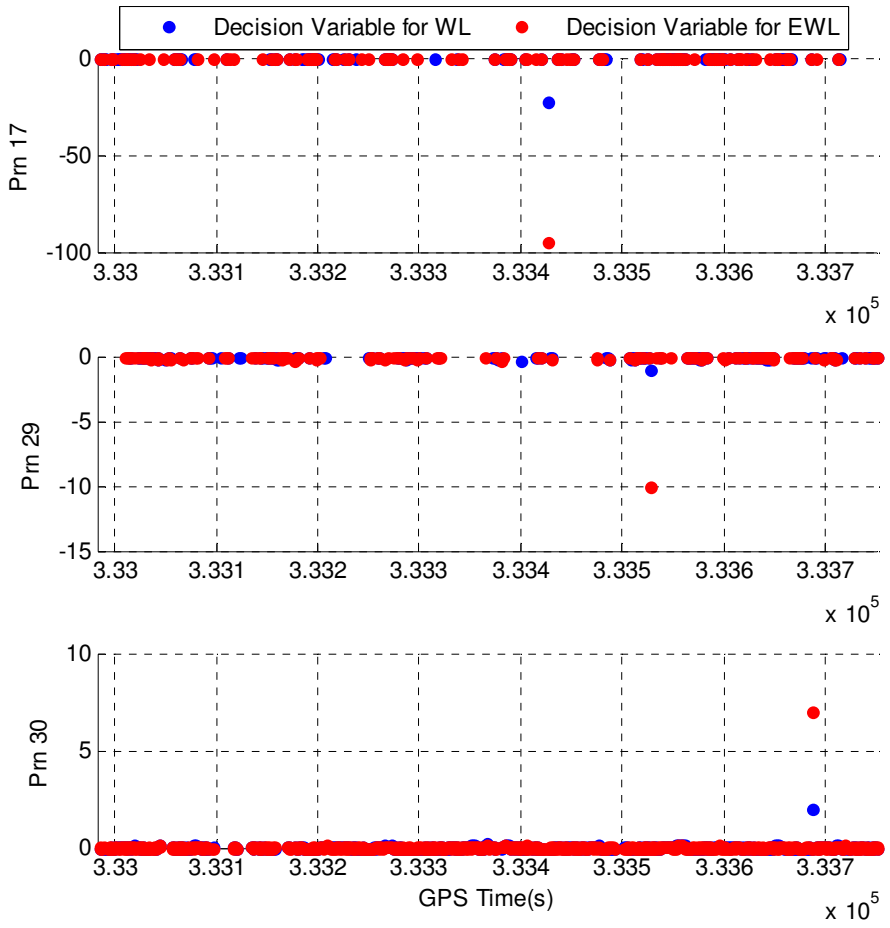


**Figure 5.41 Decision variables for PRN17, PRN29 and PRN30 with simulated cycle slips in relatively open sky area (Field Test #2)**

Table 5.26 lists the detected and identified cycle slips by using the proposed algorithm. Based on the identified WL phase and EWL phase cycle slips, the cycle slips on L1 and L2 frequencies are determined. Comparing to the simulated cycle slip scenario, all simulated cycle slips are correctly identified.

**Table 5.29 Identified cycle slips in simulated cycle slip scenario II**

| PRN | GPS time (s) | DV/WL (cycle) | DV/EWL (cycle) | CS/WL (cycle) | CS/EWL (cycle) | CS/L1 (cycle) | CS/L2 (cycle) |
|---|---|---|---|---|---|---|---|
| **2** | 333000 | 0.98 | 4.00 | 1 | 4 | 1 | 0 |
| **4** | 333123 | 1.04 | 5.00 | 1 | 5 | 0 | -1 |
| **5** | 333211 | 13.02 | 60.08 | 13 | 60 | 5 | -8 |
| **9** | 333311 | -9.02 | -45.97 | -9 | -46 | 1 | 10 |
| **17** | 333426 | -22.83 | -94.90 | -23 | -95 | -20 | 3 |
| **29** | 333527 | -1.02 | -10.07 | -1 | -10 | 5 | 6 |
| **30** | 333688 | 1.99 | 6.99 | 2 | 7 | 3 | 1 |

Having evaluated the efficiency of the proposed algorithm by using simulated cycle slip scenario, the improvements on the positioning accuracy are now discussed. The collected GPS and Crista IMU data are processed with the tightly coupled integrated system. Table 5.27 presents the obtained cycle slip detection results.

**Table 5.30 Cycle slips detection results in relatively open sky area (Field Test #2)**

| PRN | 2 | 4 | 5 | 9 | 17 | 29 | 30 | Total |
|---|---|---|---|---|---|---|---|---|
| **No. of Epochs** | 2 | 3 | 3 | 26 | 28 | 33 | 7 | 102 |

Since the GPS signals from the satellites with low elevations are frequently blocked by the buildings aside the road, a large number of cycle slips is expected. There are 102 epochs in total that cycle slips were detected. PRN2, PRN4 and PRN5 have higher elevations and very few cycle slips are detected on these satellites, however lots of cycle slips are detected on PRN9, PRN17 and PRN29 due to their low elevations.

Figure 5.42 shows the improvements on the position solution. As expected, improvements on position accuracy are observed after successfully fixing the cycle slips by using the proposed algorithm. Because the velocity estimate highly relies on the Doppler measurements, the improvements on velocity accuracy are very small.

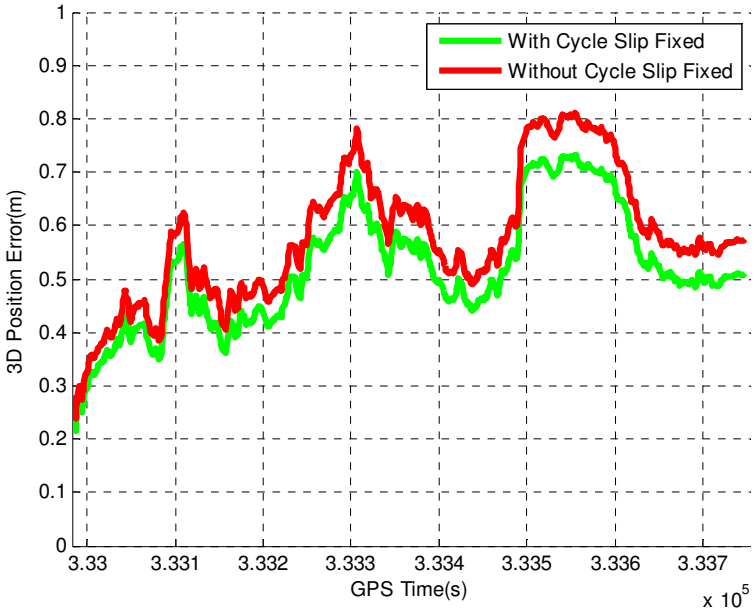


**Figure 5.42 Position accuracy improvements in relatively open sky area (Field Test #2)**

Table 5.28 summarizes the improvements on the position accuracy. By fixing the cycle slips, the latitude and longitude accuracies are improved by 18.8% and 18.2%, respectively, and the height accuracy is improved by 22.2%.

**Table 5.31 Summary of position accuracy improvements in relatively open sky area (Field Test #2)**

| | Lat (m) | Lon (m) | H (m) | Horizontal (m) | 3D (m) |
|---|---|---|---|---|---|
| **no CS fixed** | 0.32 | 0.22 | 0.54 | 0.38 | 0.66 |
| **CS fixed** | 0.26 | 0.18 | 0.42 | 0.31 | 0.53 |
| **Improvement** | 18.8% | 18.2% | 22.2% | 18.4% | 19.7% |

## 5.3 Results Summary

In this chapter, the proposed integrated PPP GPS/MEMS IMU system has been tested and analyzed with relatively open sky area data and urban area data.

### *5.3.1 Relatively Open Sky Area Results Summary*

In the relatively open sky area, although the developed integrated system does not achieve the centimetre to decimetre positioning accuracy due to the short duration of the field tests, the obtained results are still promising. In both field tests, the horizontal and vertical position accuracies are about 0.3 m and 0.4 m, respectively, and the velocity accuracy is centimetre to sub-decimetre per second. The attitude accuracies are relatively poor comparing to the tactical grade IMU due to the large sensor errors of MEMS IMU. The pitch and roll accuracies are about 0.5 degree and azimuth accuracy is about 1.5

degrees without applying any constraints. The results also indicate that the tightly coupled system slightly outperforms the loosely coupled system in the relatively open sky environments. This is because that GPS and INS information are more rigorously modeled in the tightly coupled system than a loosely coupled system.

By applying the 2D velocity constraints, the observability of the attitude estimates are improved, which leads to some improvements on the attitude accuracies. The pitch and roll accuracies are improved by 5%~9%, and the azimuth accuracy is improved by 43%~48%.

Due to the absence of the GPS updates, the INS error accumulates rapidly during complete GPS outages. In the two field tests, the maximum RMS horizontal position error reaches about 38~40 m during the 30-second complete GPS outages. By applying the 2D velocity constraints, the maximum RMS horizontal position error is reduced to 10~11 m. Under the 30-second partial GPS outages with 2 satellites available, the INS error still accumulates, although the rate of accumulation is damped. This slight improvement can be attributed to the updates from the 2 available GPS satellites. The obtained results indicate that the maximum RMS horizontal position error reaches 20~22 m and it is reduced to 5~6 m after using the 2D velocity constraints. When 3 satellites are available, the positioning performance is significantly improved, although the INS error still accumulates at a much slower rate. The maximum RMS horizontal position error is about 2 m during the 30-second partial GPS outage and it is reduced to about 1.5 m by applying the constraints.

The developed algorithm of inertial aided cycle slip detection and identification is able to detect and identify every single cycle slips. The computed decision variable is Gaussian distributed with a mean value of zero if it is free of cycle slips. By fixing the identified cycle slips in the carrier phase measurements, improvements are observed on positioning accuracy. In two field tests, the horizontal and vertical position accuracies are improved by about 18% - 22%.

### *5.3.2 Urban Area Results Summary*

As we know the GPS satellites availability is typically poor in urban canyons, the complete and partial GPS outages are frequently encountered in such conditions. Even though the MEMS IMU is able to bridge the GPS outages, the developed PPP GPS/MEMS IMU system offers the horizontal and vertical position accuracies at 8~10 m and 7~9 m, respectively. Even with the aiding from the 2D velocity constraints, the horizontal and vertical position accuracies can only achieve at 5~6 m and 6~7 m, respectively. For the applications requiring higher positioning performance, more investigations are need with the proposed integrated system.

# Chapter Six: Conclusions and Recommendations

This thesis is to investigate the integration of Precise Point Positioning GPS and low cost MEMS IMU. Both loosely and tightly coupled Kalman filters are developed to derive the optimal navigation solution. A closed loop approach is used to compensate the INS errors. Considering the high magnitudes of turn on biases and scale factors in the accelerometers and gyroscopes of the MEMS IMU, a 27-error state vector for INS errors is used in the filter. The 2D velocity constraints are incorporated to the integrated PPP GPS/MEMS IMU system to improve the attitude accuracies and to mitigate the INS error accumulation during GPS outages. With the aiding from the low cost MEMS IMU, a cycle slip detection and identification algorithm is developed to help the quality control in the PPP GPS. The proposed integrated system is tested and evaluated by two van tests, which are carried out in various GPS conditions (relatively open sky areas and urban areas). The equipments used in this study are the NovAtel OEM4 GPS receivers, the Crista MEMS IMU from the Cloud Cap Technology Inc and the tactical grade HG1700 IMU. The reference solution is obtained from a high precision integrated DGPS/INS system based on the NovAtel OEM4 receivers and the tactical grade HG1700 IMU.

The following sections outline the major conclusions drawn from this research and the recommendations for future improvements.

## 6.1 Conclusions

The developed PPP GPS/MEMS IMU integrated system offers some promising results, although only a single dual-frequency GPS receiver is used. In PPP GPS, since the ambiguity terms are estimated as float numbers and they require a time period to converge to their true values, the position solution requires a convergence time to achieve centimetre to decimetre level accuracy. Normally the required convergence time is 20-40 minutes. Since the two field tests only last for 16 min and 14 min, respectively, the ambiguities in the carrier phase measurements cannot be completely converged, a backward processing method is used to improve the obtainable navigation performance. The results indicate that the proposed integrated system provide the horizontal and the vertical position accuracies at 0.3 m and 0.4 m, respectively, under a relatively open sky environment, typically with 5~8 satellites. If the duration of the test is sufficient for the ambiguity terms to converge to their true values, then higher accuracy level can be expected from the proposed integrated PPP GPS/MEMS IMU system. The developed integrated system offers the velocity solutions with centimetre to sub-decimetre level accuracy. There is no convergence time required for velocity estimation since the velocity estimate highly depends on the Doppler measurements.

The accuracies of the attitude estimates heavily depend on the grade of IMU used. Due to the significant sensor errors of the MEMS IMU, the attitude accuracies are much poorer than the tactical grade IMU. The proposed integrated system offers the pitch and roll estimates with the accuracy better than 0.5 degree and the azimuth estimate with the accuracy of about 1.5 degrees. The obtained results are comparable to the attitude

accuracies of the DGPS/MEMS IMU integrated system, which uses the same MEMS IMU. It has been found that some non-holonomic dynamic constraints can be used to improve the attitude accuracies for ground vehicles. The constraints used in this research are the 2D velocity constraints. Since the velocity error in the body frame is correlated with the attitude errors, the use of 2D velocity constraints can improve the observability of the attitude estimates. As a result, the attitude accuracies are improved. The results indicate that the azimuth accuracy is improved by 43%-48% and the pitch and roll accuracies are improved by 5%-9% after applying the dynamic constraints.

Normally, the use of current generation of the low cost MEMS IMU can only result in relatively poor attitude accuracies due to its significant sensor errors. This is a limiting factor to apply the proposed integrated system to the applications that require high attitude accuracies. By the year 2020, the sensor error of the MEMS gyroscope can be reduced to 1˚/h (Steen et al., 2010), which is comparable to the tactical grade IMU. By then much higher attitude accuracies can be expected from the proposed integrated PPP GPS/MEMS IMU system and its application can be extended to applications requiring higher attitude accuracies.

Results indicate that the MEMS IMU is able to bridge the GPS outages. However the navigation performance of the proposed integrated system degrades rapidly during GPS outages due to significant sensor errors of MEMS IMU. Under the complete GPS outages, the developed integrated system works in the pure prediction mode and therefore entirely relies on the INS mechanization solution without getting any correction. The position

error accumulates very fast and reaches about 38~40 m over 30 seconds. Even with the aiding from the 2D velocity constraints, it still accumulates to about 10~11 m.

Under the partial GPS outages, the performance of the integrated system mainly depends on the sensor error characteristics, the number of satellites, and the geometry of the available satellites. Due to the lack of enough GPS updates, the position error still accumulates, although the rate of accumulation is damped. When 2 satellites are available, the position error accumulates to about 20~22 m over 30 seconds, and it is reduced to about 5~6 m after applying the 2D velocity constraints. When 3 satellites are available, although the position error accumulates at a much slower rate, it still reaches about 2 m within 30 seconds. Improvements are also observed after using the dynamic constraints.

The proposed algorithm of inertial aided cycle slip detection and identification is implemented in 3 steps, namely WL phase based cycle slip detection and identification, EWL phase based cycle slip detection and identification, and cycle slip identification on L1 and L2 frequencies. The reason of using the WL and EWL phase is that they have much longer wavelength, especially for the EWL phase with a wavelength of 183 cm. This nature makes the cycle slip detection and identification on WL and EWL phase more reliable and robust. Since the WL and EWL phases are linear combination of carrier phase measurements on L1 and L2 frequencies, the cycle slips on L1 and L2 frequencies can be easily determined after the cycle slips on WL and EWL phase are identified. The results indicate that the developed algorithm is able to detect and identify every single cycle slip. By enabling the proposed algorithm in the integrated system, the horizontal

and vertical position accuracies are improved by 18% - 22% under a relatively open sky environment.

The satellites availability is typically poor in the urban canyon areas. The partial and complete GPS outages with durations of several seconds to tens of seconds occur frequently. In such conditions, the positioning accuracy of the proposed integrated PPP GPS/MEMS IMU system can only be at several metres to tens of metres, for instance, with a horizontal position error of 8~10 m. Even with the aiding from the 2D velocity constraints, the horizontal position error can only be reduced to 5~6 m. For the applications requiring higher navigation performance under urban environments, more investigations are needed with the proposed integrated system.

### 6.2 Recommendations

The following recommendations can be made for the future investigation with integrated PPP GPS/MEMS IMU system:

1) Develop fast ambiguity convergence techniques

The proposed integrated PPP GPS/MEMS IMU system requires a convergence time, which is normally 20-40 minutes, to achieve centimetre to decimetre level accuracy. For post-mission applications, it can be overcome by using the backward processing strategy, which has been widely applied in GPS and INS data processing. In order to support real-time applications, some fast ambiguity convergence techniques should be investigated.

2) Develop in-motion alignment algorithm for MEMS IMU.

Due to the significant sensor errors in gyroscopes, the conventional INS alignment method is not suitable for MEMS IMU. In this thesis, the initial attitude of MEMS IMU is obtained from the HG1700 IMU, which is not practical for many applications. An innovative in-motion alignment algorithm should be developed to derive the initial attitude.

3) Integrate the PPP GPS/MEMS IMU system with other sensors.

The azimuth accuracy is typically poor in the integrated PPP GPS/MEMS IMU system, especially when there are no horizontal accelerations. Investigations should be placed on the integration of the PPP GPS/MEMS IMU system with other sensors such as steering angle sensor and GPS compass, which can directly provide the azimuth estimate.

The positioning performance of the integrated PPP GPS/MEMS IMU system is degraded very fast during complete and partial GPS outages, which deteriorate the overall navigation performance. Investigation should be also placed on the integration of the PPP GPS/MEMS IMU system with other sensors, such as altimeter, video sensor and pseudolites, to provide a more reliable and robust navigation solution when GPS dropouts occur.

4) Improved Estimation Method

Since the sensor errors are modeled as Gauss-Markov processes in this thesis, future investigations could involve using Auto-Regressive modeling methods. Investigations

could be also conducted using adaptive Kalman filtering methods in the future, in addition to an extended Kalman filter.

## References

Abdel-Hamind, W., A. Osman, A. Noureldin, and N. El-Sheimy (2004). Improving the Performance of MEMS-based Inertial Sensors by Removing Short-Term Errors Utilizing Wavelet Multi-Resolution Analysis. *Proceeding of ION NTM*, 26-28 January, San Diego CA, pp. 260-266, U. S. Institute of Navigation, Fairfax VA.

Abdel-salam, M. (2005). *Precise Point Positioning Using Un-Differenced Code and Carrier Phase Observations*. PhD Thesis. Department of Geomatics Engineering, University of Calgary, Canada.

Abdel-salam, M. and Y. Gao (2003). Ambiguity Resolution in Precise Point Positioning: Preliminary Results. *Proceedings of ION GPS-2003*, Oregon, Portland.

Abdel-salam, M., Y. Gao, and X. Shen (2002). Analyzing the Performance Characteristics of a Precise Point Positioning System. *Proceedings of ION GPS-*2002, Oregon, Portland.

Altmayer, C. (2000). Enhancing the Integrity of Integrated GPS/INS Systems by Cycle Slip Detection and Correction. *Proceedings of the IEEE Intelligent Vehicles Symposium 2000*, 3-5 October, Dearborn (MI), USA.

Bancroft, J. B. (2009). Multiple IMU Integration for Vehicular Navigation. *ION GNSS 2009, Session D2*, 22-25 September, 2009, Savannah, GA.

Bisnath, S. and R. Langley (2001). High-Precision Platform Positioning with a Single GPS Receiver. *Proceedings of ION GPS-2001*, Salt Lake City, UT.

Brown, A. and Y. Lu. (2004). Performance Test Results of an Integrated GPS/MEMS Inertial Navigation Package. *Proceedings of ION GPS*, 21-24 September, Long Beach CA, PP. 825-832, U. S. Institute of Navigation, Fairfax VA.

Brown, R. G. and P. Y. C. Hwang (1997). *Introduction to Random Signals and Applied Kalman Filtering*. John Wiley & Sons.

Chiang, K. W. (2004). *INS/GPS Integration Using Neural Networks for Land Vehicular Navigation Applications*. PhD Thesis, Department of Geomatics Engineering, The University of Calgary, Canada.

Chiang, K. W., H. Hou, X. Niu, and N. El-Sheimy (2004). Improving the Positioning Accuracy of DGPS/MEMS IMU Integrated Systems Utilizing Cascade De-noising Algorithm. *Proceedings of ION GPS*, 21-24 September, Long Beach CA, pp. 809-818, U. S. Institute of Navigation, Fairfax VA.

Collins, P., F. Lahaye, F. J. Kouba, and P. Heroux (2001). Real-Time WADGPS Corrections from Un-Differenced Carrier Phase. *ION NTM 2001*, Long Beach, CA, 22-24 January, 2001.

Crista- Interface/Operation Document (2004). *Crista Inertial Measurement Unit (IMU) Interface / Operation Document*. A Cloud Cap Technology Inc.

Dissanayake, G., S. Sukkarieh, E. Nebot, and H. Durrant-Whyte (2001). The Aiding of a Low-Cost Strapdown Inertial Measurement Unit Using Vehicle Model Constraints for Land Vehicle Applications, *IEEE Transactions on Robotics and Automation*, Vol. 17, No. 5, pp. 731-747.

Edwan, E., S. Knedlik, J. Zhou, and O. Loffeld (2009). A Constrained GPS/INS Integration Based on Rotation Angle for Attitude Update and Dynamic Models for

Position Update. *Proceedings of ION 2009 International Technical Meeting*, Anaheim, CA, January 26-28, 2009.

El-Sheimy, N. (2007). *Inertial Techniques and INS/DGPS Integration*. ENGO623-Course Notes, Department of Geomatics Engineering, The University of Calgary, Canada.

El-Sheimy, N. and K. P. Schwarz (1999). Navigating Urban Areas by VISAT - a Mobile Mapping System Integrating GPS/INS/Digital Cameras for GIS Applications, *Journal of The Institute of Navigation*, Vol. 45, No. 4, pp. 275-286.

Ellum, C. M. (2001) *The Development of a Backpack Mobile Mapping System*. MSc Thesis, Department of Geomatics Engineering, The University of Calgary, Canada.

Farrell, J. A., and M. Barth (2001) *The Global Positioning System & Inertial Navigation*, McGraw Hills.

Ford, T., J. Neumann, P. Fenton, M. Bobye, and J. Hamilton (2001). OEM4 Inertial: A Tightly Integrated Decentralized Inertial/GPS Navigation System. *Proceedings of ION GPS,* 11-14 September, Salt Lake City UT, pp. 3153 – 3163, U. S. Institute of Navigation, Fairfax VA.

Gao, Y. (2008). *Advanced Estimation Methods and Analysis*. ENGO629-Course notes, Department of Geomatics Engineering, The University of Calgary, Canada

Gao, Y., and X. Shen (2001). Improving Ambiguity Convergence in Carrier Phase-Based Precise Point Positioning. *Proceedings of ION GPS 2001*, Salt Lake City, UT.

Gelb, A., Ed. (1979). *Applied Optimal Estimation*. The MIT press.

Geng, Y. R., A. Cole, A. Dempster, C. Rizos, and J. L. Wang (2007). Developing a Low-cost MEMS IMU/DGPS Integrated System for Robust Machine Automation. *Proceedings of ION GNSS 20th International Technical Meeting*, Fort Worth, TX, September 25-28, 2007.

Godha, S. (2006) *Performance Evaluation of Low Cost MEMS-Based IMU Integrated With GPS for Land Vehicle Navigation Application*, MSc Thesis, Department of Geomatics Engineering, The University of Calgary, Canada.

Grewal, S. M., L. R. Weill, and A. P. Andrews (2001) *Global Positioning Systems, Inertial Navigation and Integration*, John Wiley and Sons Inc.

Hide, C. D. (2003) *Integration of GPS and Low Cost INS Measurements*. PhD Thesis, Institute of Engineering, Surveying and Space Geodesy, University of Nottingham, UK.

Hide, C. D. and T. Moore (2005). GPS and Low Cost INS Integration for Positioning in the Urban Environment. *Proceedings of ION GPS*, 13-16 September, Long Beach CA, pp. 1007-1015, U. S. Institute of Navigation, Fairfax VA.

Hide, C. D., T. Moore, and M. J. Smith (2003). Adaptive Kalman Filtering for Low-Cost INS/GPS, *The Journal of Navigation*, Vol. 56, No. 1, ISSN 0373-4633, pp. 143-152.

Hirokawa, R., N. Kajiwara, R. Ohata, and T. Suzuki (2008). Performance Evaluation of Low Cost Multi-Antenna GPS/INS for Small UAVs. *Proceedings of ION GNSS* 13-16 September, Savannah, GA, USA.

Hofmann-Wellenhof, B., H. Lichtenegger, and J. Collins (2001). *GPS Theory and Practice.* Fifth revised edition, Springer-Verlag Wien New York, ISBN 3-211-83534-2.

Hofmann-Wellenhof, B., K. Legat, and M. Wieser (2003). *Navigation - Principles of Positioning and Guidance.* NewYork: Springer Wien.

Jekeli, C. (2001). *Inertial Navigation System with Geodetic Applications*. Walter de Gryter GmBH and Co.

Kaplan, E. D. (1996). *Understanding GPS: Principles and Applications*, Artech House Inc., Norwood, MA.

Kim, J. and S. Sukkarieh (2002). Flight Test Results of GPS/INS Navigation Loop for an Autonomous Unmanned Aerial Vehicle (UAV). *Proceeding of ION GPS*, 24-27 September, Portland OR, pp. 1162-1170, U. S. Institute of Navigation, Fairfax VA.

Klobuchar, A. (1996). Ionosphere Effects on GPS. in *Global Positioning System: Theory and Applications*, Progress in Astronautics and Aeronautics, Vol 1 , Chapter 12. Eds. B. W. Parkinson, J.J. Spilker Jr, American Institute of Aeronautics and Astronautics, Inc., V, Washington, D.C., U.S.A.

Kouba, J. and P. Heroux (2000). GPS Precise Point Positioning Using IGS Orbit Products. *GPS Solutions*, Vol. 5, No. 2.

Lachapelle, G. (2008). *Advanced GPS Theory and Applications*, ENGO625- Course notes, Department of Geomatics Engineering, The University of Calgary, Canada.

Lee, H. (2002). GPS/Pseudolites/SDINS Integration Approach for Kinematic Applications. *Proceedings of ION GPS*, 24-27 September, Portland ON, pp. 1464-1473, U. S. Institute of Navigation, Fairfax VA.

Li, T. (2009). *Use of Wheel Speed Sensors to Enhance a Reduced IMU Ultra-Tight GNSS Receiver*. MSc Thesis, Department of Geomatics Engineering, The University of Calgary, Canada.

Li, Y., J. Wang, C. Rizos, P. J. Mumford, and W. Ding (2006). Low-cost Tightly Coupled GPS/INS Integration Based on a Nonlinear Kalman Filter Design. *Proceedings of the U.S. Institute of Navigation National Technique Meeting*, pp. 958-966.

Lochhead K., A. Kassam, R. Hare, and L. LeBlanc (2002). CDGPS – Canada-wide DGPS Service: Quality Real Time GPS Positioning. *The Canadian Hydrographic Conference*, Toronto, ON, Canada, May 28-31, 2002.

Mathur, N. G. and F. V. Grass (2000). Feasibility of Using a Low-Cost Inertial Measurement Unit with Centimeter-Level GPS. Proceedings *of ION AM*, 26-28 June, San Diego, pp. 712-720, U. S. Institute of Navigation, Fairfax VA.

Maybeck, P. (1979). *Stochastic Models, Estimation and Control*, Vol. 1. Academic Press.

Mendes, V. B. and R. B. Langley (1994). A Comprehensive Analysis of Mapping Functions Used in Modeling Tropospheric Propagation Delay in Space Geodetic Data. KIS 94, *Proceedings of the International Symposium on Kinematic Systems in Geodesy, Geomatics and Navigation*, Banff, Alberta, 30 August – 2 September 1994, pp. 87-98.

Misra, P. and P. Enge (2001). *Global Positioning System: Signal, Measurements and Performance*. Ganga-Jumuna Press.

Nassar, S. (2003). *Improving the Inertial Navigation System (INS) Error Model for INS and INS/DGPS Applications*, PhD Thesis, Department of Geomatics Engineering, The University of Calgary, Canada.

Nassar, S., K. P. Schwarz, and N. El-Sheimy (2004). INS and INS/GPS Accuracy Improvement Using Autoregressive Modeling of INS Sensor Errors. *Proceedings of ION NTM*, 26-28 January, San Diego, California, U. S. Institute of Navigation, Fairfax VA.

Nayak, R. A. (2000). *Reliable and Continuous Urban Navigation Using Multiple GPS Antennas and a Low Cost IMU*. MSc Thesis, Department of Geomatics Engineering, The University of Calgary, Canada.

Niu, X., T. Hassan, C, Ellum, and N. El-Sheimy (2006). Directly Georeferencing Terrestrial Imagery using MEMS-based INS/GNSS Integrated Systems. *XXIII FIG Congress*. Munich, Germany, October 8-13.

Numajima, T., M. Kihara, Y. Kubo, S. Sugimoto, and T. Seki (2002). INS/DGPS/VMS Integration for In-Motion Alignment. *Proceedings of ION GPS*, 24-27 September, Portland OR, pp. 556-564, U. S. Institute of Navigation, Fairfax VA.

Park, M. (2004). *Error Analysis and Stochastic Modeling of MEMS based Inertial Sensors for Land Vehicle Navigation Applications*, MSc Thesis, Department of Geomatics Engineering, The University of Calgary, Canada.

Park, M. and Y. Gao (2002). Error Analysis of Low Cost MEMS-Based Accelerometers for Land Vehicle Navigation. *Proceedings of ION GPS*, 24-27 September, Portland OR, pp. 1162-1170, U. S. Institute of Navigation, Fairfax VA.

Parkinson, B. W. and J. J. Spilker (1996) *The Global Positioning System: Theory and Applications*, American Institute of Aeronautics and Astronautics.

Petovello, M. (2003) *Real-Time Integration of a Tactical-Grade IMU and GPS for High-Accuracy Positioning and Navigation*, PhD Thesis, Department of Geomatics Engineering, TheUniversity of Calgary, Canada.

Raquet, J. F. (2001). *GPS Receiver Design*. ENGO 699.64-Course notes, Department of Geomatics Engineering, The University of Calgary, Canada.

Ray, J. and K. Senior (2005). Geodetic Techniques for Time and Frequency Comparisons Using GPS Phase and Code Measurements. *Metrologia.*

Salychev, O., V. V. Voronov, M. E. Cannon, R. A. Nayak, and G. Lachapelle (2000). Low Cost INS/GPS Integration: Concepts and Testing. *Proceedings of ION NTM*, 26-28 January, Anaheim CA, pp. 98-105, U. S. Institute of Navigation, Fairfax VA.

Savage, P. G. (2000). *Strapdown Analytics*, Vol. 1.1 Strapdown Associates, Inc.

Schwarz, K. P. and M. Wei (2000). *INS/GPS Integration for Geodetic Applications.* ENGO-623 Lecture Notes, Department of Geomatics Engineering, The University of Calgary, Canada.

Sennott, J. and D. Senffner (1997). Robustness of Tightly Coupled Integrations for Real-Time Centimeter GPS Positioning. *Proceedings of ION GPS 1997*, pp. 655-663. Institute of Navigation.

Shin, E. (2001). *Accuracy Improvement of Low Cost INS/GPS for Land Application*. MSc Thesis, Department of Geomatics Engineering, The University of Calgary, Canada.

Shin, E. and N. El-Sheimy (2004). An Unscented Kalman Filter for In-Motion Alignment of Low Cost IMUs. *Proceedings of Position Location and Navigation Symposium IEEE*, 26-29 April, pp. 273-279.

Shin, E. (2005). *Estimation Techniques for Low-Cost Inertial Navigation*. PhD Thesis, Department of Geomatics Engineering, University of Calgary, Canada.

Shin, E., X. Niu, and El-Sheimy N. (2005). Performance Comparison of the Extended and the Unscented Kalman Filter for Integrated GPS and MEMS-Based Inertial Systems. *Proceedings of ION NTM*, 24-26 January, San Diego CA, pp. 961-969, U. S. Institute of Navigation, Fairfax VA.

Skaloud, J. (1999). *Optimizing Georeferencing of Airborne Survey Systems by INS/DGPS*, PhD Thesis, Department of Geomatics Engineering, The University of Calgary, Canada.

Skone, S. (2001). The Impact of Magnetic Storms on GPS Receiver Performance. *Journal of Geodesy* 75: 457-468, Springer-Verlag, 2001.

Skone, S. (2009). *Atmosphere Effects on Satellite Navigation Systems*. ENGO 633-Course notes, Department of Geomatics Engineering, The University of Calgary, Canada.

Steen, M., P. M. Schachtebeck., M. Kujawska, and P. Hecker (2010). Analysis and Evaluation of MEMS INS/GNSS Hybridization for Commercial Aircraft and Business Jets. *IEEE/ION PLANS 2010*, 3-6 May, Palm Springs, CA.

Stephen, J. (2000). *Development of a Multi-Sensor GNSS Based Vehicle Navigation System.* MSc Thesis, Department of Geomatics Engineering, The University of Calgary, Canada.

Sukkarieh, S. (2000). *Low Cost, High Integrity, Aided Inertial Navigation Systems for Autonomous Land Vehicles*. PhD Thesis, Department of Mechanical and Mechatronic Engineering, University of Sydney, Australia.

Tao, W. Y. (2008). *Near Real-time GPS PPP-inferred Water Vapor System Development and Evaluation.* MSc Thesis, Department of Geomatics Engineering, The University of Calgary, Canada.

Tiberius, C. C. J. M. (1999). The GPS Data Weight Matrix: What Are the Issues? *National Technical Meeting Proceedings*, San Diego, California, January 25-27.

Vermeer, M. (1997). The Precision of Geodetic GPS and One Way of Improving It. *Journal of Geodesy*, 71, 240-245, Springer-Verlag.

Wang, J. and C. Wilson (2002). Improving KGPS/INS Performance for Safety Applications with Vehicle Dynamic Constraints. *Proceedings of ION GPS*, 24-27 September, Portland OR, pp. 1790-1797, U. S. Institute of Navigation, Fairfax VA.

Wang, J-H. (2004). The Aiding of a Low-Cost MEMS IMU for Land Vehicle Navigation Using Fuzzy Logic Expert System. *Proceedings of ION GPS*, 21-24 September, Long Beach CA, pp. 718-728, U. S. Institute of Navigation, Fairfax VA.

Wang, J-H (2006). *Intelligent MEMS INS/GPS Integration For Land Vehicle Navigation*. PhD Thesis, Department of Geomatics Engineering, The University of Calgary, Canada.

Wang, J., H. K. Lee, and S. Hewitson (2003). Influence of Dynamics and Trajectory on Integrated GPS/INS Navigation Performance, *Journal of Global Positioning Systems*, Vol. 2, No. 2, pp. 109-116.

Wang, J-H. and Y. Gao (2003). Performance Improvement of a Low-Cost Gyro-Free INS for Land Vehicle Navigation by using Constrained Navigation Algorithm and Neural Network, *Proceedings of ION GPS/GNSS 2003*, 9-12 September, Portland, Oregon, USA, pp. 762-768.

Wang, J-H. and Y. Gao (2006). The Aiding of MEMS INS/GPS Integration using Artificial Intelligence for Land Vehicle Navigation, *Proceedings of IMECS 2006*, 20-22 June, Hong Kong, China.

Witchayangkoon, B. (2000). *Elements of GPS Precise Point Positioning*. PhD Thesis, The University of Maine.

Zhang, J., Z. Jin, and W. Tian (2003). A Suboptimal Kalman Filter with Fading Factors for DGPS/MEMS-IMU/Magnetic Compass Integrated Navigation. *Proceedings of Intelligent Transportation Systems*, 12-15 October, IEEE, pp, 1229-1234.

Zhang, Y. and Y. Gao (2005). Performance Analysis of a Tightly Coupled Kalman Filter for the Integration of Un-Differenced GPS and Inertial Data, *Proceedings of ION NTM 2005*, 24-26 January, San Diego, CA, USA

Zhang, Y. and Y. Gao (2007). Integration of INS and Un-Differenced GPS Measurements for Precise Position and Attitude Determination. *The Journal of Navigation*, 61, The Royal Institute of Navigation, pp.1-11

Zumberge, J. F., H. Webb, and Y. Bar-Sever (2001). Precise Point Positioning of GPS Data Products and Services from JPL. *ION NTM 2001*, Long Beach, CA, 22-24 January.

Zumberge, J. F., M. B. Heflin, D. C. Jefferson, M.M. Watkins, and F.H. Webb (1997). Precise Point Positioning for the Efficient and Robust Analysis of GPS Data from Large Networks. *Journal of Geophysical Research*, Vol. 102, No. B3 Pages 5005-5017.

Zumberge, J. F., M.M. Watkins, and F.H. Webb (1998). Characteristics and Applications of Precise GPS Clock Solution Every 30 Seconds. *Journal of Navigation*, 44 (4), 449-456, 1998.